UNIVERSITY
OF MICHIGAN
MAY 9 1951
ENGINEERING
LIBRARY

JOURNAL OF THE AERONAUTICAL SCIENCES

VOLUME 18 MAY, 1951 NUMBER 5

CONTENTS

Some Roll Characteristics of Cruciform Delta Wings at Supersonic Speeds.....ZEGMUND O. BLEVISS 289

Nonstationary Motion of Purely Supersonic Wings.....JACK E. FROEHLICH 298

Effects of Pressure Gradient on Stability and Skin Friction in Laminar Boundary Layers in Compressible Fluids.....HERSCHEL WEIL 311

The Performance of Axial-Flow Compressors As Affected by Single-Stage Characteristics.....SEYMOUR M. BOGDONOFF 319

Coupled Free Vibrations of a Swept Wing.....A. E. ENGELBRECHT 329

Analysis of the Elastic and Plastic Stability of Sandwich Plates by the Method of Split Rigidities—I.....P. P. BIJLAARD 339

Readers' Forum: "New Compressibility Correction for Two-Dimensional Subsonic Flow," by E. V. Laitone; "Note on the Minimum Critical Reynolds Number and the Form Parameter," by John C. Freeman, Jr.; "The Influence of the Temperature Variation of the Specific Heats of Air in Shock-Wave Calculations," by J. Kestin; "Convective Heat Transfer from Spheres in a Free-Molecule Flow," by F. M. Sauer; "Heat Transfer by Laminar Flow from a Rotating Plate," by Knox Millsaps and Karl Pohlhausen; "Proper Use of the M.I.T. Tables for Supersonic Flow Past Inclined Cones," by Milton D. Van Dyke, George B. W. Young, and Charles Siska; "A Probe for Measuring Flow Inclination in a Supersonic Air Stream," by Robert D. Fusfeld; "Formulas for Bending with Axial Tension," by Alfred S. Niles; "Simplified Compressible Laminar Boundary-Layer Theory," by Arthur N. Tifford.....350–359

Published by the

INSTITUTE OF THE AERONAUTICAL SCIENCES, INC.

JOURNAL OF THE AERONAUTICAL SCIENCES

Editor: HUGH L. DRYDEN, *Director, N.A.C.A.*

Associate Editor: ROBERT R. DEXTER *Managing Editor:* BERNEICE H. JARCK

Editorial Committee

Aerodynamics

Francis Clauser
Howard Emmons
R. Paul Harrington
R. T. Jones
Carl Kaplan
W. B. Klemperer
John G. Lee
H. W. Liepmann
C. C. Lin
H. F. Ludloff
John R. Markham
Clark B. Millikan
Shatswell Ober
W. Bailey Oswald
Allen E. Puckett
Elliott G. Reid
H. J. F. Reid
Russell Robinson
G. B. Schubauer
W. R. Sears
John Stack
Theodore von Kármán
Richard von Mises

Flight Testing

W. K. Ebel
R. R. Gilruth
Melvin N. Gough
Robert Stanley
E. G. Stout

Meteorology

C. F. Brooks
D. M. Little
E. J. Minser
F. W. Reichelderfer
H. C. Willett

Structures and Materials

W. B. Bleakney
E. W. Conlon
J. P. Den Hartog
L. H. Donnell
E. C. Hartmann
N. J. Hoff
E. E. Lundquist
C. F. Nagel, Jr.
J. S. Newell
Alfred S. Niles
W. Ramberg
E. Reissner
F. R. Shanley
H. W. Sibert
C. R. Strang
S. Timoshenko
H. S. Tsien
Chi-Teh Wang

Rotating Wing Aircraft

Robert Coleman
K. H. Hohenemser
Bartram Kelley
Ralph McClarren
R. H. Miller
R. H. Prewitt
Igor I. Sikorsky

Physiologic Problems

H. G. Armstrong
Louis H. Bauer
Eugene Du Bois
W. Randolph Lovelace, II
Ross A. MacFarland
A. D. Tuttle

Flight Propulsion

George W. Brady
Frank W. Caldwell
L. S. Hobbs
E. E. Johnson
Joseph Keenan
R. P. Kroon
Arthur Nutt
Hans Reissner
Abe Silverstein
C. Fayette Taylor
E. S. Taylor
P. Taylor
E. S. Thompson
H. S. Tsien

Aircraft Design

W. E. Beall
W. K. Ebel
Hall L. Hibbard
Richard Hutton
C. L. Johnson
I. M. Laddon
C. J. McCarthy
Fred E. Weick
Robert J. Woods

Air Transport

Charles Froesch
J. A. Herlihy
R. D. Kelly
Otto E. Kirchner
Jerome Lederer
John C. Leslie
R. Dixon Speas

Instruments

Allan G. Binnie
W. G. Brombacher
Charles H. Colvin
B. M. Craig
C. S. Draper
S. G. Eskin
O. E. Esval
W. L. Howland
George H. Purcell
C. F. Savage
O. Hugo Schuck
L. N. Schwien
C. L. Seward, Jr.
L. D. Statham
R. C. Sylvander
D. K. Warner
P. F. Weber
Elmer P. Wheaton

Vibration and Flutter

Lee Arnold
M. A. Biot
William Bollay
Chieh-Chien Chang
Martin Goland
J. P. Den Hartog

Fuels and Oils

D. P. Barnard
J. H. Doolittle
Graham Edgar
R. T. Goodwin
S. D. Heron
A. M. Rothrock

SUBSCRIPTION RATES

JOURNAL OF THE AERONAUTICAL SCIENCES, Published Monthly.—United States and Possessions: 1 Year, $12.00; Single Copies, $1.50. Foreign Countries Including Canada (American Currency Rate): 1 Year, $13.00; Single Copies, $1.50.

AERONAUTICAL ENGINEERING REVIEW, Published Monthly.—United States and Possessions: 1 Year, $3.00; Single Copies, $0.50. Foreign Countries Including Canada (American Currency Rates): 1 Year, $3.50; Single Copies, $0.50.

Notices of change of address should be sent to the Institute at least 30 days prior to actual change of address.

Manuscripts for publication, proofs, and all correspondence should be addressed to the Editorial Office of the JOURNAL.

Correspondence regarding subscriptions may be addressed to Publication Office, 20th and Northampton Sts., Easton, Pa., or to the Editorial Office of the JOURNAL OF THE AERONAUTICAL SCIENCES, 2 East 64th Street, New York 21, New York.

Copyright, 1951, by the Institute of the Aeronautical Sciences, Inc.

Entered as Second Class Matter at the Post Office, Easton, Pa., May 1, 1937. Acceptance for mailing at a special rate of Postage provided for in the Act of August 24, 1912. Authorized April 29, 1937.

JOURNAL OF THE AERONAUTICAL SCIENCES

VOLUME 18 MAY, 1951 NUMBER 5

Some Roll Characteristics of Cruciform Delta Wings at Supersonic Speeds

ZEGMUND O. BLEVISS*

Douglas Aircraft Company, Inc.

ABSTRACT

Three roll problems associated with a missile-type configuration having a body of circular cross section, a cruciform delta wing, and some unspecified type of tail are considered. They are (1) roll due to aileron deflection of two opposite fins, (2) damping in roll, and (3) roll induced by pitch and yaw. Some effects of fin-fin, wing-body, and wing-body-tail interference are included.

Some theoretical solutions are presented for the roll due to aileron deflection and damping in roll. These results show clearly the effects of fin-fin and wing-body interference. Theoretical calculations for the cross-flow field in the Trefftz-plane behind a cruciform wing with aileron deflection are presented for the two different assumptions of nondistorted and completely rolled up vortex sheets.

A general qualitative discussion of these problems is presented. Effects of high angles of attack are discussed, along with some nonlinear, viscous, and gap effects.

Recommendations are made for future theoretical and experimental research.

INTRODUCTION

THE PURPOSE OF THIS PAPER is to discuss qualitatively three roll problems associated with a particular supersonic missile-type configuration and to present some theoretical solutions to a few of these problems. The configuration is shown in Fig. 1. It has a body of circular cross section, a cruciform delta wing on a portion of the body which is practically cylindrical, and a tail that is not specified as to type or shape.

The basic purpose of a cruciform wing is to be able to supply lift equally in any desired lateral direction by some combination of deflections of the fins. Although any wing composed of nonplanar lifting surfaces has this property, calculations are simplest for the cruciform configuration. The choice of the delta plan form and the circular body cross section was dictated by both the simplification of the theoretical problems and, more practically, their actual use in some supersonic missiles.

The three roll problems considered are (1) roll due to aileron deflection of two opposite fins, (2) damping in roll, and (3) roll induced by pitch and yaw. Within each of these problems it is convenient to classify a subgroup as interference problems. The subgroup consists of fin-fin, wing-body, and wing-body-tail interference. Fin-fin and wing-body interference are defined as the change in any characteristic of a plane wing due to the addition of a fin or body, respectively. Wing-body-tail interference will be used here to mean the change in any characteristic of a wing-body combination due to the addition of a tail.

Most of the theoretical results are based on linearized nonviscous theory, and, where this is not the case, the assumptions are explicitly stated. Furthermore, whenever fins are deflected, the effect of the gap is neglected.

NOTATION

It is convenient for illustrative purposes to consider a cruciform wing to be oriented so that one pair of fins is horizontal and the other pair vertical.

Wide Delta.—All leading edges supersonic.

Narrow Delta.—All leading edges subsonic.

Plane Wing.—Flat plate of zero thickness with delta plan form, unless otherwise stated.

Plane Aileron.—Plane wing with aileron deflection—i.e., the two halves of the plane wing deflected in opposite directions by $\pm\delta$.

Cruciform Wing.—Two plane wings with the same plan form normal to each other and symmetrically arranged about the line of intersection.

Cruciform Aileron.—Cruciform wing with aileron deflection of the horizontal fins. The general features are illustrated in Fig. 2.

Mixed Cruciform Aileron.—Cruciform aileron with wide delta vertical fins and narrow delta horizontal fins.

A = body diameter/wing span = $2r/b$

b = total span of horizontal fins

Presented at the Session on Stability, Control, and Guidance, Annual Summer Meeting, I.A.S., Los Angeles, July 12–14, 1950.

* Aerodynamics Consultant, Santa Monica Plant. Also, Graduate Student, California Institute of Technology

FIG. 1
MISSILE TYPE CONFIGURATION

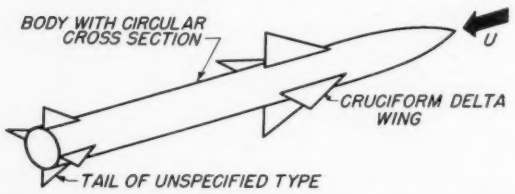

FIG. 2
CRUCIFORM AILERON

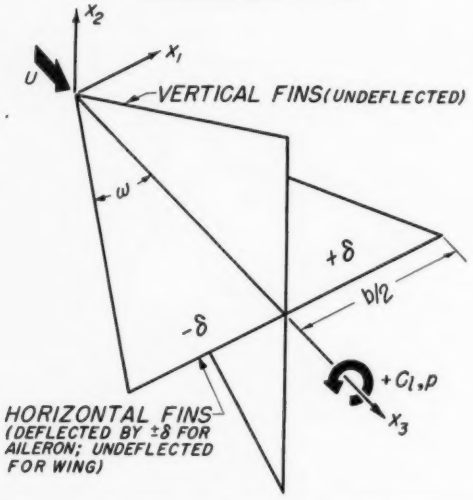

FIG. 3
ROLL DUE TO AILERON DEFLECTION AND DAMPING IN ROLL FOR WIDE DELTA CRUCIFORM WING

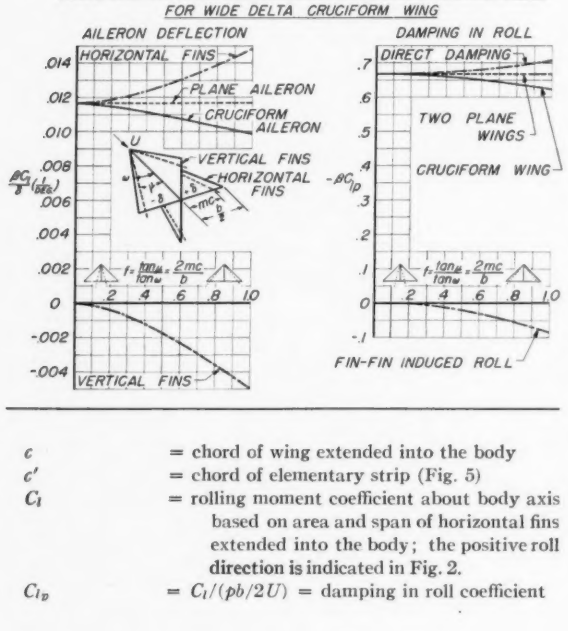

c = chord of wing extended into the body
c' = chord of elementary strip (Fig. 5)
C_l = rolling moment coefficient about body axis based on area and span of horizontal fins extended into the body; the positive roll direction is indicated in Fig. 2.
C_{l_p} = $C_l/(pb/2U)$ = damping in roll coefficient
d = $\tan\omega/\tan\mu$ (for subsonic leading edges)
$d\xi$ = differential width of elementary strip
dL = differential lift of elementary strip
dM = differential moment about the axis of the elementary strip; positive when counterclockwise facing upstream
$E(\sqrt{1-d^2})$ = complete elliptic integral of the second kind with the modulus $\sqrt{1-d^2}$
f = $\tan\mu/\tan\omega = 1/d$ (for supersonic leading edges)
M = Mach Number
m = $1/\sqrt{M^2-1}$
p = angular rolling velocity
q = $(1/2)\rho U^2$ = free-stream dynamic pressure
r = body radius or radial distance from origin in Trefftz-plane (Fig. 10)
U = free-stream velocity
u_j $(j = 1, 2, 3)$ = perturbation velocities
$n(\theta)$ = cross-flow velocity normal to the radius from the origin in the Trefftz-plane (Fig. 10)
x_j $(j = 1, 2, 3)$ = Cartesian coordinate system (Fig. 2)
α = angle of attack
β = $1/m = \sqrt{M^2-1}$
δ = aileron deflection angle
θ = angle from the x_1 axis of the radius from the origin in the Trefftz-plane (Fig. 10)
μ = Mach angle
ξ = distance between the elementary strip and the wing-body juncture
$\bar{\xi}$ = ξ/mc'
ρ = free-stream density
ω = half vertex angle of the delta plan form

Theoretical Results

Cruciform Wing—No Body

If the leading edges are supersonic, exact solutions are readily obtained for roll due to aileron deflection and damping in roll. The results are shown in Fig. 3.

Consider first the roll due to aileron deflection. The configuration is conical, and the solution is obtained from known conical wing solutions. Since the vertical fins have supersonic leading edges, the horizontal fins are independent of each other. The presence of the vertical fins requires that the sidewash velocities be zero in the plane of these fins. Hence, by symmetry, each horizontal fin acts like half of a wide delta plane wing with the angle of attack of the fin. The results in Fig. 3 are replotted from reference 1. Results for the plane aileron are plotted for comparison to illustrate the effect of fin-fin interference. The rolling moment coefficient for the plane aileron is independent of f and is given by

$$\beta C_l/\delta = 2/3 \qquad (1)$$

When the vertical fins are added, the roll carried by the horizontal fins is considerably increased above that for the plane aileron. However, unfortunately, a counter-rolling moment is induced on the vertical fins which more than offsets this gain, and the final result is a decrease in aileron effectiveness. The rolling moment

coefficient for the complete cruciform aileron is given by

$$\frac{\beta C_l}{\delta} = \frac{4}{3\pi(1-f^2)}\left[\frac{(1-2f^2)\cos^{-1}f}{\sqrt{1-f^2}} + f\right] \quad (2)$$

The result for four deflected fins is obtained from this by superposition. The reduction in rolling moment due to fin-fin interference is a maximum of 15 per cent when the leading edges are sonic.

The results for damping in roll are similar. The solution to this problem is again reduced to the solution of a plane wide delta wing, but, in this case, the wing is not flat. With the usual assumption that the effect of rolling can be represented by an apparent linear angle of attack distribution, the problem is reduced to that of a plane wing with linear symmetrical twist. Since this wing is not conical, more general wing methods must be used. Here, the comparison must be made with two plane wings for which the damping in roll is independent of f and given by

$$\beta C_{l_p} = -2/3 \quad (3)$$

If these two plane wings are combined to form a cruciform wing, the effect is generally the same as for the aileron. This case cannot be separated conveniently into horizontal and vertical fins. Instead, the corresponding rolling moments are called direct damping (the damping moment carried by the fin itself) and fin-fin induced roll (the counter-roll induced by fin interaction). Here, again, the result is a decrease in the desired characteristic, in this case damping in roll. The equation for the cruciform wing damping in roll is

$$\beta C_{l_p} = -\frac{2}{3\pi(1-f^2)^2}\left[f(2-5f^2) + (2-5f^2+6f^4)\frac{\cos^{-1}f}{\sqrt{1-f^2}}\right] \quad (4)$$

Fin-fin interference has less effect in this case. It causes a maximum reduction of damping in roll of about 7 per cent for sonic leading edges.

When the leading edges are subsonic, the problem is much more difficult, and, as yet, no exact solutions are known. In this paper an attempt is made to approximate the solution for the cruciform aileron in the region where the leading edges are not too subsonic (say, $0.75 \leq d \leq 1.0$). Actually, the method is nothing more than a reasonable guess at the solution from a knowledge of some limiting cases combined with under- and over-estimates. In Fig. 4, the known exact solution for the plane aileron[1] is shown. The equation for this curve is

$$\beta C_l/\delta = (2/3)d \quad (5)$$

Take a fixed value of d for the horizontal fins. Then let the vertical fins increase in size from the limiting case of no fins (plane aileron) to the other limiting case of fins with sonic leading edges (mixed cruciform aileron). It seems reasonable that the variation in rolling moment during this process will be continuous and monotonic

FIG.4
APPROXIMATION TO ROLL DUE TO AILERON DEFLECTION FOR NARROW DELTA CRUCIFORM WING

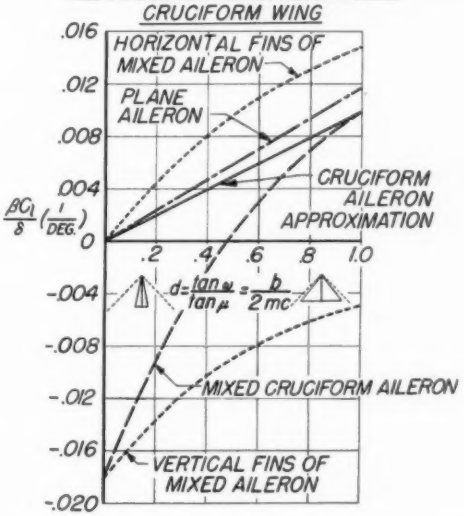

FIG.5
ESTIMATES USING ELEMENTARY STRIP

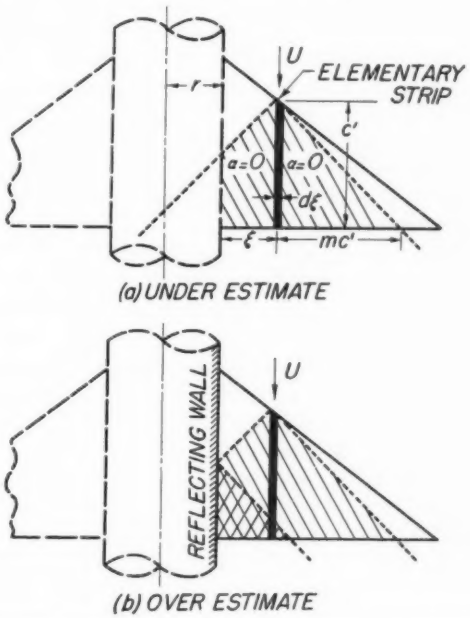

and that the value of rolling moment for the cruciform aileron will lie somewhere between the two limits. In Fig. 4, the solution for the mixed cruciform aileron is shown. This solution is readily obtained from that for the plane narrow delta wing[2] using symmetry arguments. The end points at $d = 0$ and $d = 1.0$ are known for the cruciform aileron, and it appears that a straight

line connecting these end points should give a reasonable approximation at least for the range of d values mentioned above. The equation of this line is

$$\beta C_l/\delta = (16/9\pi)\, d \tag{6}$$

and it is shown in Fig. 4 as the cruciform aileron approximation. When the slender body solution is available, the slope will be known at $d = 0$ and a better approximation can be faired in. From these considerations it appears that fin-fin interference has a detrimental effect for all leading-edge conditions. It is believed that this will also be true for damping in roll.

Cruciform Wing—with Body

No attempt is made to carry out any exact solutions when a body is present. Instead, a simple procedure for estimating the wing-body interference is used. Using this estimating procedure, results are obtained for the three cases treated above.

It is most convenient for these estimates to use the elementary strip[1, 3, 4] (see Fig. 5). The pressures produced by this strip may be obtained by interpreting the strip as a line of sources of constant strength determined by the wing downwash prescribed along that line. It is more useful in these applications to interpret the strip as a lifting wing of differential width $d\xi$ whose length dimension is in the free-stream direction and whose angle of attack is constant. Adjacent to the wing on both sides is a flat plate at zero angle of attack. On one side the plate is always ahead of any disturbances, while on the other side the leading edge is straight and may be subsonic or supersonic depending on the wing to which the calculations are to be applied. Such a strip is intended to be applied, of course, only to wings that are not cambered.

Now consider this strip as a deflected element in one fin of a delta wing-body combination as shown in Fig. 5. When the strip is close enough to the body, disturbances will strike the body at the wing-body juncture. Part of the disturbances will be diffracted and pass over the body downstream of a helical path, and the rest will be reflected back onto the fin. The part that passes onto the body can contribute nothing to the rolling moment about the body axis, since the body cross section is circular. It is this fact that makes a simple estimation of the wing-body interference possible. The disturbances that are reflected back onto the fin increase the lift of the fin and, hence, increase the rolling moment carried by the fin.

It is now apparent how the contribution of a fin to the rolling moment may be bracketed by under- and overestimates. This is illustrated in Fig. 5 for the case of supersonic leading edges. It is also true, however, if the leading edges are subsonic. An underestimate is obtained by assuming that no reflection takes place at the wing-body juncture. With the elementary strip this amounts to using only that portion of the pressure distribution which is cross-hatched in Fig. 5a. An overstimate is obtained by assuming that complete reflection takes place. This is realized if the body is replaced at the wing-body juncture by a reflecting wall that has supersonic leading edges. This is illustrated in Fig. 5b, where the region with double cross-hatching indicates the added pressures due to reflection.

Using well-known methods of supersonic wing theory, formulas for the differential lift dL and the differential rolling moment about the axis of the strip dM are easily derived. When the disturbances from the strip do not strike the body before passing off the fin, the solutions for the strip are exact and are given by

$$dL = 4mqc'(\xi)\ \alpha(\xi)d\xi \tag{7a}$$

$$dM = 0 \tag{7b}$$

for a supersonic leading edge and by

$$dL = 4mq\ \sqrt{d}\ c'(\xi)\ \alpha(\xi)d\xi \tag{8a}$$

$$dM = -m^2q\ \sqrt{d}\ (1-d)\ c'^2(\xi)\ \alpha(\xi)d\xi \tag{8b}$$

for a subsonic leading edge. When the disturbances strike the body the under- and overestimates are given by

$$dL = \frac{4mqc'(\xi)\ \alpha(\xi)}{\pi}\left(\pi + \bar{\xi}\ \text{sech}^{-1}\,\bar{\xi} - \cos^{-1}\bar{\xi}\right) d\xi \tag{9a}$$

$$dM = \frac{2m^2qc'^2(\xi)\ \alpha(\xi)}{\pi}\left(\sqrt{1-\bar{\xi}^2} - \bar{\xi}^2\ \text{sech}^{-1}\,\bar{\xi}\right) d\xi \tag{9b}$$

and

$$dL = 4mqc'(\xi)\ \alpha(\xi)d\xi \tag{10a}$$

$$dM = \frac{4m^2qc'^2(\xi)\ \alpha(\xi)}{\pi}\left(\sqrt{1-\bar{\xi}^2} + \bar{\xi}^2\ \text{sech}^{-1}\,\bar{\xi} - 2\bar{\xi}\cos^{-1}\bar{\xi}\right) d\xi \tag{10b}$$

respectively, if the leading edge is supersonic. If the leading edge is subsonic, a single application of Evvard's method yields the underestimate

$$dL = \frac{4mqc'(\xi)\ \alpha(\xi)}{\pi}\left\{\bar{\xi}\ \text{sech}^{-1}\left[\frac{\bar{\xi}(1+d)}{2d+\bar{\xi}(1-d)}\right] + \sqrt{d}\cos^{-1}\left[\frac{(1-d)-2\bar{\xi}}{1+d}\right]\right\} d\xi \tag{11a}$$

$$dM = \frac{2m^2qc'^2(\xi)\,\alpha(\xi)}{\pi}\left\{\sqrt{d}\ \sqrt{d+(1-d)\bar{\xi}-\bar{\xi}^2} - \bar{\xi}^2\ \text{sech}^{-1}\left[\frac{\bar{\xi}(1+d)}{2d+\bar{\xi}(1-d)}\right] - \frac{\sqrt{d}\,(1-d)}{2}\cos^{-1}\left[\frac{(1-d)-2\bar{\xi}}{1+d}\right]\right\} d\xi \tag{11b}$$

For the overestimate it is necessary to solve the problem for a strip in the presence of two subsonic edges. The solution requires repeated use of Evvard's method and would lead to rather complicated expressions for dL and dM. This solution has not been carried out.

These estimates may be applied only if the disturbances propagating around the body do not encounter other fins; for, if this occurs, rolling moments will be induced which the estimates do not account for. Then, to apply the estimates, the body must be large enough so that the fins do not interact. Obviously, the limiting cases where the disturbance from a fin leading edge-body juncture just strikes the trailing edge of the next fin will be different for the plane and cruciform wings. This is illustrated in Fig. 6. For supersonic leading edges, the estimates may be used for a cruciform wing if

$$A \geq 2f/(\pi + 2f)$$

and, for a plane wing, if

$$A \geq f/(\pi + f)$$

The corresponding regions of validity for subsonic leading edges are

$$A \geq 2/(2 + \pi d)$$

for a cruciform wing and

$$A \geq 1/(1 + \pi d)$$

for a plane wing.

Now strips can be superposed by integration to give the under- and overestimates for any twisted wing. If the spanwise distribution of angle of attack is complicated, the integrations will have to be carried out graphically or numerically.

The method will first be applied to the problem of roll due to aileron deflection when the leading edges are supersonic. The angle of attack is constant across the span, and, by use of Eqs. (9), the underestimate is found to be

$$\frac{\beta C_l}{\delta} = \frac{(1-A)^2}{3\pi}\left[2(1+2A)\frac{\cos^{-1} f}{\sqrt{1-f^2}} + \pi(1+2A) + 2f(1-A)\right] \quad (12)$$

In like manner, using Eqs. (10), the overestimate is

$$\frac{\beta C_l}{\delta} = \frac{2(1-A)^2}{3\pi}\left[3\pi A + 2(1-A)\left(\frac{\cos^{-1} f}{\sqrt{1-f^2}} + f\right)\right] \quad (13)$$

The results for wing-body combinations are given in Fig. 7 for both the cruciform and plane ailerons for three values of the parameter f. For a given value of f, the curves for the under- and overestimates are indicated by the same type of line. Each pair of curves is broken at a value of A indicated by a short solid line.

FIG.6
LIMITS OF FIN-FIN INDUCED EFFECTS

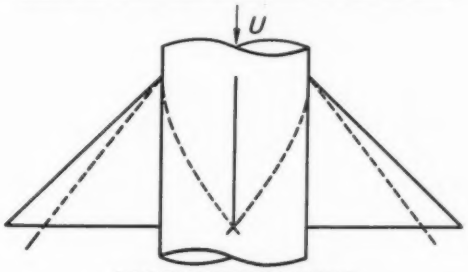

(a) CRUCIFORM WING

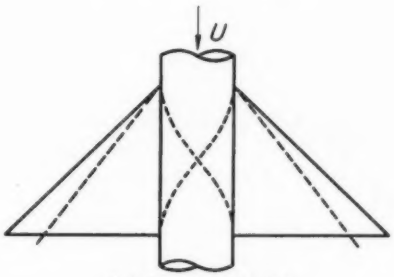

(b) PLANE WING

FIG.7
ROLL DUE TO AILERON DEFLECTION
FOR WIDE DELTA WING-BODY COMBINATIONS

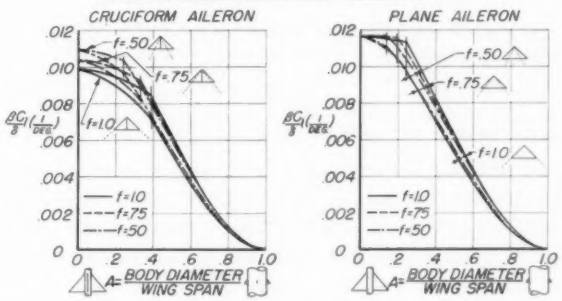

These are the values of A above which the estimates are valid and, for the sake of brevity, will be referred to as A_l. For $A \geq A_l$ the curves are given by Eqs. (12) and (13). The end points for $A = 0$ are known exactly from Fig. 3. The curves are then completed by drawing in curves from the known values at $A = 0$ to the known estimates at $A = A_l$. These curves are not drawn in tangent to the estimate curves, since it is expected that the exact solution to this problem will consist of two different expressions exhibiting the same type of slope discontinuity. Furthermore, the curves are drawn convex upward, since this appears to be the most reasonable shape. In most cases it is rather easy to complete the curves in a reasonable fashion.

The difference between the value for the plane aileron at $A = 0$ and any other value is an indication of the effects of fin-fin and wing-body interference. At $A = 0$, any decrease in rolling moment is due entirely to fin-fin interference. For $0 < A < A_1$, the reduction in rolling moment is due to both types of interference. For $A \geq A_1$, the effects are due solely to wing-body interference.

Damping in roll for supersonic leading edges is treated in the same manner. Here, the angle of attack is distributed linearly across the span. Integrating out, using Eqs. (9) and (10), yields the underestimate

$$\beta C_{l_p} = -\frac{(1-A)^2}{3\pi(1-f^2)}\left\{[(2-3f^2)\,(1+2A)+3A^2(2-f^2)]\frac{\cos^{-1}f}{\sqrt{1-f^2}}+\pi(1-f^2)\,(1+2A+3A^2)+ f(2-f^2)\,(1-A)\,(1+3A)\right\} \quad (14)$$

and the overestimate

$$\beta C_{l_p} = -\frac{2(1-A)^2}{3\pi(1-f^2)}\left\{(1-A)\,[(2-3f^2)+A(2-f^2)]\frac{\cos^{-1}f}{\sqrt{1-f^2}}+2\pi A(1-f^2)\,(1+2A)+ f(1-A)[(2-f^2)+A(2-3f^2)]\right\} \quad (15)$$

The results are shown in Fig. 8 with the exact end points at $A = 0$ taken from Fig. 3.

The cruciform aileron with subsonic leading edges can be treated even though the elementary strip overestimate is not known. Using Eqs. (11), the underestimate is given by

$$\frac{\beta C_l}{\delta} = \frac{2(1-A)^2}{3\pi}\left\{[3d(1+A)-(1-A)]\frac{\tan^{-1}\sqrt{d}}{\sqrt{d}}+\frac{3d(1+A)+(1-A)}{1+d}\right\} \quad (16)$$

The overestimate can be given if the solution for a fin with a subsonic leading edge adjacent to a wall with supersonic leading edges can be obtained. This is just the mixed cruciform aileron solution described above. The overestimate is

$$\frac{\beta C_l}{\delta} = [(1-A)^2 d/3E(\sqrt{1-d^2})]\,[4+A(3\pi-4)] \quad (17)$$

The results are given in Fig. 9. The end points at $A = 0$ are obtained from Fig. 4, where, it will be remembered, those for the cruciform aileron are approximate.

Cross-Flow in the Trefftz-Plane

Whenever any of the fins of the cruciform delta wing carries lift, a vortex sheet passes downstream from the trailing edge of that fin. A wing-body combination with all fins lifting will have four vortex sheets trailing downstream about the body. These sheets will deflect and distort under the influence of the body and the spatial distribution of vorticity. This is an extremely nonlinear problem whose exact solution is beyond present-day mathematics. Associated with the vortex sheets is a cross-flow field that will induce lift on any tail fins. This is what is referred to as wing-body-tail

FIG. 8
DAMPING IN ROLL FOR WIDE DELTA WING–BODY COMBINATIONS

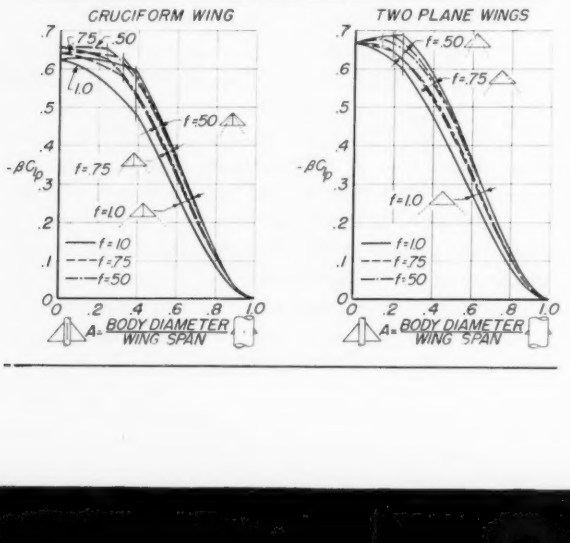

FIG. 9
ROLL DUE TO AILERON DEFLECTION
FOR NARROW DELTA WING–BODY COMBINATIONS

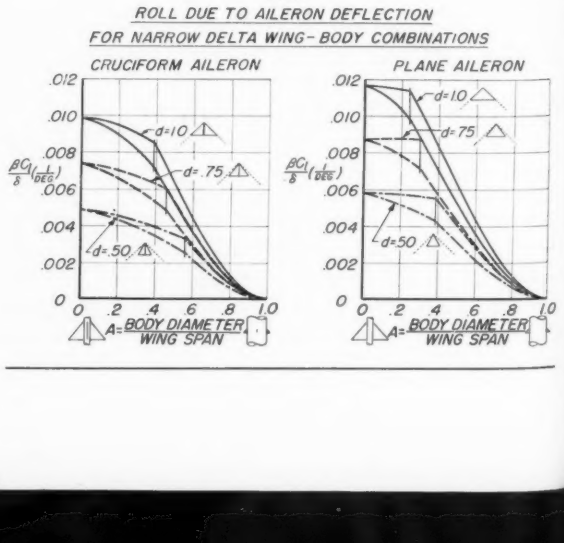

interference. These induced tail lifts and rolling moments act generally to oppose those of the wing.

It is obviously important to be able to estimate the cross-flow field at the tail. Until recently, most theoretical work on the cross-flow field behind plane wings in supersonic flow assumed that the vortex sheet remained undistorted[5, 6] (see reference 6 for further references), although, in some cases, attempts were made to estimate the deflection.[4] It was found that for undistorted vortex sheets the Trefftz-plane (infinitely for downstream) values of cross-flow velocities were obtained for all practical purposes a few chord lengths downstream of the wing.[5] Some elegant Trefftz-plane methods were developed.[5,7] Two recent papers[8, 9] indicate that, for wings of low aspect ratio such as considered in this paper, the trailing vortex sheets are certainly rolled up by the time the tail position is reached. In reference 4, some study is made of a plane wing-tail interference problem for the two assumptions of a deflected but nondistorted vortex sheet and the vortex sheet replaced by two deflected incompressible vortices. In reference 9, the effect of a circular body on the motion of two incompressible vortices is studied.

Little theoretical work has been done on the cross-flow field behind cruciform wings. However, the methods and results for the plane wing problems, which are summarized above, act as useful guides for the study of the cruciform problems. At first, Trefftz-plane solutions were sought. It was soon found that the elegant Trefftz-plane methods used with plane wings generally do not work. An approximate Trefftz-plane solution for a wide delta cruciform aileron is given in reference 1. The vortex sheets are assumed to be undeflected and undistorted. The cross-flow field generated by the vortex sheets from the horizontal fins is replotted in Fig. 10. For comparison, the assumption that the horizontal vortex sheet is rolled up into two undeflected incompressible vortices located at the centroids of vorticity from each fin is shown. This comparison is made only for the horizontal fins, because the vorticity distribution at the trailing edge of the vertical fins is such that the vortex sheet cannot be assumed to roll up into two distinct vortices. In Fig. 10, the vortex sheet and the two vortices lie along the x_1 axis, the vortices being located at $x_1 = \pm 0.96\ mc$. The velocity components normal to a radial line through the origin are shown. These results are presented to illustrate the type of cross-flow calculations that can be made for the cruciform wing.

FIG. 10
CROSS FLOW IN TREFFTZ-PLANE DUE TO HORIZONTAL FINS OF WIDE DELTA CRUCIFORM AILERON

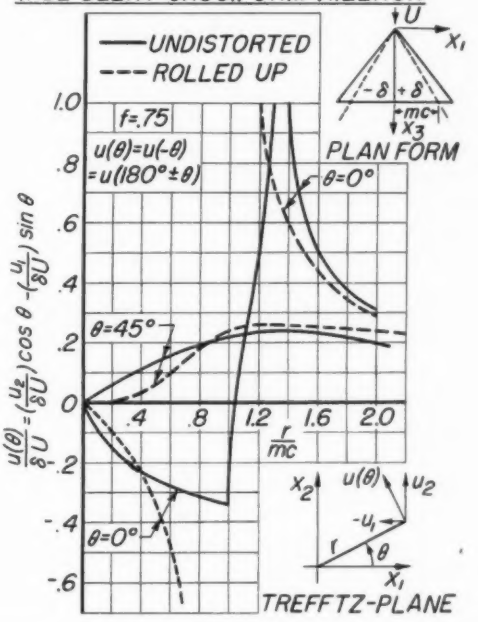

Qualitative Discussion

The above theoretical results are based on linearized nonviscous theory. Even in the results presented for the cross-flow field at the tail where linear theory was not used downstream of the wing, linearized nonviscous theory was used to determine the needed vorticity distribution at the wing trailing edges. In actual use, the cruciform wing may be subjected to angles of pitch and yaw far above the ranges within which linearized theory can be expected to give reasonable results. In these high angle-of-attack ranges, the nonlinear and viscous effects and the effect of the gap between a deflected fin and the body will be considerable. These effects are much more severe behind the wing than on the wing. The following qualitative discussion attempts to indicate the difficulties associated with the various roll problems at large angles of pitch and yaw and, where possible, the qualitative effects on the roll characteristics.

Aileron Deflection

Consider first the case of aileron deflection with no pitch or yaw. The angles through which the fins are deflected are normally within the range of linearized theory applications. A certain loss in lift must be expected because of the gap between the deflected fin and the body through which some pressure equalization takes place. Furthermore, there may be other lift losses due to viscous effects such as separation. In general, this leads to rolling moments somewhat less than predicted by theory. However, it is expected that the above theoretical results furnish a good approximation to the effects of fin-fin and wing-body interference.

Now if this aileron is given an angle of attack, the angle of attack of one fin is decreased, while the angle of attack of the other fin is increased. The fin at the

high angle of attack carries proportionately more of the lift that generates the rolling moment. At the same time, the gap and separation losses become more severe. The result is probably a decrease of aileron effectiveness with angle of attack.

If, instead of pitching, the aileron is yawed, some rolling moments must be expected because of lateral asymmetry. The body and viscous effects will certainly be important factors, and, hence, it is expected that theoretical results for yawed delta wings usually will not be applicable. From physical reasoning it does not seem possible to even predict the sign of these additional rolling moments.

All the considerations up to this point have dealt with the aileron as a stationary flow problem. Actually, of course, when the fins are deflected in flight, there is a time interval before stationary flow is established. Knowledge of the rolling moments in this transient flow region is important in stability and control considerations. No theoretical results are available.

If there is a tail on the body, the roll induced by the vorticity from the aileron is usually opposite in sign to that of the aileron. This effect is generally much greater than the effects of fin-fin or wing-body interference and results in reduced aileron effectiveness. When the body is pitched or yawed or both, the tail moves into flow regions where the induced cross-flow velocities are lower. This decreases the induced tail counter-rolling moments. In short, the wing-body-tail interference effects decrease as the angle between the free-stream direction and the body axis is increased.

Damping in Roll

The theoretical results for damping in roll for zero pitch and yaw were obtained by replacing a nonstationary problem by what is assumed to be an equivalent stationary problem. It was assumed that rolling induced an apparent linear twist. The twisted cruciform wing was then solved as a stationary problem. The magnitude of the nonstationary effects is not known for the cruciform wing, but results for plane wings indicate that these effects can be large.

In any case, gap and separation effects will probably decrease the actual damping in roll below that predicted by the correct linearized solution.

Another nonstationary problem arises for a rolling wing at an angle of attack. The flow will have lateral symmetry when the fins are horizontal and vertical or when both sets of fins are at 45°. However, for all other orientations, the asymmetry of the flow over the lifting surfaces will induce rolling moments that vary with the orientation. It is not known how important these effects are, and no theoretical results are available.

If the body has a tail, the same remarks apply as for the cruciform aileron case.

Pitch and Yaw Effects

Consider a cruciform wing that is in combined pitch and yaw. If the angles of pitch and yaw are equal or if either angle is zero, no rolling moments can be induced. For all other orientations, rolling moments must be expected because of the asymmetry in the flow. Linearized theory cannot predict the rolling moments,[1, 10] since these moments must be at least of second order—i.e., proportional to the product of the angle of attack and the angle of yaw. It appears that this problem will have to be attacked by experiment.

Another effect of pitch or yaw which can be important is the following: Consider a cruciform wing that has the horizontal fins—say, at incidence. When the wing is yawed, lateral asymmetry will induce rolling moments.

The tail effects are qualitatively the same as for aileron deflection and damping in roll.

Wing-Body-Tail Interference

The difficulties associated with the computation of wing-body-tail interference are discussed here.

The first thing that must be known is the vorticity produced by the fins. For aileron deflection and damping in roll, the vorticity distributions at the trailing edges of the fins can be computed by linearized theory if the leading edges are supersonic and there is no body. With a body present, an exact linearized solution would be difficult to compute. Any computations for combined pitch and yaw appear to be out of the question. At high angles of pitch and yaw, the actual vorticity distributions will undoubtedly differ considerably from any linearized computations because of the nonlinear, viscous, and gap effects.

As remarked above, it is now known that the vortex sheets are rolled up a short distance downstream of the wing. It appears that, if incompressible vortices are assumed to start at the trailing edges of the wing, useful engineering results can be obtained. A vortex is placed at the centroid of the vorticity distribution at the trailing edge of each fin. The strength of the vortex is put equal to the total circulation at the fin trailing edge. If the vorticity is all of one sign, a single vortex is assumed to trail from the fin. However, there are cases for which the vorticity at the trailing edge changes sign. This occurs, for example, for a plane aileron or a cruciform wing in roll. For these cases the vortex sheet probably rolls up into two distinct vortices of opposite sign and different strengths, and the vortex pattern behind a cruciform configuration might consist of two vortices trailing from each fin.

Next, the motion of the vortices as they proceed downstream to the tail must be studied. For the cases of aileron deflection and damping in roll with the body axis in the free-stream direction, the motion of the vortices as they proceed downstream will be roughly in a

direction tangential to the body with some radial displacement if only a single vortex is assumed to trail from each fin. Results for these cases can probably be obtained without excessive labor. If two vortices trail from each fin, the labor of calculation is greatly increased. Certain phases of the vortex motion behind a cruciform wing-body combination in combined pitch and yaw will definitely have to be studied experimentally.

Finally, once the position and strength of the vortices are known at the tail, the induced angle-of-attack distributions on the tail fins can be computed. If the tail is a wide delta cruciform configuration, the elementary strip estimate method may be used to determine the induced rolling moment. The integrations would be carried out graphically or numerically. For other types of tails, estimating procedures would have to be developed.

Recommendations for Future Research

A number of aircraft companies and laboratories are now carrying on theoretical and experimental research on cruciform wings. Practically none of this material is published, and, for the most part, the details of these researches are not known to the author. Hence, some of the research recommended here is probably already under way.

Theoretical Research

Most of the theoretical research on cruciform configurations appears to be by slender body methods. Reference 10 gives the solution for combined pitch and yaw and shows that, within slender body theory, no rolling moments can be induced. Future slender body research should then be confined to the aileron deflection and damping in roll problems. Such solutions will be useful as limiting cases. Furthermore, once the basic incompressible cross-flow problem is solved, solutions may be given for more general cruciform wing-body combinations than considered here.

Some attempt should be made to solve cruciform delta wings with subsonic leading edges. The simplest problem appears to be the case of aileron deflection with no body, since it can be attacked by conical flow methods. For other cases such as damping in roll and cruciform wing-body combinations, the labor involved in obtaining exact solutions may not warrant the effort.

Some study should be made of the nonstationary problems. Results from nonstationary plane wing problems will be useful.

Work should be continued on obtaining vorticity distributions at the trailing edges of cruciform wing-body combinations. The most useful results for the cross-flow field at the tail will probably be obtained by studying the motion of incompressible vortices as approximations to the rolled-up vortex sheets. Some work along this line is in progress.

Experimental Research

Some research is now in progress on the vortex motion and the cross-flow field behind cruciform wing-body combinations. More fundamental research is needed, especially for those problems where linearized theory can yield no answers.

The really basic job of experimental research should be the systematic hunting down of nonlinear and viscous effects.

References

[1] Bleviss, Zegmund O., *Some Roll Characteristics of Plane and Cruciform Delta Ailerons and Wings in Supersonic Flow*, Report No. SM-13431, Douglas Aircraft Company, Inc., June, 1949.

[2] Stewart, H. J., *The Lift of a Delta Wing at Supersonic Speeds*, Quarterly of Applied Mathematics, Vol. IV, No. 3, October, 1946.

[3] Lagerstrom, P. A., and Van Dyke, M. D., *General Considerations About Planar and Non-Planar Lifting Systems*, Report No. SM-13432, Douglas Aircraft Company, Inc., June, 1949.

[4] Graham, Martha E., *Some Linearized Computations of Supersonic Wing-Tail Interference*, Report No. SM-13430, Douglas Aircraft Company, Inc., December, 1948.

[5] Lagerstrom, P. A., and Graham, M. E., *Downwash and Sidewash Induced by Three-Dimensional Lifting Wings in Supersonic Flow*, Report No. SM-13007, Douglas Aircraft Company, Inc., April, 1947.

[6] Mirels, Harold, and Haefeli, Rudolph C., *The Calculation of Supersonic Downwash Using Line Vortex Theory*, Journal of the Aeronautical Sciences, Vol. 17, No. 1, p. 13, January, 1950.

[7] Lagerstrom, P. A., and Graham, M. E., *Methods for Calculating the Flow in the Trefftz-Plane Behind Supersonic Wings*, Report No. SM-13288, Douglas Aircraft Company, Inc., July, 1948.

[8] Spreiter, John R., and Sacks, Alvin H., *The Rolling Up of the Trailing Vortex Sheet and Its Effect on the Downwash Behind Wings*, Journal of the Aeronautical Sciences, Vol. 18, No. 1, p. 21, January, 1951.

[9] Lagerstrom, P. A., and Graham, M. E., *Aerodynamic Interference in Supersonic Missiles*, Report No. SM-13743, Douglas Aircraft Company, Inc., July, 1950.

[10] Spreiter, John R., *Aerodynamic Properties of Cruciform-Wing and Body Combinations at Subosnic, Transonic, and Supersonic Speeds*, N.A.C.A. T.N. No. 1897, June, 1949.

Nonstationary Motion of Purely Supersonic Wings

JACK E. FROEHLICH*

California Institute of Technology

ABSTRACT

A general theory is presented for the calculation of the total forces acting on purely supersonic wings. The method applies to wings having an arbitrary downwash distribution (stationary or nonstationary) and is valid whenever all of the wing edges are supersonic. The general three-dimensional nonstationary problem is reduced to an equivalent two-dimensional problem. In the case of harmonic oscillations, the aerodynamic coefficients are expressed in terms of known or tabulated functions. The specific example of an oscillating delta wing is considered, and values of the aerodynamic coefficients for plunging, pitching, and rolling oscillations are calculated for two Mach Numbers.

TABLE OF NOTATION

$\bar{x}, \bar{y}, \bar{z}$	= Cartesian space coordinates
$\bar{t}, t$	= time
φ	= perturbation velocity potential
P	= pressure
ρ	= density
c	= acoustic velocity
L	= lift
M	= pitching moment
R	= rolling moment
$\bar{y}_p, \bar{y}_s$	= coordinates of the port and starboard leading edges
b	= semichord
ω	= frequency
x, y, z	= wing coordinates
$M = U/c$	= Mach Number
U	= free-stream velocity
$\nu = \omega b/U$	= reduced frequency
k	= $\nu M/\beta^2$
β^2	= $M^2 - 1$
σ	= sweep angle
S	= wing area
$q = (1/2)\rho_0 U^2$	= dynamic pressure
$C_L = L/qS$	= lift coefficient
$C_M = M/2bqS$	= pitching moment coefficient
l	= span
$C_l = R/qSl$	= rolling moment coefficient
α	= angle of attack
$\bar{p}$	= rate of roll
$()_a$	= Case a; plunging oscillation
$()_b$	= Case b; pitching oscillation
$()_c$	= Case c; rolling oscillation
$()_d$	= Case d; pitching oscillation of a flap

(I) INTRODUCTION

With the advent of high-performance aircraft and the possibility of supersonic flight, the problem of flutter and aerodynamic stability of airfoils moving at supersonic speeds has become of increasing importance. Consequently, much attention has been directed to the problem of an oscillating airfoil in a supersonic stream.

As in the case of the subsonic theory developed by Glauert,[1] von Kármán and Sears,[2] and others, the approach to the supersonic nonstationary problem has generally been made through the use of the linearized equations of motion. It is well known that, if one considers a nonviscous nonheat-conducting fluid with the assumptions of irrotationality and small disturbances, the equations that govern the disturbed motion of the fluid may be reduced to the wave equation. Under these conditions, it is possible to find general solutions of the wave equation which may be superimposed to satisfy the boundary condition of tangential flow on the wing surface.

Possio[3] and Borbely[4] have both treated the two-dimensional airfoil in this manner. These authors have obtained solutions for the pressures on an airfoil due to an arbitrary chordwise downwash distribution that exhibits a harmonic time dependence. These solutions are expressed as integrals that cannot be evaluated in terms of known functions. However, Schwarz[5] has calculated these integrals by numerical methods for a sufficient range of the parameters to make the use of this theory practical.

Garrick and Rubinow[6] and, recently, Miles,[7] following the early work of Possio and Borbely, have treated the two-dimensional theory as applied specifically to the flutter problem. These authors have obtained analytical expressions for the flutter derivatives in terms of integrals tabulated by Schwarz.

The work of Garrick and Rubinow, which includes some numerical results, indicates that for a certain range of Mach Numbers the aerodynamic damping due to torsional oscillations becomes negative; hence, the motion is unstable. This point is of paramount interest to the designer, and the question naturally arises as to what further instabilities may arise in the case of a finite wing.

Miles[8] has carried out an approximate solution of the problem of an oscillating delta wing, including only terms of first order in frequency. This analysis indicates that the instabilities found by Garrick and Rubinow may also occur for wings of finite span.

Recently, Stewart and Li[9] have obtained the solution for an oscillating rectangular wing. They have found that there is a marked change in the nature of

Received July 10, 1950.

* Research Analysis Section, Jet Propulsion Laboratory.

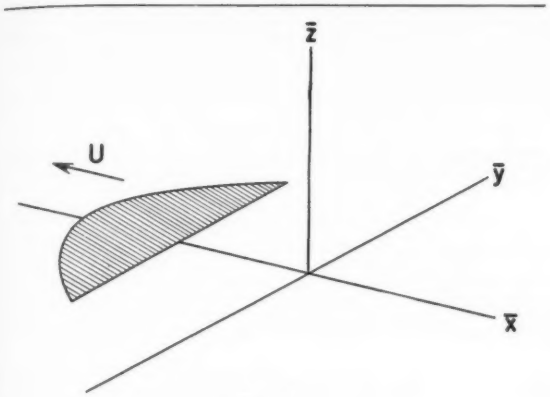

FIG. 1.

the damping of certain modes due to the finite aspect ratio.

The general solution for an oscillating three-dimensional wing with supersonic edges* may easily be expressed in terms of elementary solutions of the wave equation. However, even for relatively simple plan forms, the calculation of the pressures involves integrals much too difficult to evaluate. Fortunately, knowledge of pressure distributions is not of prime importance in the application of the theory. On the contrary, interest is centered on the nature of the total forces acting on the wing.

Miles[10] has pointed out that it is possible to reduce the problem of calculating the forces acting on an oscillating delta wing to an equivalent two-dimensional problem.† It is the purpose of this paper to present a general solution for the arbitrary motion of any three-dimensional wing having supersonic edges in terms of an equivalent two-dimensional problem. In the case of harmonic oscillations, the solution is expressed in terms of the familiar two-dimensional functions tabulated by Schwarz. This reduction is possible only if the trailing edge of the wing is straight and perpendicular to the direction of the free-stream velocity.

The specific example of an oscillating delta wing is considered. The forces acting on the wing due to rolling, plunging, and pitching oscillations are calculated for two Mach Numbers as a function of frequency.

(II) General Theory

Consider a wing contained in the $\bar{x}$, $\bar{y}$ plane which is extremely thin in the $\bar{z}$ direction and is moving in the direction of the negative $\bar{x}$ axis with a supersonic velocity U (Fig. 1). Let the wing perform any motion of small amplitude and small velocity about the plane $\bar{z} = 0$.

If the flow is assumed to be irrotational, a velocity potential may be introduced such that

$$\left.\begin{aligned} u &= \partial\varphi/\partial\bar{x} \\ v &= \partial\varphi/\partial\bar{y} \\ w &= \partial\varphi/\partial\bar{z} \end{aligned}\right\} \tag{1}$$

where u, v, and w are the components of the velocity of the fluid in the $\bar{x}$, $\bar{y}$, and $\bar{z}$ directions, respectively.

Since the disturbances are assumed to be small, the equations of motion for an inviscid nonheat-conducting fluid may be linearized to give

$$\frac{\partial^2\varphi}{\partial\bar{x}^2}+\frac{\partial^2\varphi}{\partial\bar{y}^2}+\frac{\partial^2\varphi}{\partial\bar{z}^2}-\frac{1}{c^2}\frac{\partial^2\varphi}{\partial\bar{t}^2}=0 \tag{2}$$

$$\left.\begin{aligned} \partial\varphi/\partial\bar{t} &= (P_0 - P)/\rho_0 \\ c^2 &= (dP/d\rho)_0 \end{aligned}\right\} \tag{3}$$

where P_0 and ρ_0 are the pressure and density far from the wing and c is the acoustic velocity.

The boundary condition on φ is expressed in terms of the downwash necessary to produce tangential flow over the wing. If $\bar{z}_w = \bar{z}(\bar{x}, \bar{y}, \bar{t})$ describes the altitude of points on the wing at the time $\bar{t}$, then the vertical velocity of the fluid adjacent to the wing will be given by

$$\partial\varphi/\partial\bar{z}(\bar{x}, \bar{y}, 0, \bar{t}) = -\mathrm{w}(\bar{x}, \bar{y}, \bar{t}) \tag{4}$$

where

$$\mathrm{w}(\bar{x}, \bar{y}, \bar{t}) = -\partial\bar{z}_w/\partial\bar{t} \tag{5}$$

If the edges of the wing are all supersonic, no disturbances will occur in the plane of the wing off the wing except in its wake. Furthermore, if the trailing edge is supersonic, the pressures on the wing are independent of conditions in its wake. Thus, the pressures on the wing are completely specified by Eqs. (2) through (5).

The problem represented by this system of equations can, in principle, be solved. However, in certain cases (harmonic oscillations, for example), the integrals encountered in the calculation of the pressures are so complicated that they have thus far resisted evaluation.

If only the total forces acting on the wing need be calculated, considerable simplification can be obtained. It has already been noted that, because of the hyperbolic nature of the differential equation and the assumption of supersonic edges, the two sides of the wing may be treated independently.‡ Further, since the wing is essentially a lamina, the downwash on the wing will be an even function of $\bar{z}$, and, hence, the over pressure will be an odd function of $\bar{z}$. Thus, it can be readily seen that the total lift acting on the wing will be given by

* It is common practice to refer to a wing boundary as being either subsonic or supersonic according to whether the normal component of the free-stream Mach Number is greater or less than 1.

† The publication in which Miles reported the results of his analysis[12] was brought to the author's attention after the completion of this manuscript. The present paper is in agreement with reference 12 on the results for the wide delta wing.

‡ This is equivalent to the statement that there are no disturbances in the plane of the wing off the wing.

$$L = 2\rho_0 \int\int_w [(P_0 - P)/\rho_0] dS$$

where the integral is evaluated over the upper surface of the wing. Introducing Eq. (3),

$$L = 2\rho_0 \int_{-U\bar{l}}^{-U\bar{l}+2b} \int_{\bar{y}_p(\bar{x}+U\bar{l})}^{\bar{y}_s(\bar{x}+U\bar{l})} \frac{\partial \varphi}{\partial \bar{l}} (\bar{x}, \bar{y}, 0, \bar{l})\, d\bar{y}\, d\bar{x} \quad (6)$$

where $\bar{y}_p$ and $\bar{y}_s$ are the extreme left- and right-hand coordinates, respectively, of the wing, $2b$ is the maximum dimension of the wing in the $\bar{x}$ direction, and

$$\bar{y}_p(0) = \bar{y}_s(0) = 0$$

In an analogous manner, the pitching moment about the point $\bar{x} = -U\bar{l}$ and the rolling moment about the $\bar{x}$ axis can be written as

$$M = -2\rho_0 \int_{-U\bar{l}}^{-U\bar{l}+2b} (\bar{x} + U\bar{l}) \int_{\bar{y}_p}^{\bar{y}_s} \frac{\partial \varphi}{\partial \bar{l}} (\bar{x}, \bar{y}, 0, \bar{l})\, d\bar{y}\, d\bar{x} \quad (7)$$

$$R = -2\rho_0 \int_{-U\bar{l}}^{-U\bar{l}+2b} \int_{\bar{y}_p}^{\bar{y}_s} \bar{y} \frac{\partial \varphi}{\partial \bar{l}} (\bar{x}, \bar{y}, 0, \bar{l})\, d\bar{y}\, d\bar{x} \quad (8)$$

Since it is known that $\partial\varphi/\partial\bar{l}(\bar{x}, \bar{y}, 0, \bar{l})$ is zero for $\bar{y} < \bar{y}_p$ and $\bar{y} > \bar{y}_s$, it is possible to extend the intervals of integration in the $\bar{y}$ direction without affecting the results. Thus, Eqs. (6), (7), and (8) may be written as

$$L = 2\rho_0 \int_{-U\bar{l}}^{-U\bar{l}+2b} \int_{-\infty}^{\infty} \frac{\partial \varphi}{\partial \bar{l}} (\bar{x}, \bar{y}, 0, \bar{l})\, d\bar{y}\, d\bar{x} \quad (9)$$

$$m = -2\rho_0 \int_{-U\bar{l}}^{-U\bar{l}+2b} (\bar{x} + U\bar{l}) \times \int_{-\infty}^{\infty} \frac{\partial \varphi}{\partial \bar{l}} (\bar{x}, \bar{y}, 0, \bar{l})\, d\bar{y}\, d\bar{x} \quad (10)$$

$$R = -2\rho_0 \int_{-U\bar{l}}^{-U\bar{l}+2b} \int_{-\infty}^{\infty} \bar{y} \frac{\partial \varphi}{\partial \bar{l}} (\bar{x}, \bar{y}, 0, \bar{l})\, d\bar{y}\, d\bar{x} \quad (11)$$

The above equations indicate that, if the following two-dimensional functions are introduced,

$$\psi_1(\bar{x}, \bar{z}, \bar{l}) = \int_{-\infty}^{\infty} \varphi(\bar{x}, \bar{y}, \bar{z}, \bar{l})\, d\bar{y} \quad (12)$$

$$\psi_2(\bar{x}, \bar{z}, \bar{l}) = \int_{-\infty}^{\infty} \bar{y}\varphi(\bar{x}, \bar{y}, \bar{z}, \bar{l})\, d\bar{y} \quad (13)$$

the total forces and moments acting on the wing may be calculated without explicit knowledge of the solution for φ, provided that the functions ψ_1 and ψ_2 can be evaluated.* For, if Eqs. (12) and (13) are differentiated with respect to $\bar{l}$ and substituted into Eqs. (9), (10), and (11), the expressions for the forces become

$$L = 2\rho_0 \int_{-U\bar{l}}^{-U\bar{l}+2b} \frac{\partial \psi_1}{\partial \bar{l}} (\bar{x}, 0, \bar{l})\, d\bar{x} \quad (14)$$

$$M = -2\rho_0 \int_{-U}^{-U\bar{l}+2b} (\bar{x} + U\bar{l}) \frac{\partial \psi_1}{\partial \bar{l}} (\bar{x}, 0, \bar{l})\, d\bar{x} \quad (15)$$

$$R = -2\rho_0 \int_{-U\bar{l}}^{-U\bar{l}+2b} \frac{\partial \psi_2}{\partial \bar{l}} (\bar{x}, 0, \bar{l})\, d\bar{x} \quad (16)$$

The functions ψ_1 and ψ_2 have an important physical interpretation. $\partial\psi_1/\partial\bar{l}$ represents the lift of a spanwise element of the wing, and $\partial\psi_2/\partial\bar{l}$ represents the rolling moment contributed by a spanwise element of the wing.

It is now necessary to determine, if possible, the differential equations that these functions satisfy and the appropriate boundary conditions that must be imposed upon them. This can best be accomplished by examining the derivatives of ψ_1 and ψ_2. Consider ψ_1,

$$\left.\begin{aligned} \partial^2\psi_1/\partial\bar{x}^2 &= \int_{-\infty}^{\infty} (\partial^2\varphi/\partial\bar{x}^2)\, d\bar{y} \\ \partial^2\psi_1/\partial\bar{z}^2 &= \int_{-\infty}^{\infty} (\partial^2\varphi/\partial\bar{z}^2)\, d\bar{y} \\ \partial^2\psi_1/\partial\bar{l}^2 &= \int_{-\infty}^{\infty} (\partial^2\varphi/\partial\bar{l}^2)\, d\bar{y} \end{aligned}\right\} \quad (17)$$

Since, from physical considerations, infinite velocities and pressures in the flow field are not allowed, φ is at least a piecewise continuous function of the independent variables. Therefore, the integral of Eq. (12) exists in the ordinary sense. However, φ may have discontinuities in its first derivatives. Therefore, the integrals of Eq. (17) must be considered as Stieltjes integrals. The derivatives defined by Eq. (17) will thus have meaning whenever the Stieltjes integrals exist.

For values of $\bar{x}$, $\bar{z}$, $\bar{l}$, such that the second derivatives of φ exist, ψ_1 satisfies the equation

$$\frac{\partial^2\psi_1}{\partial\bar{x}^2} + \frac{\partial^2\psi_1}{\partial\bar{z}^2} - \frac{1}{c^2}\frac{\partial^2\psi_1}{\partial\bar{l}^2} = \int_{-\infty}^{\infty} \left[\frac{\partial^2\varphi}{\partial\bar{x}^2} + \frac{\partial^2\varphi}{\partial\bar{z}^2} - \frac{1}{c^2}\frac{\partial^2\varphi}{\partial\bar{l}^2}\right] d\bar{y}$$

or, from Eq. (2),

$$\frac{\partial^2\psi_1}{\partial\bar{x}^2} + \frac{\partial^2\psi_1}{\partial\bar{z}^2} - \frac{1}{c^2}\frac{\partial^2\psi_1}{\partial\bar{l}^2} = -\int_{-\infty}^{\infty} \frac{\partial^2\varphi}{\partial\bar{y}^2}\, d\bar{y} \quad (18)$$

Since the sidewash must vanish at infinity, the right-hand side of Eq. (18) may be integrated to give

$$\frac{\partial^2\psi_1}{\partial\bar{x}^2} + \frac{\partial^2\psi_1}{\partial\bar{z}^2} - \frac{1}{c^2}\frac{\partial^2\psi_1}{\partial\bar{l}^2} = 0 \quad (19)$$

For certain values of $\bar{x}$, $\bar{z}$, and $\bar{l}$, terms of Eq. (19) may not be defined. This is to be expected, since Eq. (19) is a hyperbolic differential equation. The boundary condition on ψ_1 may be obtained in a similar manner. Consider

$$\partial\psi_1/\partial\bar{z} = \int_{-\infty}^{\infty} (\partial\varphi/\partial\bar{z})\, d\bar{y}$$

If the trailing edge of the wing is straight and perpendicular to the $\bar{x}$ axis and if the leading edges are supersonic, Eq. (4) gives

$$\frac{\partial\psi_1}{\partial\bar{z}} (\bar{x}, 0, \bar{l}) = -\int_{\bar{y}_p}^{\bar{y}_s} w(\bar{x}, \bar{y}, \bar{l})\, d\bar{y} = -w_1(\bar{x}, \bar{l}) \quad (20)$$

$$(0 < \bar{x} + U\bar{l} < 2b)$$

* This possibility was suggested by Dr. P. A. Lagerstrom.

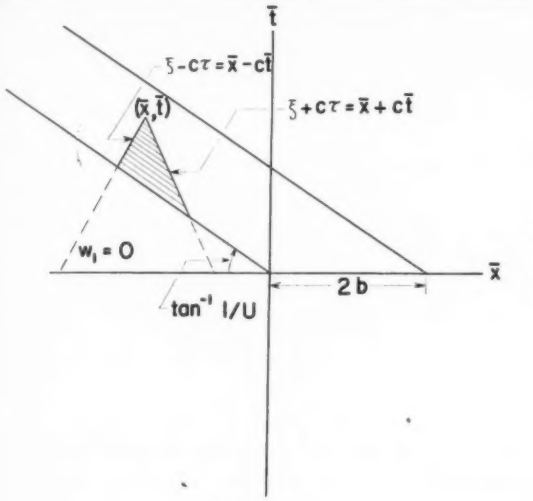

FIG. 2.

where $w(\bar{x}, \bar{y}, \bar{t})$ is the downwash on the wing. Also,

$$\partial\psi_1/\partial\bar{z}(\bar{x}, 0, \bar{t}) = 0 \quad (\bar{x} + U\bar{t} < 0)$$

The solution to Eqs. (19) and (20) is well known. For points on the wing, the solution is

$$\psi_1(\bar{x}, 0, \bar{t}) = \frac{c}{\pi}\int_0 \int_{\bar{x}-c(\bar{t}-\tau)}^{\bar{x}+c(\bar{t}-\tau)} \frac{w_1(\xi, \tau)\, d\xi\, d\tau}{\sqrt{c^2(\bar{t}-\tau)^2 - (x-\xi)^2}} \tag{21}$$

The region of integration in the $\bar{x}, \bar{t}$ plane is illustrated in Fig. 2. Now consider ψ_2,

$$\left.\begin{aligned} \partial^2\psi_2/\partial\bar{x}^2 &= \int_{-\infty}^{\infty} \bar{y}(\partial^2\varphi/\partial\bar{x}^2)\, d\bar{y} \\ \partial^2\psi_2/\partial\bar{z}^2 &= \int_{-\infty}^{\infty} \bar{y}(\partial^2\varphi/\partial\bar{z}^2)\, d\bar{y} \\ \partial^2\psi_2/\partial\bar{t}^2 &= \int_{-\infty}^{\infty} \bar{y}(\partial^2\varphi/\partial\bar{t}^2)\, d\bar{y} \end{aligned}\right\} \tag{22}$$

Here, the presence of $\bar{y}$ in the integrand introduces no convergence difficulties because φ and all of its derivatives are zero outside of a finite $\bar{y}$ interval. From Eq. (2),

$$\frac{\partial^2\psi_2}{\partial\bar{x}^2} + \frac{\partial^2\psi_2}{\partial\bar{z}^2} - \frac{1}{c^2}\frac{\partial^2\psi_2}{\partial\bar{t}^2} = -\int_{-\infty}^{\infty} \bar{y}\frac{\partial^2\varphi}{\partial\bar{y}^2} d\bar{y} \tag{23}$$

and

$$\varphi = \frac{\partial\varphi}{\partial\bar{y}} = \frac{\partial^2\varphi}{\partial\bar{y}^2} = 0 \quad [|\bar{y}| \geqslant Y(\bar{x}, \bar{z}, \bar{t})]$$

The right-hand side of Eq. (23) may thus be written

$$\int_{-\infty}^{\infty} \bar{y}\frac{\partial^2\varphi}{\partial\bar{y}^2} d\bar{y} = \int_{-Y}^{Y} \bar{y}\frac{\partial^2\varphi}{\partial\bar{y}^2} d\bar{y} = \left[\bar{y}\frac{\partial\varphi}{\partial\bar{y}}\right]_{-Y}^{Y} - \int_{-Y}^{Y} \frac{\partial\varphi}{\partial\bar{y}} d\bar{y} = 0$$

Therefore,

$$\partial^2\psi_2/\partial\bar{x}^2 + \partial^2\psi_2/\partial\bar{z}^2 - 1/c^2(\partial^2\psi_2/\partial\bar{t}^2) = 0 \tag{24}$$

The boundary condition on ψ_2 becomes

$$\left.\begin{aligned} \frac{\partial\psi_2}{\partial\bar{z}}(\bar{x}, 0, \bar{t}) &= -\int_{\bar{y}_p}^{\bar{y}_s} \bar{y}w(\bar{x}, \bar{y}, \bar{t})\, d\bar{y} = -w_2(\bar{x}, \bar{t}) \\ &\qquad (0 < \bar{x} + U\bar{t} < 2b) \\ \partial\psi_2/\partial\bar{z}(\bar{x}, 0, \bar{t}) &= 0 \quad (\bar{x} + U\bar{t} < 0) \end{aligned}\right\} \tag{25}$$

The solution for ψ_2 for points on the wing may be written down immediately as

$$\psi_2(\bar{x}, 0, \bar{t}) = \frac{c}{\pi}\int_0 \int_{\bar{x}-c(\bar{t}-\tau)}^{\bar{x}+c(\bar{t}-\tau)} \frac{w_2(\xi, \tau)\, d\xi\, d\tau}{\sqrt{c^2(\bar{t}-\tau)^2 - (x-\xi)^2}} \tag{26}$$

The original three-dimensional problem has now been reduced to an equivalent two-dimensional problem. The methods previously used for two-dimensional wings can be applied to obtain the forces acting on the wing.

The solutions represented by Eqs. (21) and (26) are general and apply to any downwash distribution, such as gust loading, unit step loading, or accelerated flight. The special case that will be of interest here is the downwash distribution that, at any point on the wing, has a harmonic time dependence. This condition is

$$\partial\varphi/\partial\bar{z}(\bar{x}, \bar{y}, 0, \bar{t}) = -w(\bar{x} + U\bar{t}, \bar{y})e^{j\omega}$$

or, from Eq. (20),

$$\frac{\partial\psi_1}{\partial\bar{z}}(\bar{x}, 0, \bar{t}) = -\int_{\bar{y}_p(\bar{x}+U\bar{t})}^{\bar{y}_s(\bar{x}+U\bar{t})} w(\bar{x} + U\bar{t}, y)e^{j\omega\bar{t}}\, d\bar{y} = -w_1(\bar{x} + U\bar{t})e^{j\omega} \tag{27}$$

and from Eq. (25),

$$\frac{\partial\psi_2}{\partial\bar{z}}(\bar{x}, 0, \bar{t}) = -\int_{\bar{y}_p(\bar{x}+U\bar{t})}^{\bar{y}_s(\bar{x}+U\bar{t})} \bar{y}w(\bar{x} + U\bar{t}, \bar{y})e^{j\omega\tau}\, d\bar{y} = -w_2(\bar{x} + U\bar{t})e^{j\omega\bar{t}} \tag{28}$$

With these boundary conditions, the expressions for ψ_1 and ψ_2 can be simplified. Consider Eq. (21). Using Eq. (27),

$$\psi_1(\bar{x}, 0, \bar{t}) = \frac{c}{\pi}\int_0 \int_{\bar{x}-c(\bar{t}-\tau)}^{\bar{x}+c(\bar{t}-\tau)} \frac{w_1(\xi + U\tau)e^{j\omega\tau}\, d\xi\, d\tau}{\sqrt{c^2(\bar{t}-\tau)^2 - (\bar{x}-\xi)^2}} \tag{29}$$

Introducing the Galilean transformation

$$x = \bar{x} + U\bar{t}, \quad y = \bar{y}$$
$$z = \bar{z}, \quad t = \bar{t}$$

and integrating first along $\xi + U\tau$ = constant, Eq. (29) yields the well-known integral relation (see, for example, reference 4 or 7)

$$\psi_1(x, 0, t) = \frac{e^{j\omega}}{\beta} \int_0^x w_1(s) J_0\left[\frac{k(x - s)}{b}\right] e^{-jkM(x-s)/b}\, ds \tag{30}$$

where

$$M = U/c$$
$$\beta^2 = M^2 - 1$$
$$k = \omega b/c\beta^2$$

and J_0 is the Bessel function of the first kind of zero order. Similarly,

$$\psi_2(x, 0, t) = \frac{e^{j\omega t}}{\beta} \int_0^x w_2(s) J_0\left[\frac{k(x - s)}{b}\right] e^{-jkM(x-s)}\, ds \tag{31}$$

The calculation of ψ_1 and ψ_2 has been reduced to the evaluation of a single integral. The calculation of the forces and moments requires another integration. In many cases of interest, $w_1(x)$ and $w_2(x)$ are polynomials in x.. When this is true, it will be demonstrated that the expressions for the forces and moments reduce to the single integrals tabulated by Schwarz. The special case of an oscillating delta wing will now be considered.

(III) The Delta Wing

The functions ψ_1 and ψ_2 will now be used to calculate the aerodynamic forces acting on an oscillating delta wing. The plan form of the wing is an isosceles triangle with a vertex angle of $\pi - 2\sigma$ (Fig. 3). The vertex is placed at the origin of the x, y, z coordinate system. The maximum chord of the wing is $2b$. Three types of motion will be considered: plunging, pitching, and rolling oscillations.

Case a: Plunging Oscillation

This motion is characterized by a downwash that is the same for each point on the wing. Analytically, this is expressed by

$$\partial\varphi/\partial z(x, y, 0, t) = -w_0 e^{j\omega t}$$

or

$$w(x, y) = w_0 = \text{constant}$$

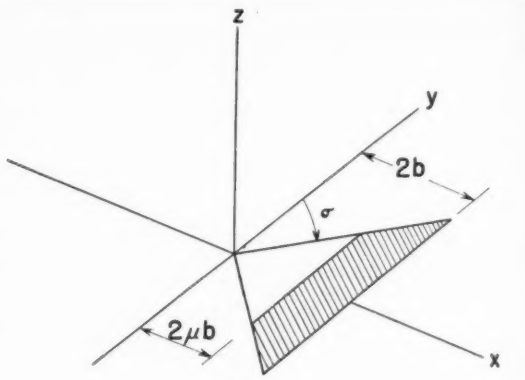

FIG. 3.

The leading edge of the wing is described by the equations

$$y_p = -x/\tan\sigma, \quad y_s = x/\tan\sigma \tag{32}$$

Now from Eq. (27)

$$w_1(x) = \int_{-x/\tan\sigma}^{x/\tan\sigma} w_0\, dy = 2w_0 x/\tan\sigma \tag{33}$$

Substituting Eq. (33) into Eq. (30),

$$\psi_1(x, 0, t) = \frac{2w_0 e^{j\omega t}}{\beta \tan\sigma} \int_0^x sG(x - s)\, ds \tag{34}$$

where

$$G(x - s) = J_0\left[\frac{k(x - s)}{b}\right] e^{-jkM(x-s)/b} \tag{35}$$

It will often be convenient to express integrals of the type appearing in Eq. (34) in slightly different form. A change of the variable of integration establishes the following relation:

$$\int_0^x f(s)h(x - s)\, ds = \int_0^x f(x - s)h(s)\, ds \tag{36}$$

With the aid of the Galilean transformation introduced in the previous section, Eq. (14) becomes

$$L = 2\rho_0 \int_0^{2b} [(\partial\psi_1/\partial t) + U(\partial\psi_1\partial/\partial x)]\, dx \tag{37}$$

Substituting Eq. (34) and using the relation of Eq. (36),

$$L = 2\rho_0 \int_0^{2b} \left[\frac{\partial}{\partial t} + U\frac{\partial}{\partial x}\right] \frac{2w_0 e^{j\omega t}}{\beta \tan\sigma} \int_0^x (x - s)G(s)\, ds\, dx$$

or

$$L = \frac{4\rho_0 w_0 e^{j\omega t}}{\beta \tan\sigma}\left[j\omega \int_0^{2b}\int_0^x (x - s)G(s)\, ds\, dx + U\int_0^{2b}\int_0^x G(s)\, ds\, dx\right]$$

Since the area of the wing is $S = 4b^2/\tan\sigma$ and the dynamic pressure is $q = (1/2)\rho_0 U^2$, the lift coefficient becomes

$$C_L = \frac{2w_0 e^{j\omega t}}{\beta U^2 b^2}\left[j\omega \int_0^{2b}\int_0^x (x - s)G(s)\, ds\, dx + U\int_0^{2b}\int_0^x G(s)\, ds\, dx\right] \tag{38}$$

It is interesting to note that the C_L is independent of the sweep angle σ. It will be found that this is true for all of the coefficients considered in this analysis.

Introducing the quasi-steady value for the lift coefficient $C_{L_0} = (4w_0 e^{j\omega t})/\beta U$, Eq. (38) becomes

$$\left(\frac{C_L}{C_{L_0}}\right)_a = \frac{j\omega}{2Ub^2}\int_0^{2b}\int_0^x (x-s)G(s)\,ds\,dx + \frac{1}{2b^2}\int_0^{2b}\int_0^x G(s)\,ds\,dx \tag{39}$$

Now, if the variables of integration are changed by $x = 2b\,\xi$ and $s = 2b\,\eta$, then

$$\left(\frac{C_L}{C_{L_0}}\right)_a = 4j\nu\int_0^1\int_0^\xi (\xi-\eta)G(2b\eta)\,d\eta\,d\xi + 2\int_0^1\int_0^\xi G(2b\eta)\,d\eta\,d\xi \tag{40}$$

where $\nu = \omega b/U$. Finally, Eq. (40) can be integrated by parts to give

$$(C_L/C_{L_0}) = j\nu[T_0 - T_1 + (1/4)T_2] + T_0 - (1/2)T_1 \tag{41}$$

where

$$T_n = 2^{n+1}\int_0^1 s^n G(2bs)\,ds \tag{42}$$

The stalling moment about the vertex of the wing is obtained from Eq. (15),

$$M = -\frac{4\rho_0 w_0 e^{j\omega t}}{\beta\tan\sigma}\left[j\omega\int_0^{2b} x\int_0^x (x-s)G(s)\,ds\,dx + U\int_0^{2b} x\int_0^x G(s)\,ds\,dx\right] \tag{43}$$

Now, $C_M = M/qS2b$, and the quasi-steady value of C_M is $C_{M_0} = -(8w_0 e^{j\omega t})/3\beta U$. Therefore, by integrating by parts and using Eq. (42), the final expression becomes

$$(C_M/C_{M_0})_a = j\nu[T_0 - (3/4)T_1 + (1/16)T_3] + (3/4)T_0 - (3/16)T_2 \tag{44}$$

Since the wing is symmetrical about the x-axis and the downwash is an even function of y for this mode of oscillation, the total rolling moment about the x-axis is zero.

Case b: Pitching Oscillation

In this case, the wing is assumed to be pitching about an axis a distance $2\mu b$ downstream of the vertex. The instantaneous angle of attack is given by

$$\alpha = \alpha_0 e^{j\omega t} \tag{45}$$

where α_0 = constant. Therefore, the z coordinate of any point on the wing is

$$z_w = -\alpha(x - 2\mu b)$$

and the downwash necessary to produce tangential flow over the wing is

$$\frac{\partial\varphi}{\partial z} = \frac{\partial z_w}{\partial t} + U\frac{\partial z_w}{\partial x} = -\alpha_0 e^{j\omega t}\,[j\omega(x - 2\mu b) + U]$$

or

$$w(x, y) = (1 - 2j\nu\mu)U\alpha_0 + j\nu\alpha_0 U(x/b) \tag{46}$$

The first term on the right-hand side of Eq. (46) corresponds to the downwash used in Case a. Therefore, it is only necessary to obtain a solution for the parabolic downwash,

$$w_p = (\alpha_0 Ux)/b$$

From Eq. (27),

$$w_1(x) = \int_{-x/\tan\sigma}^{x/\tan\sigma}\frac{\alpha_0 Ux}{b}\,dy = \frac{2\alpha_0 Ux^2}{b\tan\sigma}$$

and, from Eq. (30),

$$\psi_1(x, 0, t) = \frac{2\alpha_0 Ue^{j\omega t}}{\beta b\tan\sigma}\int_0^x (x-s)^2 G(s)\,ds \tag{47}$$

Introducing Eq. (47) into Eq. (14),

$$L_p = \frac{4\rho_0\alpha_0 Ue^{j\omega t}}{\beta b\tan\sigma}\left[j\omega\int_0^{2b}\int_0^x (x-s)^2 G(s)\,ds\,dx + 2U\int_0^{2b}\int_0^x (x-s)G(s)\,ds\,dx\right]$$

Dividing by qS and integrating by parts,

$$C_{L_p} = \frac{16\alpha_0 e^{j\omega t}}{3\beta}\left[j\nu\left(T_0 - \frac{3}{2}T_1 + \frac{3}{4}T_2 - \frac{1}{8}T_3\right) + \frac{3}{2}T_0 - \frac{3}{2}T_1 + \frac{3}{8}T_2\right]$$

A comparison of this expression with Eqs. (41) and (44) leads to the following result:

$$C_{L_p} = (16\alpha_0 e^{j\omega t}/3\beta)[3(C_L/C_{L_0})_a - 2(C_M/C_{M_0})_a] \tag{48}$$

Since the differential equations that are being solved are linear, it is permissible to superimpose solutions. Therefore, from Eq. (46),

$$C_{L_b} = (1 - 2j\nu\mu)(U\alpha_0/w_0)C_{L_a} + j\nu C_{L_p}$$

For this case, the quasi-steady C_L is given by

$$(C_{L_0})_b = (4\alpha_0/\beta)e^{j\omega t} = (\alpha_0 U/w_0)(C_{L_0})_a$$

so that

$$(C_L/C_{L_0})_b = (1 - 2j\nu\mu + 4j\nu)(C_L/C_{L_0})_a - (8j\nu/3)(C_M/C_{M_0})_a \tag{49}$$

It is now necessary to calculate the moment about the vertex due to the parabolic downwash. From Eqs. (15) and (47),

$$M_p = -\frac{4\rho_0\alpha_0 U e^{j\omega t}}{\beta b \tan\sigma}\left[j\omega \int_0^{2b} x \int_0^x (x - s)^2 G(s)\, ds\, dx + 2U \int_0^{2b} x \int_0^x (x - s) G(s)\, ds\, dx\right]$$

By a change of variable and integration by parts,

$$C_{M_p} = -\frac{4\alpha_0 e^{j\omega t}}{\beta}\left[j\nu\left(T_0 - \frac{4}{3}T_1 + \frac{1}{2}T_2 - \frac{1}{48}T_4\right) + \frac{4}{3}T_0 - T_1 + \frac{1}{12}T_3\right]$$

Since

$$(C_{M_b})_{x=0} = (1 - 2j\nu\mu)(U\alpha_0/w_0)C_{M_a} + j\nu C_{M_p}$$

the total moment coefficient about the vertex is

$$(C_{M_b})_{x=0} = -(8\alpha_0 e^{j\omega t}/3\beta)(1 - 2j\nu\mu)(C_M/C_{M_0})_a + j\nu C_{M_p}$$

In the case of pitching motions, it is generally desirable to calculate the pitching moment about the axis of rotation. If $(C_{M_b})_\mu$ is the pitching moment coefficient about the axis of rotation, then

$$(C_{M_b})_\mu = (C_{M_b})_{x=0} + \mu C_{L_b}$$

Since the quasi-steady value for $(C_{M_b})_\mu$ is

$$(C_{M_0})_\mu = [4\alpha_0(3\mu - 2)/3\beta]e^{j\omega t}$$

then

$$\left(\frac{C_M}{C_{M_0}}\right)_{b\mu} = \frac{1}{2 - 3\mu}\left[2(1 - 2j\nu\mu)\left(\frac{C_M}{C_{M_0}}\right)_a - 3\mu\left(\frac{C_L}{C_{L_0}}\right)_b + j\nu\left(\frac{C_M}{C_{M_0}}\right)_p\right] \tag{50}$$

where

$$\left(\frac{C_M}{C_{M_0}}\right)_p = j\nu\left(3T_0 - 4T_1 + \frac{3}{2}T_2 - \frac{1}{16}T_4\right) + 4T_0 - 3T_1 + \frac{1}{4}T_3 \tag{51}$$

In this case the downwash is again symmetrical about the x-axis, and the rolling moment is therefore zero.

Case c: Rolling Oscillation

In this case the motion of the wing and, hence, the downwash will be specified by the rate of roll ϕ. Thus, if $\phi = pe^{j\omega t}$, then $w(x, y) = py$. Since the downwash is antisymmetrical with respect to the x-axis, the lift and pitching moment will be zero. It is therefore only necessary to calculate the rolling moment.

From Eq. (28),

$$w_2(x) = \int_{-x/\tan\sigma}^{x/\tan\sigma} py^2\, dy = 2px^3/3\tan^3\sigma \tag{52}$$

Introducing this into Eq. (31),

$$\psi_2(x, 0, t) = (2pe^{j\omega t}/3\beta\tan^3\sigma)\int_0^x (x - s)^3 G(s)\, ds \tag{53}$$

The rolling moment is obtained from Eq. (16):

$$R = -\frac{4\rho_0 p e^{j\omega t}}{3\beta \tan^3 \sigma}\left[j\omega \int_0^{2b}\int_0^x (x-s)^3 G(s)\, ds\, dx + 3U \int_0^{2b}\int_0^x (x-s)^2 G(s)\, ds\, dx \right]$$

If the rolling moment coefficient is defined as $C_l = R/qSl$, where $l = 4b/\tan\sigma$ = span of wing, then

$$C_l = -\frac{2lpe^{j\omega t}}{3\beta U}\left[2j\nu \int_0^1\int_0^\xi (\xi-\eta)^3 G(2b\eta)\, d\eta\, d\xi + 3\int_0^1\int_0^\xi (\xi-\eta)^2 G(2b\eta)\, d\eta\, d\xi \right]$$

Since the quasi-steady value for the C_l is

$$C_{l_0} = -lpe^{j\omega t}/6\beta U \tag{54}$$

and using Eqs. (42) and (54), together with the results of Case a and Case b, the final result becomes

$$(C_l/C_{l_0})_c = 12(C_L/C_{L_0})_a - 8(C_M/C_{M_0})_a - (C_M/C_{M_0})_p \tag{55}$$

Note that for a given span the rolling moment coefficient is independent of the sweep angle.

Case d: Oscillating Flap

The final case investigated is that of a flap oscillating about its hinge axis. The flap considered consists of the aft portion of a delta wing (Fig. 3). The hinge line is perpendicular to the x-axis. The chord of the flap is $(1-\mu)2b$. The portion of the wing forward of the hinge line remains at zero angle of attack.

Under the above conditions, the expression for the downwash is

$$\begin{aligned} w(x, y) &= 0 && (x < 2\mu b) \\ w(x, y) &= \alpha_0 U[1 - 2j\nu\mu + (j\nu x/b)] && (2\mu b < x < 2b) \end{aligned}$$

From Eq. (27),

$$\begin{aligned} w_1(x) &= 0 && (x < 2\mu b) \\ w_1(x) &= \frac{2\alpha_0 Ux}{\tan\sigma}\left(1 - 2j\nu\mu + \frac{j\nu x}{b}\right) && (2\mu b < x < 2b) \end{aligned}$$

and, from Eq. (30),

$$\psi_1(x, 0, t) = 0 \quad (x < 2\mu b)$$

$$\psi_1(x, 0, t) = \frac{2\alpha_0 U e^{j\omega t}}{\beta \tan\sigma}\int_{2\mu b}^x \left(1 - 2j\nu\mu + \frac{j\nu s}{b}\right) sG(x-s)\, ds \quad (2\mu b < x < 2b) \tag{56}$$

but the lift is given by

$$L = 2\rho_0 \int_{2\mu b}^{2b} [(\partial\psi_1/\partial t) + (\partial\psi_1/\partial x)U]\, dx$$

and $\partial\psi_1/\partial t = j\omega\psi_1$. Integrating the second term of the equation for lift,

$$L = 2\rho_0\left[j\omega \int_{2\mu b}^{2b} \psi_1\, dx + U\psi_1(2b, 0, t)\right]$$

which becomes, on substituting Eq. (56),

$$L = \frac{4\rho_0\alpha_0 U e^{j\omega t}}{\beta \tan\sigma}\left[j\omega \int_{2\mu b}^{2b}\int_{2\mu b}^x \left(1 - 2j\nu\mu + \frac{j\nu s}{b}\right) sG(x-s)\, ds\, dx + U\int_{2\mu b}^{2b}\left(1 - 2j\nu\mu + \frac{j\nu s}{b}\right) sG(2b-s)\, ds\right]$$

Since the area of the flap is

$$S_f = 4b^2(1-\mu^2)/\tan\sigma$$

some algebraic manipulation leads to the following expression for the C_L:

$$C_L = \frac{8\alpha_0 e^{j\omega t}}{\beta(1+\mu)}\left\{ 2j\nu(1-\mu)\int_0^1\int_0^x [1 + 2j\nu(1-\mu)(x-s)][(1-\mu)(x-s) + \mu]G[2b(1-\mu)s]\, ds\, dx + \right.$$

$$\left. \int_0^1 [1 + 2j\nu(1-\mu)(1-s)][(1-\mu)(1-s) + \mu]G[2b(1-\mu)s]\, ds \right\}$$

It is now convenient to adopt the following convention. If $F = F(b)$, then $F' = F(b')$, where $b' = (1 - \mu)b$. This convention makes it possible to use expressions previously obtained but with the reduced frequency ν' based on the chord of the flap.

The expression for the C_L can now be reduced in the usual manner using Eq. (42). The result, in terms of expressions already obtained, is

$$\left(\frac{C_L}{C_{L_0}}\right)_d = \frac{2}{1+\mu}\left\{\mu\left[\frac{1}{2}T_0' + j\nu'\left(T_0' - \frac{1}{2}T_1'\right)\right] + \frac{1}{2}(1 - \mu + 4j\nu' - 2j\nu'\mu)\left(\frac{C_L}{C_{L_0}}\right)_a' - \frac{4j\nu'(1-\mu)}{3}\left(\frac{C_M}{C_{M_0}}\right)_a'\right\} \quad (57)$$

where the quasi-steady lift coefficient of the flap is given by $C_{L_0} = 4\alpha_0 e^{j\omega t}/\beta$.

The pitching moment about the hinge axis is

$$M = -2\rho_0 \int_{2\mu b}^{2b} [(\partial\psi_1/\partial t) + U(\partial\psi_1/\partial x)](x - 2\mu b)\, dx$$

The second term can be integrated by parts to give

$$M = -2\rho_0\left[j\omega \int_{2\mu b}^{2b} (x - 2\mu b)\psi_1\, dx + 2bU(1-\mu)\psi_1(2b, 0, t) - U\int_{2\mu b}^{2b} \psi_1\, dx\right]$$

Using Eq. (56),

$$M = -\frac{4\rho_0\alpha_0 U e^{j\omega t}}{\beta \tan\sigma}\left[j\omega \int_{2\mu b}^{2b} (x - 2\mu b)\int_{2\mu b}^{x}\left(1 - 2j\nu\mu + \frac{j\nu s}{b}\right)sG(x-s)\, ds\, dx + 2b(1-\mu)U \times \right.$$
$$\left. \int_{2\mu b}^{2b}\left(1 - 2j\nu\mu + \frac{j\nu s}{b}\right)sG(2b - s)\, ds - U\int_{2\mu b}^{2b}\int_{2\mu b}^{x}\left(1 - 2j\nu\mu + \frac{j\nu s}{b}\right)sG(x-s)\, ds\, dx\right]$$

Proceeding exactly as in the case of the C_L, the final result is

$$\left(\frac{C_M}{C_{M_0}}\right)_d = \frac{6}{2+\mu}\left\{\mu\left[\frac{1}{4}T_1' + j\nu'\left(\frac{1}{2}T_0' - \frac{1}{8}T_2'\right)\right] + \frac{1}{3}(1 - \mu + 2j\nu'\mu)\left(\frac{C_M}{C_{M_0}}\right)_a' + \frac{j\nu'(1-\mu)}{6}\left(\frac{C_M}{C_{M_0}}\right)_p'\right\} \quad (58)$$

where

$$C_{M_0} = -[4\alpha_0(2+\mu)/3\beta(1+\mu)]e^{j\omega t}$$

Here, the C_M is based on the chord of the flap.

TABLE 1
$M = 1.25$
(Cases b and d; $\mu = 0.5$)

$2kM$	$R\left(\frac{C_L}{C_{L_0}}\right)_a$	$I\left(\frac{C_L}{C_{L_0}}\right)_a$	$R\left(\frac{C_M}{C_{M_0}}\right)_a$	$I\left(\frac{C_M}{C_{M_0}}\right)_a$	$R\left(\frac{C_L}{C_{L_0}}\right)_b$	$I\left(\frac{C_L}{C_{L_0}}\right)_b$	$R\left(\frac{C_M}{C_{M_0}}\right)_{b\mu}$	$I\left(\frac{C_M}{C_{M_0}}\right)_{b\mu}$
0.6	0.9720	−0.0996	0.9665	−0.1375	0.9722	−0.0862	0.9545	−0.0727
1.0	0.9263	−0.1572	0.9120	−0.2110	0.9276	−0.1277	0.8832	−0.0919
1.4	0.8662	−0.2035	0.8413	−0.2611	0.8710	−0.1489	0.7970	−0.0742
1.8	0.8001	−0.2364	0.7647	−0.2851	0.8124	−0.1460	0.7136	−0.0206
2.2	0.7359	−0.2552	0.6922	−0.2847	0.7581	−0.1283	0.6500	0.0659
2.6	0.6798	−0.2612	0.6314	−0.2654	0.7161	−0.0952	0.6138	0.1670
3.4	0.6044	−0.2444	0.5576	−0.1997	0.6727	−0.0152	0.6210	0.3611
4.2	0.5726	−0.2119	0.5364	−0.1400	0.6670	0.0510	0.6827	0.4918
5.0	0.5613	−0.1793	0.5356	−0.1052	0.6686	0.0968	0.7271	0.5703

$2kM$	$R\left(\frac{C_L}{C_{L_0}}\right)_c$	$I\left(\frac{C_L}{C_{L_0}}\right)_c$	$R\left(\frac{C_L}{C_{L_0}}\right)_d$	$I\left(\frac{C_L}{C_{L_0}}\right)_d$	$R\left(\frac{C_M}{C_{M_0}}\right)_d$	$I\left(\frac{C_M}{C_{M_0}}\right)_d$
0.6	0.9867	−0.0743	0.9673	−0.0431	0.9556	−0.0491
1.0	0.9694	−0.1212	0.9158	−0.0510	0.8866	−0.0523
1.4	0.9424	−0.1612	0.8526	−0.0343	0.8039	−0.0200
1.8	0.9097	−0.1936	0.7903	0.0086	0.7265	0.0479
2.2	0.8738	−0.2180	0.7391	0.0722	0.6680	0.1426
2.6	0.8367	−0.2343	0.7051	0.1476	0.6364	0.2499
3.4	0.7656	−0.2460	0.6869	0.2970	0.6442	0.4479
4.2	0.7096	−0.2373	0.6878	0.4117	0.6841	0.5821
5.0	0.6675	−0.2195	0.6998	0.5016	0.6927	0.6800

TABLE 2
$M = 2.00$
(Cases b and d; $\mu = 0.5$)

$2kM$	$R\left(\frac{C_L}{C_{L_0}}\right)_a$	$I\left(\frac{C_L}{C_{L_0}}\right)_a$	$R\left(\frac{C_M}{C_{M_0}}\right)_a$	$I\left(\frac{C_M}{C_{M_0}}\right)_a$	$R\left(\frac{C_L}{C_{L_0}}\right)_b$	$I\left(\frac{C_L}{C_{L_0}}\right)_b$	$R\left(\frac{C_M}{C_{M_0}}\right)_{b\mu}$	$I\left(\frac{C_M}{C_{M_0}}\right)_{b\mu}$
0.6	0.9890	−0.0389	0.9868	−0.0539	0.9892	0.0274	0.9839	0.1542
1.0	0.9707	−0.0618	0.9651	−0.0832	0.9718	0.0521	0.9591	0.2685
1.4	0.9461	−0.0804	0.9360	−0.1036	0.9499	0.0853	0.9300	0.3971
1.8	0.9181	−0.0937	0.9033	−0.1135	0.9274	0.1278	0.9040	0.5404
2.2	0.8897	−0.1013	0.8708	−0.1127	0.9081	0.1785	0.8880	0.6954
2.6	0.8637	−0.1032	0.8420	−0.1025	0.8951	0.2352	0.8863	0.8560
3.4	0.8269	−0.0927	0.8049	−0.0638	0.8919	0.3525	0.9274	1.1739
4.2	0.8144	−0.0708	0.7985	−0.0205	0.9117	0.4555	0.9990	1.4240
5.0	0.8203	−0.0468	0.8135	0.0098	0.9342	0.5356	1.0508	1.6285

$2kM$	$R\left(\frac{C_l}{C_{l_0}}\right)_c$	$I\left(\frac{C_l}{C_{l_0}}\right)_c$	$R\left(\frac{C_L}{C_{L_0}}\right)_d$	$I\left(\frac{C_L}{C_{L_0}}\right)_d$	$R\left(\frac{C_M}{C_{M_0}}\right)_d$	$I\left(\frac{C_M}{C_{M_0}}\right)_d$
0.6	0.9955	−0.0296	0.9927	0.1848	0.9902	0.2346
1.0	0.9879	−0.0476	0.9813	0.3119	0.9745	0.3966
1.4	0.9771	−0.0634	0.9657	0.4442	0.9546	0.5659
1.8	0.9638	−0.0764	0.9493	0.5822	0.9338	0.7431
2.2	0.9488	−0.0863	0.9340	0.7254	0.9155	0.9273
2.6	0.9330	−0.0928	0.9215	0.8726	0.9018	1.1163
3.4	0.8987	−0.0961	0.9078	1.1716	0.8915	1.4985
4.2	0.8758	−0.0892	0.9052	1.4661	0.8959	1.8684
5.0	0.8572	−0.0765	0.9035	1.7523	0.8980	2.2249

(IV) Calculation and Results

The aerodynamic coefficients obtained in the previous section have all been expressed in terms of the functions $T_n(k, M)$. A recurrence formula may be obtained for T_n by integrating Eq. (42) by parts. This formula was first given by Borbely;[4] however, the RTP Translation of the paper by Borbely is in error. The correct formula is

$$\nu T_n = 2^n\left[jJ_0(2k) - \frac{1}{M}J_1(2k) + \frac{(1-n)J_0(2k)}{2kM}\right]\times$$

$$e^{-2jkM} + j(1-2n)T_{n-1} + \frac{(1-n)^2}{kM}T_{n-2} \quad (59)$$

where J_0 and J_1 are Bessel functions of the first kind of zero and first order, respectively. With this formula it is possible to express all of the results for the delta wing in terms of the single function T_0. Schwarz has tabulated the values of two functions, $J_s(\lambda, x)$ and $J_c(\lambda, x)$, which are related to T_0 by the equation

$$T_0(k, M) = \frac{1}{kM}\left[J_c\left(\frac{1}{M}, 2kM\right) - jJ_s\left(\frac{1}{M}, 2kM\right)\right] \quad (60)$$

The coefficients of the previous section have been evaluated by means of Eqs. (59) and (60) for two values of Mach Number, 1.25 and 2. These results are presented in Tables 1 and 2 and are plotted as polar diagrams in Figs. 4 to 10.

In Fig. 7, at $M = 1.25$, the phase angle of $(C_M/C_{M_0})_b$ is negative for small values of the reduced frequency. Since the damping in pitch is proportional to $2 - 3\mu$ times the sine of the phase angle, the pitching motion is unstable in this range.

It is of interest to determine the Mach Number at which the pitching oscillations first become unstable for small values of frequency. This may be done by obtaining a Taylor expansion of the T_n. Thus, neglecting terms of order k^2,

$$T_n = [2^{n+1}/(n+1)] - j[2^{n+2}/(n+2)]kM \quad (61)$$

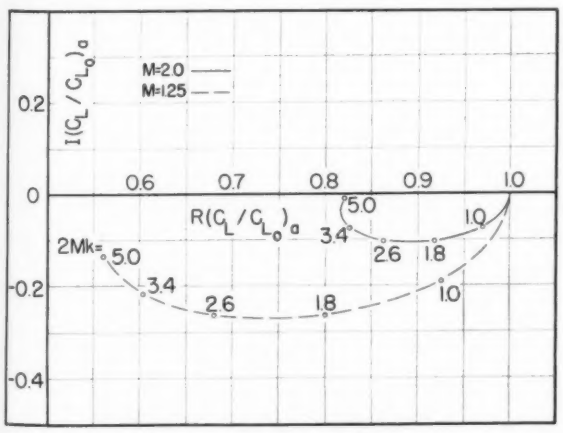

FIG. 4. Lift coefficient, Case a.

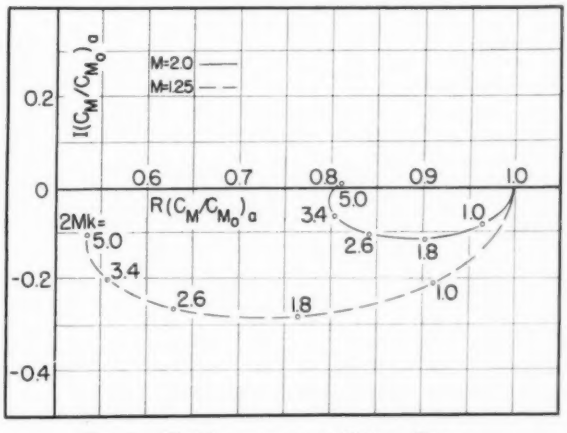

FIG. 5. Pitching moment coefficient, Case a.

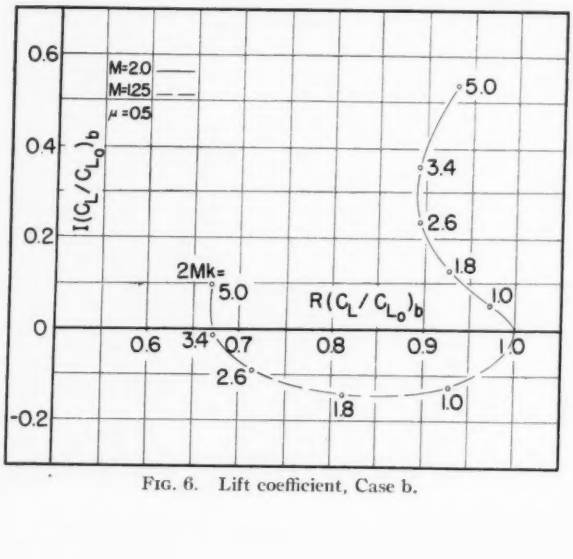

FIG. 6. Lift coefficient, Case b.

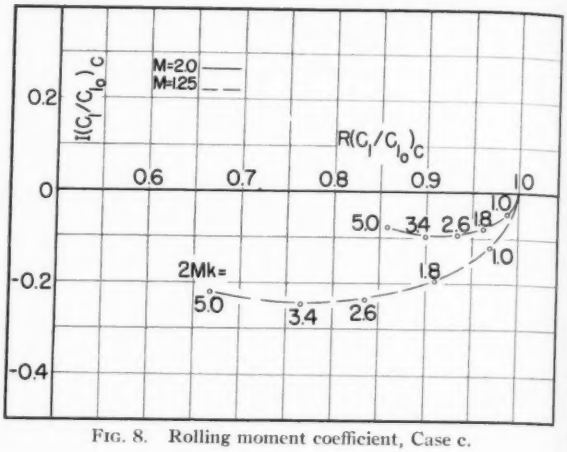

FIG. 8. Rolling moment coefficient, Case c.

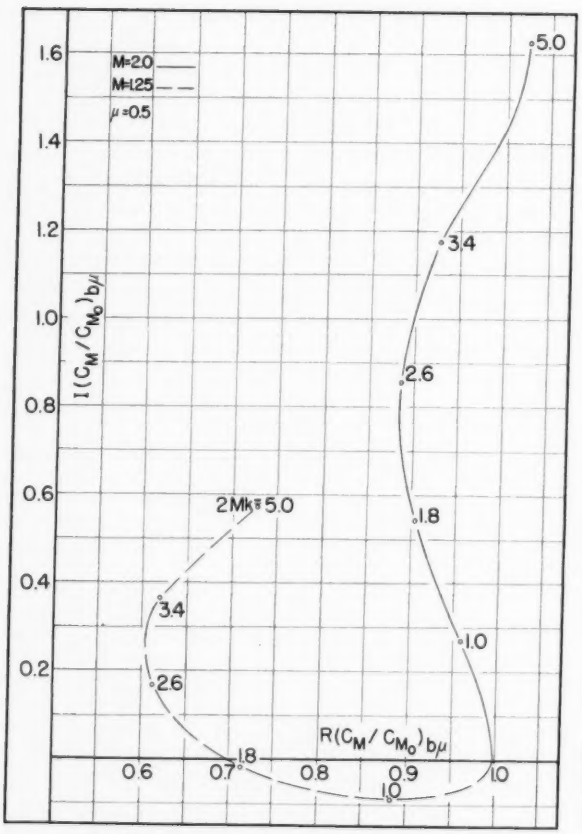

FIG. 7. Pitching moment coefficient, Case b.

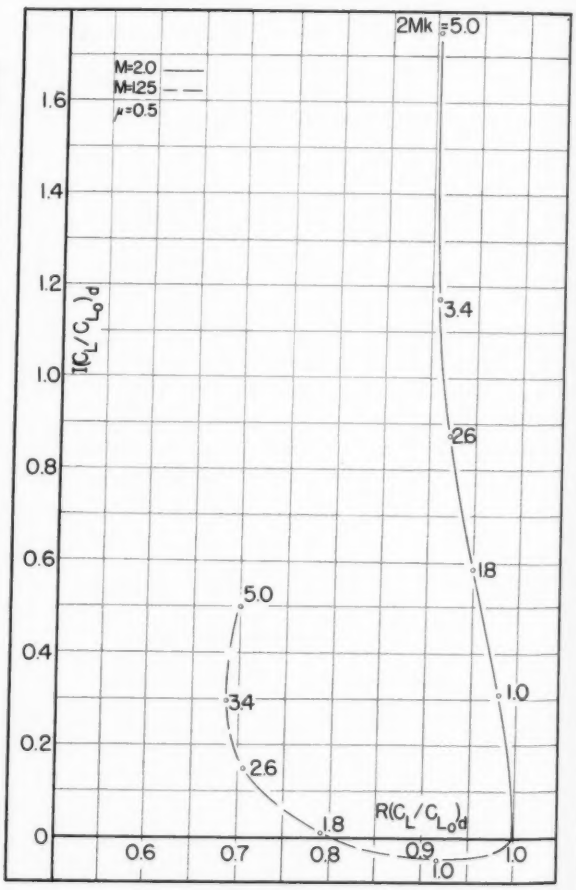

FIG. 9. Lift coefficient, Case d.

By means of Eq. (61), the expression for $(C_M/C_{M_0})_{b\mu}$ becomes, for small values of frequency,

$$\left(\frac{C_M}{C_{M_0}}\right)_{b\mu} = 1 + \frac{jk}{M(3\mu - 2)} \times \left(8\beta^2\mu - 6\beta^2\mu^2 - 3\beta^2 + \frac{3}{2} - 2\mu\right) \quad (62)$$

The condition that the damping is positive is

$$8\beta^2\mu - 6\beta^2\mu^2 - 3\beta^2 + (3/2) - 2\mu < 0$$

In Fig. 11 the Mach Number at which the damping reverses sign is plotted as a function of μ. A similar region of instability was found in the two-dimensional case calculated by Garrick and Rubinow.[6] Fig. 11 shows that the maximum Mach Number for instability is $\sqrt{2}$ and that all instability vanishes for rotations about axes aft of the three quarters chord. These results agree with those obtained by Miles.[8]

Fig. 10 indicates that the damping in the case of the flap also becomes negative at $M = 1.25$. By using Eq. (61), the expression for $(C_M/C_{M_0})_d$ becomes

$$\left(\frac{C_M}{C_{M_0}}\right)_d = 1 + \frac{jk'}{(2+\mu)M}\left[\mu\left(M^2 - \frac{7}{2}\right) + 3M^2 - \frac{9}{2}\right] \quad (63)$$

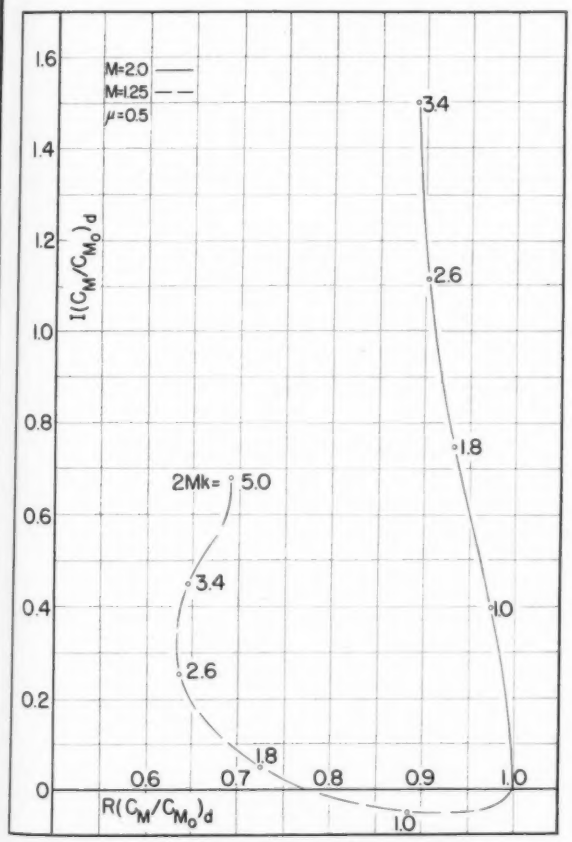

FIG. 10. Pitching moment coefficient, Case d.

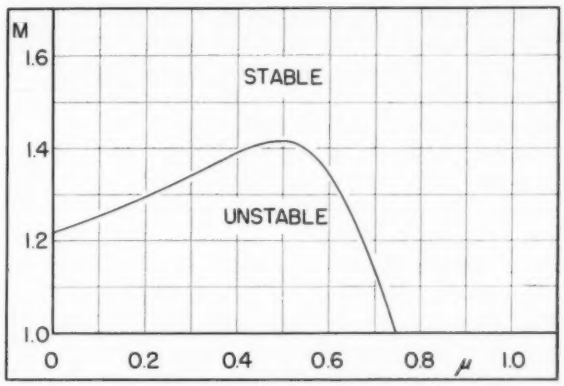

FIG. 11. Stability regions for pitching oscillation.

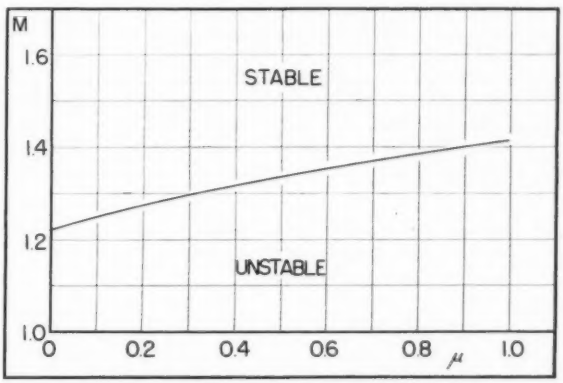

FIG. 12. Stability regions for oscillating flap.

Thus, the condition for positive damping is

$$\mu[M^2 - (7/2)] + 3M^2 - (9/2) > 0$$

The Mach Number for zero damping is plotted as a function of μ in Fig. 12. It is seen that, for a flap of infinite aspect ratio ($\mu = 1$), the Mach Number for zero damping is $\sqrt{2}$. This is the two-dimensional result obtained by Garrick and Rubinow.

(V) CONCLUSIONS

Using the linearized equations for a compressible isentropic flow, one can reduce any three-dimensional wing problem to an equivalent two-dimensional problem, provided that the edges of the wing are supersonic and that the trailing edge is normal to the flow. For the usual types of plan forms and downwash distributions, the forces acting on the wing can be expressed in terms of tabulated functions.

As an example, the forces acting on a delta wing have been calculated for the case in which the downwash exhibits a harmonic time dependence. All of the aerodynamic coefficients were found to be independent of the sweep angle. Since any nonstationary motion of a rigid delta wing can be obtained by harmonic analysis from the three modes of oscillation considered here, it is proved that the force coefficients for such an

arbitrary motion are independent of the sweep angle. It is also found that the pitching oscillations of a delta wing exhibit a characteristic instability for small values of the frequency. This is in agreement with the two-dimensional result obtained previously.

Finally, it should be noted that, while it is correct to calculate the total loads acting on the wing by strip theory, this procedure does not necessarily give the correct spanwise loading.* It is interesting, however, that, although the load distribution is disturbed by the three-dimensional effect, the two-dimensional lift of a chordwise strip is preserved. This result is in accord with the theorem on the preservation of lift for steadily lifting wings given by Dr. P. A. Lagerstrom.[11]

References

[1] Glauert, H., *The Force and Moment on an Oscillating Aerofoil*, R. and M. 1242, 1929.

[2] von Kármán, Th., and Sears, W. R., *Airfoil Theory for Non-Uniform Motion*, Journal of the Aeronautical Sciences, Vol. 5, No. 10, August, 1938.

[3] Possio, Camillo, *L'azione aerodinamica sul profile oscillante alle velocita ultrasonore*, Acto Pontif. Acad. Sci., No. 11, p. 93, 1937.

[4] Borbely, S. V., *Aerodynamic Forces on a Harmonically Oscillating Wing at Supersonic Velocity (2-Dim. Case)*, Z.A.M.M., Vol. 22, No. 4, pp. 130–205, August, 1942 (RTP Translation No. 2019).

[5] Schwarz, L., *Untersuchung einiger mit der Zylinderfunktionen nullter Ordnung verwandten Funktionen*, Luftfahrtforschung, Vol. 19, pp. 341–372, 1942.

[6] Garrick, I. E., and Rubinow, S. I., *Flutter and Oscillating Air-Force Calculations for an Airfoil in a Two-Dimensional Supersonic Flow*, N.A.C.A. T.N. No. 1158, October, 1946.

[7] Miles, John W., *The Aerodynamic Forces on an Oscillating Airfoil at Supersonic Speeds*, Journal of the Aeronautical Sciences, Vol. 14, No. 6, pp. 351–358, June, 1947.

[8] Miles, John W., *On Damping in Pitch for Delta Wings*, Journal of the Aeronautical Sciences, Vol. 16, No. 9, pp. 574–575, September, 1949.

[9] Stewart, H. J., and Li, Ting-Yi, *Periodic Motions of a Rectangular Wing Moving at Supersonic Speed*, Journal of the Aeronautical Sciences, Vol. 17, No. 9, pp. 529–539, 564, September, 1950.

[10] Miles, John W., *On Nonsteady Motion of Delta Wings*, Readers' Forum, Journal of the Aeronautical Sciences, Vol. 16, No. 9, pp. 568–569, September, 1949.

[11] Lagerstrom, P. A., and Van Dyke, M. D., *General Considerations About Planar and Non-Planar Lifting Systems*, Douglas Aircraft Corporation Report No. SM-13432, June, 1949.

[12] Miles, John W., *On Harmonic Motion of Wide Delta Airfoils at Supersonic Speeds*, Technical Memorandum RRB-36, U.S. Naval Ordnance Test Station, Inyokern, Calif., 9 February, 1950.

* This comment should be noted in connection with a similar remark on page 12 of reference 12.

Symposium on Fluid Dynamics

The Fourth Symposium on Applied Mathematics of the American Mathematical Society (cosponsored by the University of Maryland and the U.S. Naval Ordnance Laboratory) will be held at the University of Maryland, College Park, Md., and the U.S.N.O.L., White Oak, Md., on Friday and Saturday, June 22–23, 1951.

The general topic of the Symposium is "Fluid Dynamics," and sessions are planned on Turbulence, Foundations, Compressible and Incompressible Flow.

I.A.S. members interested in attending may secure additional information by writing to M. H. Martin, University of Maryland, College Park, Md.

Effects of Pressure Gradient on Stability and Skin Friction in Laminar Boundary Layers in Compressible Fluids†

HERSCHEL WEIL‡
General Electric Company

ABSTRACT

An extension of the von Kármán-Pohlhausen method is carried through to find approximate steady-state velocities and temperatures in the compressible laminar boundary layer with a pressure gradient in the direction of flow along a two-dimensional adiabatic wall. These are used to find the effect of pressure gradient on skin friction; on momentum thickness; and, by a criterion due to Lees, on stability to small perturbations.

At a given point along the airfoil, the boundary layer is stable if the Reynolds number R_θ based on momentum thickness is less than a certain critical value $(R_\theta)_{cr.\ min.}$ which is a function solely of Mach Number M and a suitable parameter λ dependent on the airfoil shape. A curve family of $(R_\theta)_{cr.\ min.}$ vs. λ for various M's is given. In addition, the product of skin friction times R_θ, which depends solely on λ, is plotted. Numerical results were obtained for flows at $M = 1.5$ and 4 over a 5 per cent thick biconvex airfoil which showed that for these examples the favorable effect of the negative pressure gradient on stability is not large for $M = 4$ but is extremely pronounced at the lower supersonic Mach Number $M = 1.5$, and in both cases there is an increase in drag up to about 30 per cent at mid-chord compared to the case of a flat plate. The dependence on M and λ of the conversion factors between Reynolds Numbers based, respectively, on distance from the leading edge x, on momentum thickness θ, and on displacement thickness δ^* is exhibited.

NOTATION

C_f	= local skin-friction coefficient
c_p	= specific heat at constant pressure
i	= enthalpy
k	= [see Eq. (29)]
K	= [see Eq. (10)]
L	= a typical length, such as chord length
M	= Mach Number
n	= distance measured normal to airfoil boundary
p	= pressure
$\bar{p}$	= p/p_∞
P_r	= Prandtl Number
R	= universal gas constant or Reynolds Number
R_x, R_{δ^*}, R_θ	= Reynolds Numbers defined, respectively, with x, δ^*, and θ as typical length, $u_1 x/\nu_1$, etc.
s	= distance measured along airfoil boundary from the leading edge
t	= [see Eq. (11)]
T	= temperature, absolute, $(\bar{T} = T/T_1)$
u	= velocity in s direction (tangential)
v	= velocity in n direction (normal)
w	= u/u_1
x	= distance measured along airfoil chord from the leading edge
γ	= ratio of specific heat at constant pressure to specific heat at constant volume
δ	= boundary-layer thickness
δ^*	= boundary-layer displacement thickness
η	= n/δ
θ	= boundary-layer momentum thickness
κ	= [see Eq. (32)]
λ	= [see Eq. (16)]
μ	= viscosity
ρ	= density
ν	= μ/ρ

A superscribed bar denotes a dimensionless ratio as given by Eq. (2).

Subscripts

$()_0$	= stagnation value
$()_1$	= "local ambient" value—i.e., the value taken just outside the boundary layer at the s value in question
$()_\infty$	= undisturbed free-stream quantity
$()_{cr.\ min.}$	= critical minimum
$()_w$	= value taken at the solid boundary
$()_{tr}$	= transition

(I) INTRODUCTION

IN ORDER TO INVESTIGATE both skin friction and the stability to time dependent perturbations of a laminar boundary layer in compressible flow, it is necessary to obtain the steady-state velocity and temperature distributions in the boundary layer. An extension of the von Kármán-Pohlhausen method of incompressible flow†† is given here to find these steady-state distributions with sufficient accuracy for stability computations for flows over insulated bodies with a generally nonvanishing pressure gradient in the direction of flow. It is assumed that the Prandtl Number is unity and that viscosity is proportional to temperature. The velocity and temperature distributions obtained in this way are then applied to studying the stability of laminar boundary layers by the methods of Lees and Lin[1] and to finding skin friction.

In connection with stability, the formulas are given for the computation of a particular Reynolds Number,

Received July 7, 1950.

† The author wishes to thank the U.S. Army Ordnance Department and the General Electric Company for permission to publish these results and R. H. Norris and Dr. Carl Gazley, of the General Electric Company, for helpful discussions. In particular, Eq. (36) was pointed out by Dr. Gazley.

‡ Mathematician, General Engineering and Consulting Laboratory.

†† This extension is closely related to the work of Dorodnitzyn[8] and Howarth[7] as explained in Section (III) of this paper.

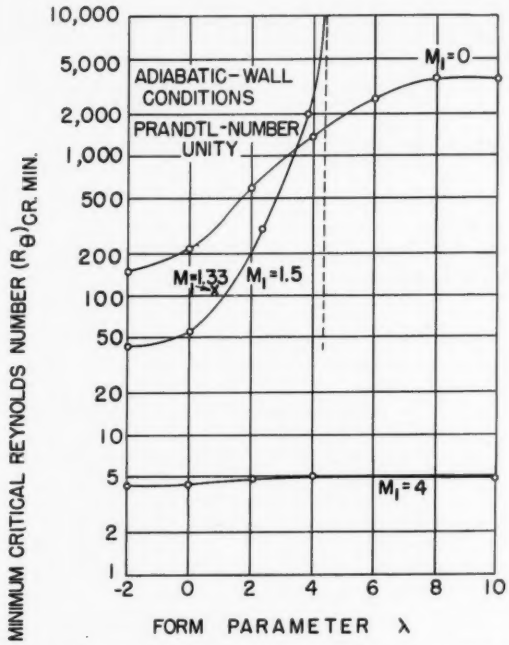

FIG. 1. Minimum critical Reynolds Number for stability, as a function of form parameter.

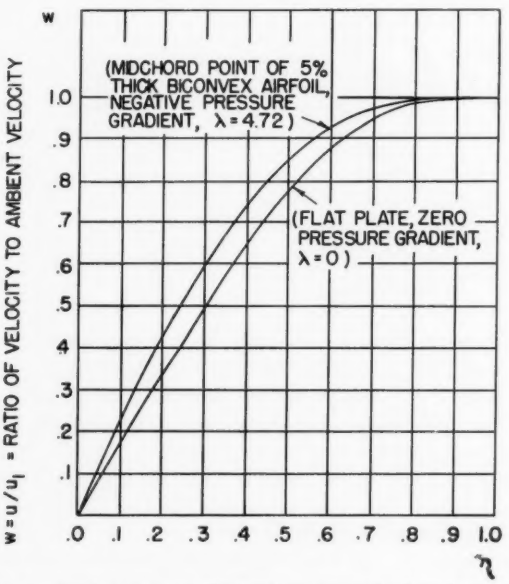

FIG. 2. Typical velocity distributions across the boundary layer to illustrate effect of pressure gradient, $M = 1.5$.

$(R_\theta)_{cr.\ min.}$, by Lees'[2] rapid approximate method when the steady-state distributions are given in a special coordinate system that is used here. The significance of $(R_\theta)_{cr.\ min.}$ lies in the fact that, in laminar boundary layers at points where the Reynolds Number $R_\theta < (R_\theta)_{cr.\ min.}$, small time-dependent disturbances originating in the layer will be damped out; the boundary layer will be stable, whereas at points where $R_\theta > (R_\theta)_{cr.\ min.}$ these disturbances may build up and cause the boundary-layer flow to become turbulent.

The quantity $(R_\theta)_{cr.\ min.}$ computed with the type of velocity distributions considered here depends solely on the local ambient† Mach Number and a quantity λ, called the form parameter. For a given local ambient Mach Number, λ is proportional both to the local ambient velocity gradient in the direction of the undisturbed flow and to the square of the boundary-layer thickness at the point in question. Thus, the information on the dependence of stability on velocity gradient or pressure gradient may be essentially contained in a family of curves of $(R_\theta)_{cr.\ min.}$ vs. λ for various values of M. However, for practical purposes, the quantity $(R_x)_{cr.\ min.}$ is of greater importance than $(R_\theta)_{cr.\ min.}$, since it is $(R_x)_{cr.\ min.}$ that determines how far behind the leading edge the boundary layer is stable—namely, from the leading edge to the point where R_x becomes equal to $(R_x)_{cr.\ min.}$. Thus, one is also interested in the effect of pressure gradient on the conversion factor $k = R_x/R_\theta^2$. Unfortunately, k does not depend explicitly on M and λ only but also depends explicitly on position, $\bar{x}$, along the airfoil and the local ambient velocity gradient. Thus, universal curve families of these quantities are not possible as with $(R_\theta)_{cr.\ min.}$. The situation is different from the flat plate case where, within the approximations used here, k is independent of M and x. Similar remarks hold for the quantities $C_f\sqrt{u_1 s/\nu_1}$ and $\theta\sqrt{u_1/\nu_1 s}$ related, respectively, to skin friction coefficient and momentum thickness, since these are shown to be respectively proportional to $\sqrt{k}$ and equal to $1/\sqrt{k}$. The quantity $C_f R_\theta$, however, depends solely on λ.

For high-speed flights of noninsulated bodies, where heat is conducted from the air to the solid body, $(R_\theta)_{cr.\ min.}$ is actually larger than would be predicted for the insulated bodies considered here. The boundary layers in this case are consequently more stable, so that the values of $(R_\theta)_{cr.\ min.}$ computed by the methods given here may be looked on, in a sense, as worst possible values. The increase of $(R_\theta)_{cr.\ min.}$ with decrease of surface temperature is actually a pronounced effect. In fact, from the data in Fig. 6b of reference 2 for flow over a flat plate at Mach Number 0.7 with no pressure gradient, $(R_x)_{cr.\ min.}$ increases from 3.8×10^4 to 1.8×10^6 as the wall temperature decreases from that of an insulated wall, T_{aw}, to $0.77\ T_{aw}$.

At supersonic speeds, this effect is even more pronounced, since, at certain critical temperatures somewhat lower than adiabatic wall temperature, complete stability $[(R_x)_{cr.\ min.} = \infty]$ is achieved over a flat plate, $M > 3$. For example, at $M = 4$, this critical temperature is computed in reference 2 to be $0.86\ T_{aw}$.

† The term "local ambient" is used throughout this report to refer to values just outside the boundary layer at an arbitrary distance, x, from the leading edge.

TABLE 1

Configuration	$\bar{s}$	M_1	$d\bar{p}/d\bar{s}$	λ	k	$(R_\theta)_{cr.\ min.}$	$(R_x)_{cr.\ min.}$
5 per cent biconvex airfoil	0.0789	1.33	−0.687	0.810	2.48	107	28,400
	0.500	1.5	−0.562	4.72	2.75	Complete stability	
Flat plate	...	1.5	0	0	2.29	55.0	6,930

(II) Results and Conclusions

(A) *Stability*

Curves were computed of $(R_\theta)_{cr.\ min.}$ vs. λ at Mach Numbers 0, 1.5, and 4 and are shown in Fig. 1. The curve for $M = 0$ was computed from the data in Fig. 2 of reference 3 by using Eq. (32) of this report, while the other two curves were computed by the methods of Section (IV).† For $M = 1.5$, the favorable effect of negative pressure gradient is pronounced, $(R_\theta)_{cr.\ min.}$ becoming infinite at $\lambda = 4.38$. However, for $M = 4$, the favorable effect of negative pressure gradient is insignificant.

It is evident from Fig. 1 that, in the supersonic range, for a fixed λ, this favorable effect of negative pressure gradients becomes much less as the Mach Number increases—that is, the ratio

$$(R_\theta)_{cr.\ min.}(\lambda, M)/(R_\theta)_{cr.\ min.}(0, M)$$

for a fixed positive λ decreases as M increases.

Computations were carried out to find the local ambient values of Mach Number and of λ along the forward half of a two-dimensional biconvex airfoil of 5 per cent thickness-to-chord ratio and undisturbed free-stream Mach Number 1.5. The λ values are given by the curve labeled "integral curve" in Fig. 5. At a point 7.58 per cent of the chord length from the leading edge, the local ambient Mach Number is 1.33, $\lambda = 0.810$, and the value $(R_\theta)_{cr.\ min.}$ is 107, lying somewhat above the corresponding point on the $M = 1.5$ curve of Fig. 1. At the mid-chord point $M = 1.5$, $\lambda = 4$, and there is complete stability. These results are included in Table 1. This shows that, near the leading edge, pressure gradient is not sufficiently negative to bring an important increase of $(R_\theta)_{cr.\ min.}$ over the value for a flat plate, but it is evident that the extremely strong favorable effect of a sufficiently increased λ is brought into play as one nears the mid-chord point.

Table 1 contains, in addition to the values of λ and $(R_\theta)_{cr.\ min.}$ mentioned above for the airfoil, the corresponding values of $k = R_x/R_\theta^2$ and $(R_x)_{cr.\ min.}$ and also the values applicable for a flat plate at $M_\infty = 1.5$. The k values were computed by Eq. (29).

Bear in mind that these results are for an insulated (adiabatic) wall and that, at slightly lower wall temperatures than that of an adiabatic wall, finite $R_{cr.\ min.}$ may increase radically as discussed in Section (I).

In addition, it should be pointed out that a difference is to be expected between $R_{cr.\ min.}$, the Reynolds Number at which instability may occur, and R_{tr}, the Reynolds Number at which the originally laminar boundary layer may actually become turbulent. At present, there is no theory to determine R_{tr}, although R_{tr} has been found in a few cases by experiments where sufficiently low free-stream turbulence was obtained so that transition due to disturbances originating in the boundary layer could be observed.[4–6] These experiments indicate that, for adiabatic conditions, $(R_x)_{tr}$ is never less than about 10^6. Comparison with the $(R_x)_{cr.\ min.}$ values corresponding to the curves of Fig. 1 shows that the magnitude of the difference $R_{cr.\ min.} - R_{tr}$ is far greater than the increase of $R_{cr.\ min.}$ with favorable pressure gradient for a sufficiently high Mach Number such as $M = 4$. This indicates that the pressure gradient effect on $R_{cr.\ min.}$ is relatively unimportant at extremely high speeds and can safely be neglected.

Incidental to the stability computations, it was necessary to compute the data needed for curves of w vs. η—that is, velocity divided by local ambient velocity vs. distance normal to the airfoil divided by the local boundary-layer thickness. Two of these curves are shown in Fig. 2—one for flow over a flat plate and the other for flow at the mid-chord point of a 5 per cent airfoil, both for $M = 1.5$.

(B) *Friction Drag*

The formulas of Section (III C) show how to compute not only k but the closely related quantities, momentum thickness and skin friction. The numerical computations showed an increase in local skin-friction coefficient as compared to the case of a flat plate at the same free-stream Mach Number. This increase reached about 30 per cent at the mid-chord point for $M_\infty = 1.5$ as the results in Table 2 indicate.

In addition, $C_f R_\theta$, which depends solely on λ (Eq. 50), is shown graphically as a function of λ in Fig. 3.

TABLE 2

Configuration	M_1	$\bar{s}$	$\theta\sqrt{u_1/\nu_1 x} = 1/k$	$C_f\sqrt{u_1 x/\nu_1}$
5 per cent biconvex airfoil	1.33	0.0789	0.635	0.736
	1.5	0.500	0.604	0.975
	3.68	0.0789	0.654	0.704
	4	0.500	0.683	0.883
Flat plate	0 to ∞	0 to 1	0.661	0.661

† The author is indebted to Prof. Lester Lees, of Princeton University, for pointing out to him that in reference 9, on which this paper is based, the stability curves for $M = 1.5$ and 1.4 were computed incorrectly. This came about because a factor π was omitted from the equation in that report corresponding to Eq. (40) in this paper and on which these curves are based.

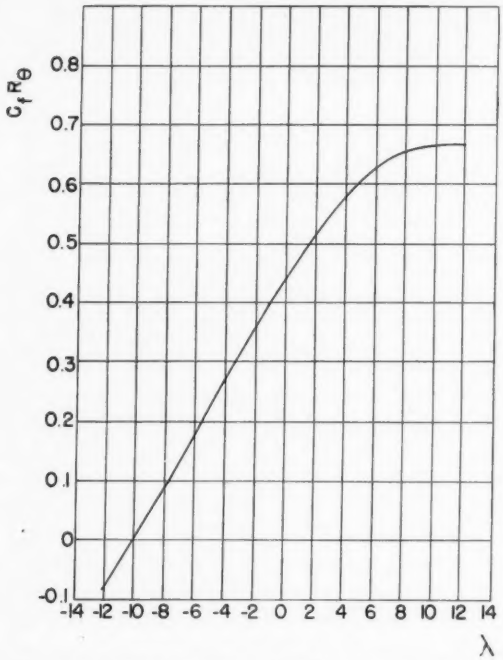

FIG. 3. Skin-friction coefficient times Reynolds Number based on momentum thickness plotted vs. form parameter.

Principally as a check on the methods used here, it was decided to verify some numerical results obtained by Howarth[7] by a procedure not related to the von Kármán-Pohlhausen method for a flow given by $\bar{u}_1 = \beta\bar{x}$. This is actually the type of flow one gets near the forward stagnation point on a blunt-nosed body. Fig. 6 of reference 7 is, in the present notation, a curve of

$$\frac{1}{2} C_f \sqrt{R_x}(1 - \beta^2\bar{x}^2)^{1/4} \text{ vs. } M_1/\sqrt{1 + \frac{\gamma - 1}{2} M_1^2}$$

It is reproduced in Fig. 4 for the abscissa range 0 to 0.6 ($1 \leq M_1 \leq 0.67$), together with the corresponding curve computed by the procedures of Section (III) but using fourth-order polynomials.

(III) Theoretical Basis for the Steady-State Flow Computations

(A) *General Discussion*

The method used here to determine the steady-state velocity distribution in the boundary layer is an extension to compressible flow of the von Kármán-Pohlhausen method used in incompressible flow problems. This method consists of assuming that the velocity u in the integrated momentum equation is a suitable polynomial in the perpendicular distance n from the solid body. The polynomial involves an undetermined parameter, $\lambda(s)$ occurring linearly in the coefficients. By this procedure the integrated momentum equation is reduced to a first-order ordinary differential equation for λ which may then be integrated under a suitable boundary condition.

It will be shown in Sections (III B) and (III C) that the extension to compressible flow is made feasible by assuming $P_r = K = 1$ and by introducing a certain change from $\bar{n}$ to a new variable τ. This transformation, Eqs. (11) and (12), was introduced by Dorodnitzyn[8] simultaneously with an additional but nonessential transformation in the s direction which is actually a hindrance for numerical application of the theory. Later, Howarth[7] applied a transformation in the normal direction only, as in this report, his new coordinate being a function of s times the t of this report. His reference quantities are not the same as the ones used here, and his λ is defined in a slightly different way. Since Howarth used only a transformation in the normal direction, there is no basic reason to prefer the transformation used here to his transformation, and his λ and differential equation for λ would serve as well. However, the work reported here was largely completed before reference 7 came to the writer's attention.

Both these authors considered fourth-order polynomial approximations for u which permit the boundary conditions on u and its first two derivatives with respect to n to be satisfied. However, for the stability problem, the second derivatives of u with respect to n are extremely important, and, in order to obtain these with some accuracy, a sixth-order polynomial is necessary. One can then impose, on the third derivative of u, the proper boundary conditions at the wall and at the outer edge of the boundary layer so that at least the correct rate of change of the second derivative can be ensured near these boundaries. It turns out that the transformation (11) is essential not only in obtaining the ordinary differential equation for λ but also to enable one to satisfy the boundary condition on the third derivative at the solid boundary.

In the following, the derivation of the differential equation for λ is different from the equation in reference 7 or 8, where the transformations are applied to the nonintegrated momentum equation expressed in terms of a stream function, and thereby it is attempted

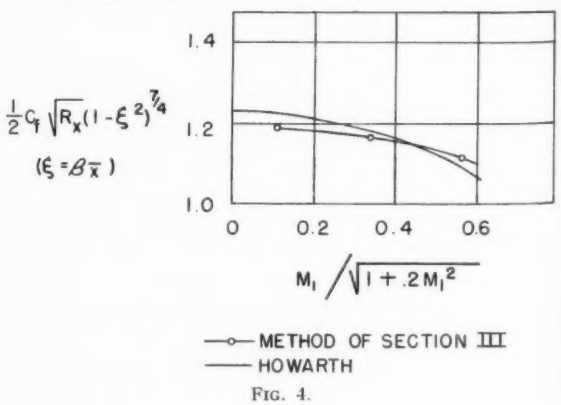

FIG. 4.

to make the reason for the change from n to τ more evident than it is in these references.

(B) *Transformation of the Integrated Momentum Equation to an Equation for* λ

The well-known momentum equation in boundary-layer flow is

$$\rho\left(u\frac{\partial u}{\partial s}+v\frac{\partial u}{\partial n}\right)=-\frac{\partial p}{\partial s}+\frac{\partial}{\partial n}\left(\mu\frac{\partial u}{\partial n}\right) \tag{1}$$

In terms of the dimensionless variables

$$\bar{u}=\frac{u}{\sqrt{2i_0}},\quad \bar{s}=\frac{s}{L},\quad \bar{n}=\frac{n}{L},\quad \bar{\delta}=\frac{\delta}{L} \tag{2}$$

Eq. (1) may be integrated for compressible flow to

$$\left(\frac{\mu}{\rho_0\sqrt{2i_0}L}\frac{\partial\bar{u}}{\partial\bar{n}}\right)_{\bar{n}=0}=\frac{\partial}{\partial\bar{s}}\int_0^{\bar{\delta}}\frac{\rho}{\rho_0}\bar{u}\,(\bar{u}_1-\bar{u})\,d\bar{n}+\frac{\partial\bar{u}_1}{\partial\bar{s}}\int_0^{\delta}\left(\frac{\rho_1}{\rho_0}\bar{u}_1-\frac{\rho}{\rho_0}\bar{u}\right)d\bar{n} \tag{3}$$†

where the integration is carried out at a fixed $\bar{s}$. In the incompressible case, ρ is constant so that, when a particular form of $\bar{u}$ such as a polynomial is assumed, the integrals may be immediately evaluated. Here, however, the variable ρ appears under the integral sign, and one must know the behavior of ρ as a function of $\bar{n}$.

The assumption of $P_r = 1$ takes care of this, for then one can show that

$$\frac{\rho}{\rho_0}=(1-\bar{u}_1^2)^{\gamma/(\gamma-1)}/(1-\bar{u}^2) \tag{4}$$

This is a consequence of the fact that, with $P_r = 1$, the momentum equation [Eq. (1)] and the equation of conservation of energy in the boundary layer[10]

$$\rho c_p\left(u\frac{\partial T}{\partial s}+v\frac{\partial T}{\partial n}\right)=u\frac{\partial p}{\partial s}+\mu\left(\frac{\partial u}{\partial n}\right)^2+\frac{\partial}{\partial n}\left(k\frac{\partial T}{\partial n}\right) \tag{5}$$

may be combined to yield

$$\rho\left(u\frac{\partial}{\partial s}+v\frac{\partial}{\partial n}\right)\left(c_pT+\frac{u^2}{2}\right)=\frac{\partial}{\partial s}\left[\mu\frac{\partial}{\partial n}\left(c_pT+\frac{u^2}{2}\right)\right] \tag{6}$$

An integral of this corresponding to an adiabatic wall [for which $(\partial T/\partial n)_{n=0} = 0$] is $c_pT + (u^2/2) = i_0 =$ constant, which may be rewritten in the following form:

$$T=T_0\,(1-\bar{u}^2) \tag{7}$$

When this is combined with the equation of state

$$p=\rho RT \tag{8}$$

and Bernoulli's equation, written in the form

$$p=p_0(1-\bar{u}_1^2)^{\gamma/(\gamma-1)} \tag{9}$$

† See reference 9 for details of this.

Eq. (4) follows. Eq. (9) makes use of the assumption of perfect gases, p = constant ρ^γ.

In addition, one can assume that

$$\mu=\mu_0\,(1-\bar{u}^2)^K \tag{10}$$

where K is a numerical exponent that will later be specialized to $K = 1$.

Now, however, if Eq. (4) is substituted in Eq. (3) and fourth- or sixth-order polynomials in $\bar{n}$ are assumed for $\bar{u}$, the integrals cannot be readily evaluated as they would be in Eq. (3) with ρ = constant because there will be terms with factors $(1-\bar{u}^2)^{-1}$ in the integrals. This suggests the introduction of the new variable

$$t=\int_0^{\bar{n}}\frac{\rho}{\rho_0}\,d\bar{n}=\int_0^{\bar{n}}\frac{(1-\bar{u}_1^2)^{\gamma/(\gamma-1)}}{1-\bar{u}^2}\,d\bar{n} \tag{11}$$

In addition, one can make the range of integration independent of $\bar{s}$ by using, instead of t,

$$\tau=t/t(\bar{\delta}) \tag{12}$$

Eq. (3) takes the form

$$\frac{1}{2}\frac{d\,[t(\bar{\delta})]^2}{d\bar{s}}\left(\int_0^1\bar{u}^2\,d\tau-\bar{u}_1\int_0^1\bar{u}\,d\tau\right)+[t(\bar{\delta})]^2\times\left[\frac{d}{d\bar{s}}\int_0^1\bar{u}^2\,d\tau-\bar{u}_1\frac{d}{d\bar{s}}\int_0^1\bar{u}\,d\tau-\frac{\bar{u}_1}{1-\bar{u}_1^2}\frac{d\bar{u}_1}{d\bar{s}}\times\int_0^1(1-\bar{u}^2)\,d\tau\right]+\frac{(1-\bar{u}_1^2)^{\gamma/(\gamma-1)}\nu_0}{\sqrt{2i_0}\,L}\left.\frac{d\bar{u}}{d\tau}\right|_{\tau=0}=0 \tag{13}$$

from which it is evident that, when $\bar{u}$ is a polynomial in τ, the integrals may be readily evaluated.

The conditions that the velocity $\bar{u}$ must satisfy are, first of all,

$$\bar{u}(1)=\bar{u}_1,\quad \left.\frac{\partial\bar{u}}{\partial\tau}\right|_{\tau=1}=\left.\frac{\partial^2\bar{u}}{\partial\tau^2}\right|_{\tau=1}=\left.\frac{\partial^3\bar{u}}{\partial\tau^3}\right|_{\tau=1}=0 \tag{14}$$

on the usual assumption of a flow outside the boundary layer which is independent of y. Because the fluid does not slip along the solid boundary,

$$\bar{u}(0)=0 \tag{15}$$

Two more boundary conditions may be determined at $\tau = 0$ by considering the limit as $y \to 0$ of the momentum equation and also the limit of its y derivative. These two limits give, respectively, the conditions

$$\left.\begin{aligned}(\partial^2\bar{u}/\partial\tau^2)|_{\tau=0}&=-\bar{u}_1\lambda\\ \lambda&=\left\{\frac{[t(\bar{\delta})]^2L\sqrt{2i_0}}{\nu_0(1-\bar{u}_1^2)^{(2\gamma-1)/(\gamma-1)}}\right\}\frac{d\bar{u}_1}{d\bar{s}}=\\ &\quad\left\{\frac{-[t(\delta)]^2\,p_0L}{\mu_0u_1(1-u_1^2)^{2\gamma/(\gamma-1)}}\right\}\frac{d\bar{p}}{d\bar{s}}\end{aligned}\right\} \tag{16}$$

and

$$(\partial^3\bar{u}/d\tau^3)|_{\tau=0}=2(K-1)\,(\partial\bar{u}_1/\partial\tau)^3|_{\tau=0} \tag{17}$$

One can check that near a stagnation point these boundary conditions reduce to those in the incompressible

case. Eqs. (14) to (17) form a set of equations which determines the coefficients of the polynomial $\bar{u}(\tau)$. However, Eq. (17) makes the set nonlinear and therefore not readily solved unless $K = 1$, which is the reason for making this assumption. When it is made, the set of conditions on $\bar{u}$ and, consequently, the polynomial for τ take the same form as found by Schlichting and Ulrich[11] in the incompressible case.

$$\bar{u} = \bar{u}_1 [f(\tau) + \lambda g(\tau)] \tag{18}$$

where

$$\left.\begin{aligned} f &= 2\tau - 5\tau^4 + 6\tau^5 - 2\tau^6 \\ g &= \frac{1}{5}\tau - \frac{1}{2}\tau^2 + \tau^4 - \tau^5 + \frac{3}{10}\tau^6 \end{aligned}\right\} \tag{19}$$

It is interesting to note that the boundary condition corresponding to Eq. (17) expressed in terms of derivatives with respect to $\bar{n}$ is

$$(d^3\bar{u}/d\bar{n}^3)\big|_{\bar{n}=0} = 2K(d\bar{u}/d\bar{n})^3\big|_{\bar{n}=0} \tag{20}$$

Thus, if $\bar{u}$ were assumed to be a polynomial in $\bar{n}$ rather than in τ, linear equations for the polynomial coefficients would be possible only when $K = 0$, so that μ would be everywhere constant, which is less realistic than the assumption $\mu/\mu_0 = T/T_0$ made above.

With the help of the definition [Eq. (16)] of λ, Eq. (13) may now be written as an equation for λ which is to be solved subject to a proper boundary condition at some point $s = s_0$. This equation may be manipulated to the form

$$d\lambda/d\bar{s} = U_1\Lambda_1(\lambda) + U_2\Lambda_2(\lambda) \tag{21}$$

where

$$\left.\begin{aligned} U_1 &= \frac{\bar{u}_1''}{\bar{u}_1'} + \frac{2\bar{u}_1\bar{u}_1'}{1-\bar{u}_1^2}\left(2 + \frac{\gamma}{\gamma-1}\right) \\ U_2 &= (\bar{u}_1'/\bar{u}_1) + [\bar{u}_1\bar{u}_1'/(1-\bar{u}_1^2)] \end{aligned}\right\} \tag{22}$$

while the functions Λ_1 and Λ_2 are the same as in the incompressible case,

$$\left.\begin{aligned} \Lambda_1(\lambda) &= \lambda A(\lambda)/[A(\lambda) + B(\lambda)] \\ \Lambda_2(\lambda) &= \\ &\frac{-2\{\lambda C(\lambda) + 2\lambda A(\lambda) + [f' - \lambda(1-g')]_{\tau=0}\}}{A(\lambda) + B(\lambda)} \end{aligned}\right\} \tag{23}$$

where

$$\left.\begin{aligned} A(\lambda) &= \int_0^1 (f^2 + 2\lambda fg + \lambda^2 g^2 - f - \lambda g)\, d\tau \\ B(\lambda) &= 2\lambda \int_0^1 (2\lambda g^2 - g + 2fg)\, d\tau \\ C(\lambda) &= \int_0^1 (f + \lambda g)\, d\tau \end{aligned}\right\} \tag{24}$$

When the sixth-order polynomials [Eqs. (19)] are used, A, B, and C may be determined numerically, and

$$\left.\begin{aligned} \Lambda_1(\lambda) &= \frac{95\lambda^2 + 28\lambda^3}{4{,}925 - 142.5\lambda - 35\lambda^2} + \lambda \\ \Lambda_2(\lambda) &= \frac{180{,}180 - 27{,}422\lambda + 1{,}048\lambda^2 + 28\lambda^3}{4{,}925 - 142.5\lambda - 35\lambda^2} \end{aligned}\right\} \tag{25}$$

Note that U_1 and U_2 depend only on local ambient values and are actually independent of the form of function used for $\bar{u}(\tau)$, although Λ_1 and Λ_2 depend indirectly on $\bar{u}(\tau)$. As a check on Eq. (22), one can verify that, in the neighborhood of a stagnation point where $\bar{u}_1 = 0$, Eq. (21) reduces to the corresponding equation for incompressible flow.

(C) *Momentum Thickness, Skin Friction, and the Relations Between R_θ and R_x, and R_θ and R_{δ^*}*†

The simple approximate relations

$$\theta\sqrt{\frac{u_1}{\nu_1 x}} = C_f\sqrt{\frac{u_1 x}{\nu_1}} = 0.667, \quad R_x = 2.25R_\theta^2 \tag{26}$$

used, for example, in reference 2 no longer hold when the pressure gradient does not vanish. However, when $\bar{u}$ is approximated by a polynomial, as in the foregoing sections, expressions for θ and C_f, as well as the connection between R_θ and R_x, are not difficult to compute.

By the definitions of the Reynolds Numbers,

$$R_\theta = R_x(\theta/x) \tag{27}$$

while the momentum thickness θ is defined by

$$\theta = \frac{1}{\rho_1 u_1^2}\int_0^\delta \rho u(u_1 - u)\, dn \tag{28}$$

With the help of the formulas of the preceding section [with $K = 1$ in Eq. (10)], one can find, by direct substitution in Eqs. (27) and (28), that

$$\left.\begin{aligned} \theta^2\frac{u_1}{\nu_1 x} &= \frac{1}{k}, \quad R_x = kR_\theta^2 \\ k(\bar{x}, \lambda) &= \frac{\bar{x}\,\bar{u}_1'}{(1-\bar{u}_1^2)\bar{u}_1\lambda A^2(\lambda)} \end{aligned}\right\} \tag{29}$$

where A is given by Eq. (24).

In a similar manner, the displacement thickness

$$\delta^* = \frac{1}{\rho_1 u_1}\int_0^\delta (\rho_1 u_1 - \rho u)\, dn \tag{30}$$

† By generalizing the von Kármán-Pohlhausen approach for use with compressible flow in a different manner from this paper, Oswatisch and Wieghardt[12] obtain the quantity δ^*/θ as a function of

$$\lambda^* = (\rho_w\theta^2/\mu_w)(du_1/ds)$$

by a numerical method based on the use of the Hartree velocity profiles for incompressible flow. They also obtain an expression relating $d\delta^*/ds$ to δ^*/θ and the free-stream velocity distribution. This expression is applied to the study of stability in the interaction between the boundary layer and the free-stream flow, although this study is limited to the flat-plate case. References to other related German work are given in this report.

may be written as

$$\delta^* = L\ell(\bar{\delta})\left[\frac{1-\bar{u}_1^2\,(A+C)}{(1-\bar{u}_1^2)^{\gamma/(\gamma-1)}} - \frac{C}{(1-\bar{u}_1^2)^{1/(\gamma-1)}}\right] \tag{31}$$

where A and C are defined by Eq. (24). Then,

$$\kappa \equiv \frac{R_\delta^*}{R_\theta} = \frac{\delta^*}{\theta} = \frac{A\bar{u}_1^2 + C - 1}{A\,(1-\bar{u}_1^2)} \tag{32}$$

Finally, the skin-friction coefficient

$$C_f = 2\mu_0\,(\partial u/\partial n)|_{n=0}/\rho_1 u_1^2 \tag{33}$$

may be put in the form

$$C_f\sqrt{\frac{xu_1}{\nu_1}} = 2A(\lambda)\sqrt{k}\left(\frac{df}{d\tau}+\frac{dg}{d\tau}\right)_{\tau=0} \tag{34}$$

which, for the sixth-order polynomials [Eqs. (19)], becomes

$$C_f\sqrt{R_x} = 4A(\lambda)\sqrt{k}[1+(\lambda/10)] \tag{35}$$

where k is given by Eq. (29). Although $C_f\sqrt{R_x}$ depends on $\bar{x}$ through the appearance of k in Eq. (35), the quantity C_fR_θ depends only on λ. When k in Eq. (35) is replaced by R_x/R_θ^2, there results

$$C_fR_\theta = 4A(\lambda)\,[1+(\lambda/10)] \tag{36}$$

Eqs. (29) and (35) may be compared with Eq. (26) when there is no pressure gradient so that $\bar{u}_1' = \bar{u}_1'' = \lambda = 0$. In this case one has, from Eqs. (21) and (25),

$$(d/dx)\,(\lambda/\bar{u}_1') = 36.56/\bar{u}_1(1-\bar{u}_1^2) \tag{37}$$

in which the right side is a constant. Integrating this for $\lambda/\bar{u}_1'$ and substituting in Eqs. (29) and (35) yields

$$\theta\sqrt{\frac{u_1}{\nu_1 x}} = C_f\sqrt{\frac{u_1 x}{\nu_1}} = 0.667, \quad R_x = 2.29\,R_\theta^2 \tag{38}$$

(D) *Relation Between $\bar{u}$ and M*

It is convenient to be able to convert readily between $\bar{u}$ and M. These two quantities are related by

$$M_1^2 = 2\bar{u}_1^2/(\gamma-1)\,(1-\bar{u}_1^2) \tag{39}$$

which follows by substituting Eq. (7) and the perfect gas relationship

$$c_p = [\gamma/(\gamma-1)]R \tag{40}$$

into the expression

$$M_1^2 = u_1^2/\gamma RT \tag{41}$$

(E) *Computations of λ for the Airfoil*†

The results tabulated in Tables 1 and 2 for flow over a thin biconvex airfoil depend on the determination of $\lambda(s)$, the proper integral of Eq. (21). The computation of the coefficients (22) in this equation was based on an approximate formula for u derived by Tollmien,[13]

$$\bar{u}_1 = \bar{u}_\infty\,(1 + c_1\epsilon + c_2\epsilon^2) \tag{42}$$

where ϵ is the slope of the airfoil with respect to the direction of flight and c_1 and c_2 are the following functions of Mach Number:

$$\left.\begin{aligned} c_1 &= -1/\sqrt{M_\infty^2-1} \\ c_2 &= \frac{-1}{4(M_\infty^2-1)^2}[(\gamma-1)\,M_\infty^4+2] \end{aligned}\right\} \tag{43}$$

The boundary condition that λ be zero at the leading edge was used, and the equation was integrated by the method of isoclines. The isocline field and integral curve are shown in Fig. 5.

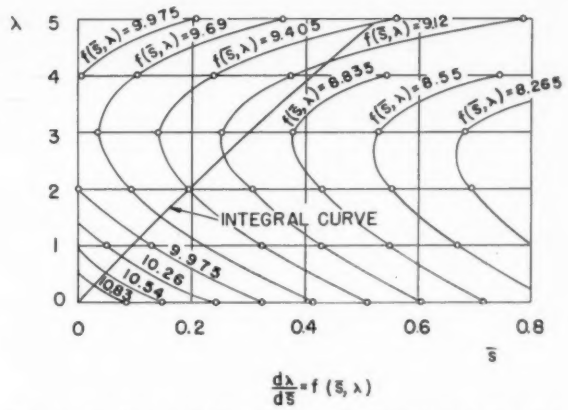

FIG. 5. Isoclines and integral curve for integration of Eq. (21).

(IV) STABILITY; COMPUTATION OF $(R_\theta)_{cr.\ min.}$

This computation is done by applying formulas derived in reference 2. In the notation of this report, these formulas are

$$(R_\theta)_{cr.\ min.} \approx \frac{6}{\bar{T}_w}\,\frac{[\bar{T}(c_0)]^{1.76}}{c_0^4\sqrt{1-M_1^2(1-c_0)^2}} \tag{44}$$

where c_0 is the value for c for which

$$\pi[1-2\,\Xi\,(c)]V(c) = 0.580 \tag{45}$$

Here,

$$V(c) = -c\left(\frac{dw}{d\eta}\frac{1}{\bar{T}}\right)_w\left[\frac{(\bar{T})^2}{(dw/d\eta)^3}\frac{d}{d\eta}\left(\frac{dw/d\eta}{\bar{T}}\right)\right]_{w=c} \tag{46}$$

$$\Xi\,(c) = (\eta_c/c)\,(dw/d\eta)_w - 1 \tag{47}$$

and c is a number, $0 \le c \le 1$. In Eq. (47), η_c is defined by the relation $c = w\,(\eta_c)$.

On the basis of Eq. (7), the temperature ratio $\bar{T}$ may be written as

$$\bar{T} = \frac{1-\bar{u}^2}{1-\bar{u}_1^2}, \qquad \bar{T}_w = \frac{1}{1-\bar{u}_1^2} \tag{48}$$

† See reference 9 for details.

TABLE 3

τ	f	g	$\int_0^\tau f^2\,d\tau$	$\int_0^\tau g^2\,dt \times 10^3$	$\int_0^\tau fg\,dt \times 10^3$	$\frac{df}{d\tau}$	$\frac{dg}{d\tau}$	$\frac{d^2f}{d\tau^2}$	$\frac{d^2g}{d\tau^2}$
0	0	0	0	0	0	2.00	0.200	0	−1.00
0.1	0.200	0.0151	0.00133	0.00878	0.108	1.98	0.104	−0.486	−0.899
0.3	0.573	0.0209	0.0343	0.0911	1.72	1.67	−0.028	−2.65	−0.387
0.5	0.844	0.0109	0.139	0.147	4.04	1.00	−0.056	−3.75	0.0625
0.75	0.986	0.0013	0.357	0.151	5.23	0.206	−0.017	−2.10	0.1600
1.0	1.00	0	0.605	0.153	5.41	0	0	0	0

[f and g are the sixth-order polynomials, Eq. (19)]

Thus,

$$V(c) = -(dw/d\eta)_w \times \cdot \left\{\frac{w}{(dw/d\eta)^3}\left[(1-\bar{u}^2)\frac{d^2w}{d\eta^2} + 2\bar{u}\bar{u}_1\left(\frac{dw}{d\eta}\right)^2\right]\right\}_{w=c} \quad (49)$$

Since our information on the steady-state flow is given in terms of τ, it is necessary to express $dw/d\eta$ and $d^2w/d\eta^2$ in terms of derivatives with respect to τ. Based on Eqs. (11) and (12), one finds

$$\frac{d\bar{w}}{d\eta} = \frac{\partial\bar{u}}{d\tau}\frac{\bar{\delta}}{t(\bar{\delta})}\frac{(1-\bar{u}_1^2)^{\gamma/(\gamma-1)}}{\bar{u}_1(1-\bar{u}^2)} \quad (50)$$

and

$$\frac{d^2w}{d\eta^2} = \left[\frac{d^2\bar{u}}{d\tau^2} + 2\left(\frac{\partial u}{\partial\tau}\right)^2\frac{\bar{u}}{1-\bar{u}^2}\right]\times \left[\frac{\delta}{t(\delta)}\right]^2\frac{(1-u_1^2)^{2\gamma/(\gamma-1)}}{u_1(1-\bar{u}^2)^2} \quad (51)$$

To find $\bar{\delta}/t(\bar{\delta})$. the formula

$$\frac{\bar{\delta}}{t(\bar{\delta})} = \frac{1}{(1-\bar{u}_1^2)^{\gamma/(\gamma-1)}}\times \left[1-\bar{u}_1^2\int_0^1 (f^2+2\lambda fg+\lambda^2g^2)\right]d\tau \quad (52)$$

is valid where the integration is carried out at a fixed $\bar{s}$ and the Eqs. (19) are used for f and g.

Since, for fixed $\bar{s}$, w is known as a function of τ, in order to find η_c it is necessary to know η as a function of τ. This may be found by

$$\eta = \frac{t(\bar{\delta})}{\bar{\delta}}\frac{1}{(1-\bar{u}_1^2)^{\gamma/(\gamma-1)}}\times \left[\tau-\bar{u}_1^2\int_0^\tau (f^2+2\lambda fg+\lambda^2g^2)\right]d\tau \quad (53)$$

For computational purposes one notes that a considerable part of the computations involved in Eqs. (45) through (53) is independent of the value of $\bar{s}$. Consequently, the numerical values of f and g and the necessary integrals and derivatives are tabulated for various τ values in Table 3. These functions are given graphically in reference 9, where, in addition, a computing procedure is given.

REFERENCES

[1] Lees, Lester, and Lin, C. C., *Investigation of the Stability of the Laminar Boundary Layer in a Compressible Fluid*, N.A.C.A. T.N. No. 1115, 1946.

[2] Lees, Lester, *The Stability of the Laminar Boundary Layer in a Compressible Fluid*, N.A.C.A. T.N. No. 1360, 1947.

[3] Hahneman, Elizabeth, Freeman, J. C., and Finston, M., *Stability of Boundary Layers and of Flow in Entrance Section of a Channel*, Journal of the Aeronautical Sciences, Vol. 15, No. 8, pp. 493–496, 1948.

[4] Schubauer, G. B., and Skramstad, H. K., *Laminar Boundary Layer Oscillations and Transition on a Flat Plate*, J. Res. Nat. Bur. Stand., Vol. 38, pp. 251–292, 1947.

[5] Young, E. C., and Wilson, R. E., *First Interim Report on Experimentally Determined Turbulent Boundary Layer Characteristics at Supersonic Speeds*, JHU/APL CF 1095 (U/TEX).

[6] Wilson, R. E., Young, E. C., and Thompson, M. J., *Secondary Interim Report on Experimentally Determined Turbulent Boundary Layer Characteristics at Supersonic Speeds*, JHU/APL CM 501.

[7] Howarth, L., *Concerning the Effect of Compressibility on Laminar Boundary Layers and Their Separation*, Royal Soc. Proc. A, Vol. 194, pp. 16–42, 1948.

[8] Dorodnitzyn, A., *Laminar Boundary Layer in a Compressible Fluid*, Compt. Rend. Acad. Sci., U.S.S.R., Vol. 39, No. 8, pp. 213–219, 1942.

[9] Weil, H., *Effects of Pressure Gradient on Stability and Skin Friction in Laminar Boundary Layers in Compressible Fluids*, General Electric Company Report No. R49A0533, 1950.

[10] Lewis, J. A., *Boundary Layer in Compressible Fluid*, Technical Report No. F-TR-1179-ND Hdqs. Air Materiel Command, Wright Field, Dayton, Ohio, 1948.

[11] Schlichting, H., and Ulrich, A., *Ueber Die Berechnung der Umschlagstelle Laminar—turbulent*, Jahrb. der Deutschen Luftfahrtforschung, Part I, pp. 8–35, 1942.

[12] Oswatisch, K., and Wieghardt, K., *Theoretical Analysis of Stationary Potential Flows and Boundary Layers at High Speed* (translation by J. Vanier), N.A.C.A. T.M. No. 1189, 1948.

[13] Tollmien, W., *Steady Two-Dimensional and Rotationally-Symmetric Supersonic Flows* (Brown University Translation), Analysis Division, Intelligence Dept., Air Materiel Command, Wright Field, Dayton, Ohio, 1948.

The Performance of Axial-Flow Compressors As Affected by Single-Stage Characteristics

SEYMOUR M. BOGDONOFF*
Princeton University

SUMMARY

A series of calculations were carried out to obtain the performance of a six-, an eight-, and a 13-stage compressor, each designed for the same tip speed, to handle the same mass flow, and to develop a pressure ratio of 3.2. The simplified analysis was based on experimental cascade and single-stage studies. The effects of boundary-layer growth and distortion of the velocity profiles, which occur at the rear of multistage axial-flow compressors, were neglected.

(I) INTRODUCTION

THE SIMPLE BLADE ELEMENT THEORY of axial-flow compressor design has been widely used, both in actual compressor design and in analysis, to determine the effects of many design parameters. The theory, however, gives no indication of the physical limitations of the calculations. The maximum pressure ratio per stage, maximum turning angles, or Mach Numbers must be determined from experimental tests. From many tests of multistage compressors, a "rule of thumb" has appeared which states that, for highest efficiency, widest range, and best stalling characteristics, the number of stages should be large—i.e., the pressure ratio per stage should be small. It is important to note, however, that most of these tests were conducted on machines designed without the benefit of many recent cascade and single-stage studies. It has been shown conclusively in recent rotor tests[1–3] that the efficiency of properly designed blades can be kept high even with extremely high loadings. This permits the design of efficient compressors that can deliver a desired pressure ratio in fewer stages than was previously possible.

It is the purpose of this paper to examine the effect of single-stage characteristics on the overall performance of multistage axial-flow compressors. The single-stage variables to be studied are the blade loading or pressure rise per stage and the efficiency variation with mass flow. The overall multistage performance will be examined particularly with reference to the range of operation with good efficiency and the stalling characteristics. The analysis is, of necessity, a simplified one. Since information is not available to evaluate the effects at the rear of a multistage compressor, the compressors to be studied are assumed to be made up of a series of single stages. The performance of each of these stages can be calculated from theory and actual single-stage tests with a relatively high degree of accuracy. The analysis will, therefore, neglect the effects of multistaging connected with the trailing vortexes (distortion of the velocity profiles downstream) and boundary-layer growth. The calculations are based on experimentally determined efficiency curves, stalling data, and two-dimensional cascade data. It is believed that the results obtained give a good qualitative picture; the actual quantitative results must wait for a more complete understanding of the many multistage effects.

Received November 22, 1949. Revised and received October 13, 1950.

* Assistant Professor of Aeronautical Engineering.

(II) GENERAL PROCEDURE OF CALCULATION

The general procedure was as follows: Three compressors were designed with six, eight, and 13 stages to develop a pressure ratio of about 3.2 and all handling the same mass flow. The rotational speed at the mean blade height was taken as 684 ft. per sec. and the design axial velocity as 450 ft. per sec. for all cases. The only variable was the loading of each stage—i.e., the pressure rise, lift coefficient, or turning angle. These axial and rotational velocities are in the operating range of many commercial axial-flow compressors in use today and were chosen only to give numerical results. All stages in each design had the same vector diagram at the mean blade height. This vector diagram was symmetrical—i.e., the stage was of the 50 per cent reaction type at the mean blade height. The design stagger angles β (defined as the angle between the entering air and the perpendicular to the blade row) and the turning angles θ (defined as the deflection of the air passing through the blade row) are shown in Table 1 for the three compressors. The product of lift coefficient and solidity, σC_L, is also included in this table.

These designs were completed to the point of actual blade-shape design and were found to be within the region covered by references 2 and 4. The mass flow

TABLE 1

Design Conditions at the Mean Blade Height

Compressor	β, Deg.	θ, Deg.	σC_L
6-stage	49.17	29.02	1.47
8-stage	46.5	21.08	1.11
13-stage	43.15	12.97	0.70

through each compressor was then varied by steps from the flow that would stall the compressor to the flow that would cause part of the compressor to act as a turbine. The turning angles were predicted from the angle of attack and blade section using cascade data.[4, 2] For each stage, the efficiency was determined from the data in references 1 and 3. This procedure is necessarily a step-by-step one, since each blade row is treated separately. From the final blade row, the overall pressure ratio and efficiency were calculated. This procedure was repeated with different rotational speeds and a second single-stage efficiency curve.

(III) Assumptions and Approximations

The assumptions and approximations included in the calculations are indicated below. A detailed discussion of the effects of each of these on the final results is given later in the paper.

(1) The mean blade height was held constant for all stages. The flow path then looked like that shown in the sketch below.

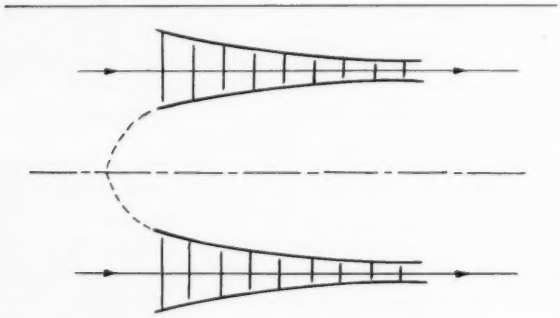

(2) The slope of the $d\theta/d\alpha$ curve was taken to be a constant value of 0.9, where θ is the turning angle through the blade row and α is the angle of attack.

(3) A single composite curve of efficiency vs. mass flow for a single stage was developed using twice the losses shown for a rotor in references 1 and 3, Fig. 1.

(4) The effects of Reynolds Number and Mach Number were neglected.

(5) No effect of the change of boundary-layer thickness on the walls was included.

(6) Calculations of each blade row were based on conditions entering the row.

(7) Constant entrance pressure and temperature (2,116 lbs. per sq.ft. and 560°R.) were assumed.

(IV) Detailed Calculations

From the original design of each compressor, the passage areas and blade angles were known (corresponding to design mass flow and performance). The axial velocity was constant at 450 ft. per sec. through each machine at design conditions. To find the effect of varying the mass flow, a new mass flow was chosen, and the axial velocity entering the guide vanes was changed accordingly. The turning angle did not change, since the entering flow is still axial, but the absolute velocity has changed. The pressure and temperature after the guide vane was calculated from

$$T_0 = T_2' + (V_2'^2/2C_p)$$

and

$$P_2'/P_0 = [T_2'/T_0]^{[\gamma/(\gamma-1)]\eta}$$

where

T = temperature, °R.
V = absolute velocity, ft. per sec.
P = pressure, lbs. per sq.ft.
C_p = specific heat of air at constant pressure
η = efficiency (assumed 100 per cent for guide vanes), stage efficiency determined from single-stage data
γ = ratio of specific heats
$()_0$ = stagnation conditions ahead of compressor
$()_2$ = flow after guide vane
$()'$ = new flow caused by change in entrance mass flow

The density can be computed from

$$P = \rho RT$$

where ρ = density and R = gas constant. With the passage area known from the original design and with the density calculated as above, the continuity equation can be used to calculate the axial velocity leaving the blade row.

The absolute tangential velocity is known from the axial velocity and the turning angle, so the angle relative to the rotating blade row can be obtained. The new angle of attack of the rotor blade is then known, and the change in turning angle is calculated from $d\theta/d\alpha = 0.9$. The new leaving velocity can then be calculated, and the pressure and temperature can be found as above. The new density is found, and the axial velocity is calculated again from the known mass flow, density, and area. This procedure was repeated for each blade row. The overall pressure ratio was taken as the ratio of exit static pressure to inlet static pressure. The efficiency was calculated from $\eta = \Delta T_{th}/\Delta T_{act}$, where ΔT_{th} was the value obtained adiabatically from the pressure ratio.

These calculations were carried out at a constant blade radius (actually one-half way between the root and tip of the blade) and therefore are independent of the flow type through the compressor. The results are, of course, an approximation to the actual flow, since the flows at the root and tip sections of the blade are not directly calculated. They are included, however, to some extent by the use of an efficiency curve obtained from actual tests of the three-dimensional blade row designed for free-vortex flow. This efficiency curve must be modified for flow types

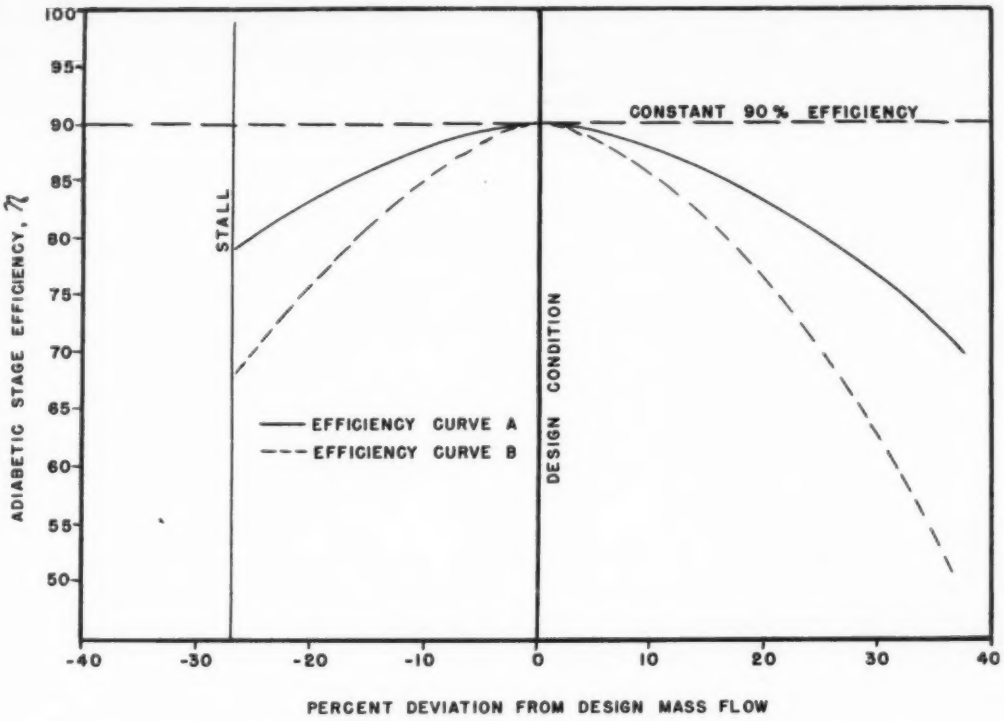

FIG. 1 EFFICIENCY VARIATIONS USED IN CALCULATIONS

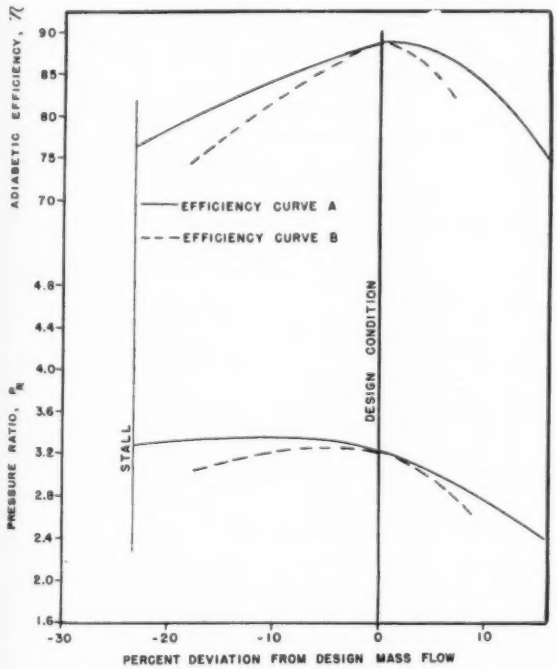

FIG. 2 EFFICIENCY AND PRESSURE RATIO CHARACTERISTICS OF THE SIX STAGE COMPRESSOR

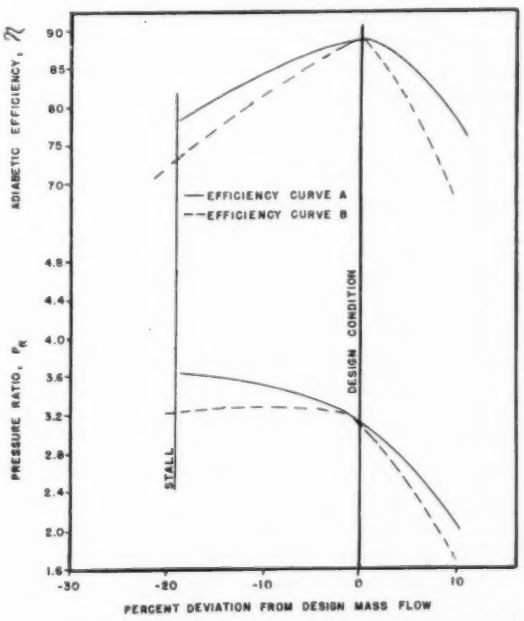

FIG. 3 EFFICIENCY AND PRESSURE RATIO CHARACTERISTICS OF THE EIGHT STAGE COMPRESSOR

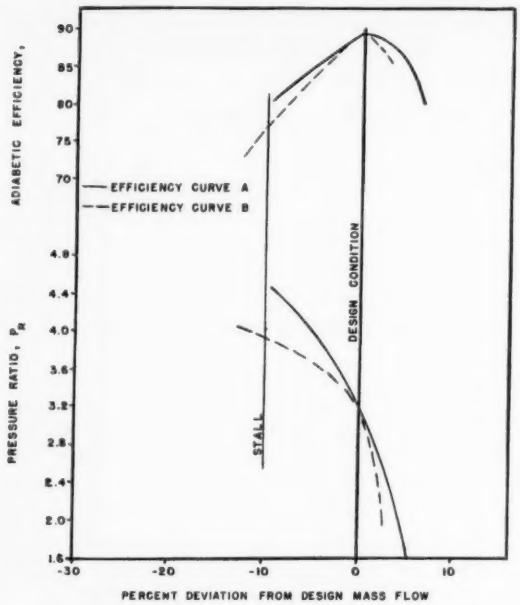

FIG. 4 EFFICIENCY AND PRESSURE RATIO CHARACTERISTICS OF THE THIRTEEN STAGE COMPRESSOR

other than free vortex. In general, the results seem to be similar if the blade shapes are properly designed, as shown by a comparison of the results of references 1 and 5.

Stalling of the compressor was arbitrarily taken when one or more blade rows reached the stalled condition. This point was found to be a constant 27 per cent below design axial velocity if the design condition was taken to be the point of *maximum efficiency* instead of the point used in references 1 and 3. Therefore, with a design axial velocity of 450 ft. per sec., the compressor was considered stalled if the velocity entering any blade row dropped to 328.5 ft. per sec.

(V) Results and Discussion

(A) *Performance Curves and Range*

The overall performance of each compressor is summarized in Figs. 2–4. It is immediately apparent that a change in the number of stages has a strong effect on the shape of the pressure ratio and efficiency curves. Increasing the number of stages steepens the curves, although all three compressors have the same pressure ratio, about 3.2, and efficiency, 88.5 per cent, at the design conditions. The pressure ratio for the six-stage compressor varies between 2.2 and 3.35 in its operating range, while the 13-stage machine varies from 2.2 to almost 4.5. This steepening of the curves associated with increasing number of stages was found to be true also for staged centrifugal compressors (Pfau[6]).

The most striking point, however, is the large increase in operating mass-flow range shown by the machine with highly loaded stages. The eight-stage machine has a range of good operating characteristics of twice that of the 13-stage machine, while the six-stage machine has a range of almost three times that of the 13-stage machine. (See Table 2.)

Table 2
Range Analysis, Curve A

	Range, % Design Mass Flow
6-stage compressor	41
8-stage compressor	28
13-stage compressor	14

The range is defined as the per cent change in mass flow from stalled conditions to the point where the pressure ratio dropped to 2.2. At this point for all compressors, the last stage was operating as a turbine. For any deviation from the design point, the fewer the number of stages, the higher the efficiency and the lower the change in pressure ratio. This would, of course, only hold up to the case where further increases in blade loading gave decreased performance of the single-stage machine. The range shown for the six-stage machine is considerably more than that shown by any axial-flow compressor in operation today. It has been shown by Howell that the outlet air angle has a considerable effect on multistage performance, but the results obtained cannot be explained on this basis alone. It should be noted that the steeper characteristics, with the associated greater pressure ratio range, may be more desirable for some applications such as gas turbines.

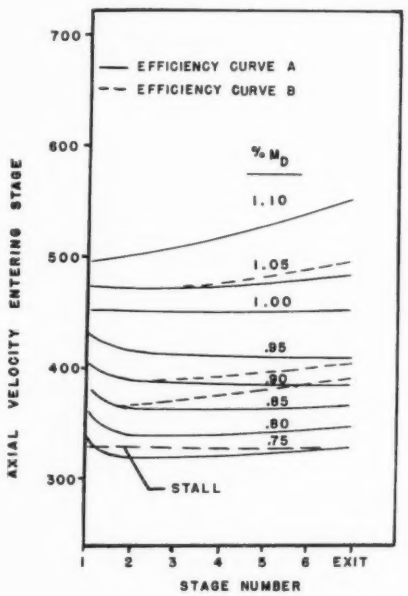

FIG. 5 AXIAL VELOCITY DISTRIBUTION THROUGH THE SIX STAGE COMPRESSOR

To show the cause of the change in shape of performance curves with the number of stages, the axial velocity distributions through each compressor for various mass flows are shown in Figs. 5–7 (all plotted to the same scale; M_d designates the design mass flow). From these curves, it can be seen that, for a given change in mass flow, the change in axial velocity through the compressor increases with the number of stages. This effect is due to a combination of two factors: (1) the "reheat factor" or the inherent higher efficiency of the more highly loaded stages and (2) a given change in mass flow gives a smaller percentage change in pressure ratio for the more highly loaded blade rows.

The first of these, the "reheat factor," can best be understood by comparing one stage of the six-stage machine to two stages of the 13-stage machine. Both of them will give about the same pressure ratio. From the rotor tests of references 1 and 3, the maximum efficiency for both sets of blade rows is the same. The one stage of the six-stage machine may have an efficiency of 90 per cent; therefore, the overall efficiency of the unit we are considering (one stage) is 90 per cent.

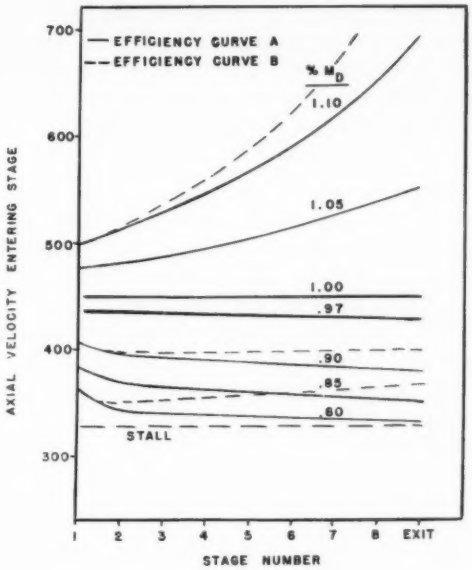

FIG. 6 AXIAL VELOCITY DISTRIBUTION THROUGH THE EIGHT STAGE COMPRESSOR

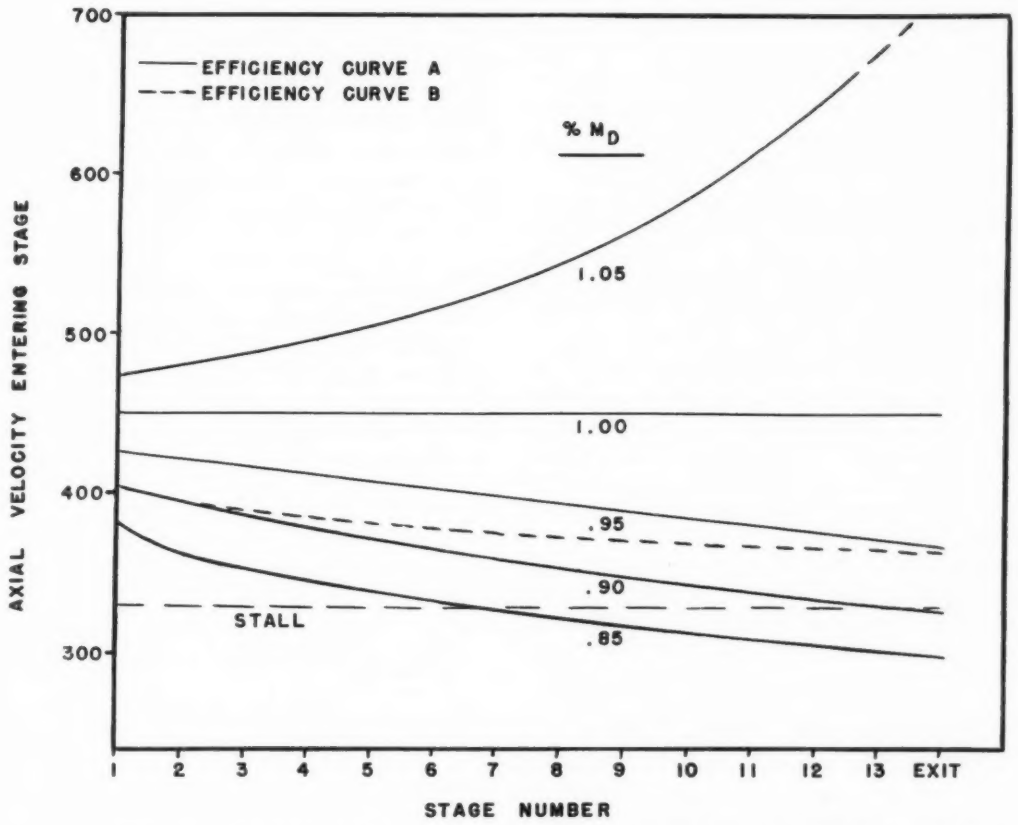

FIG. 7 AXIAL VELOCITY DISTRIBUTION THROUGH THE THIRTEEN STAGE COMPRESSOR

The two-stage unit, however, is made up of two 90 per cent efficient stages, and, since the second stage must operate with a higher inlet temperature, the overall efficiency of the two-stage unit is less than 90 per cent. This "reheat factor" is small and, in these calculations, seems to have a secondary effect.

The important factor in the change of shape of the performance curves is the percentage change in pressure ratio or axial velocity which occurs for a given change in mass flow. If the three compressors are compared from this point of view, it is obvious that the machine with the most lightly loaded blades will be most critical. The same change in angle of attack gives a much greater change in pressure ratio (as a percentage) for the stage with a light loading than for one that is highly loaded. In other words, for a given change in angle of attack (caused by a change in mass flow) the blade row with the highest turning angle is least affected. As an example, compare the axial velocities entering the second stage of the six-stage machine and the third stage of the 13-stage machine when the mass flow is 0.85 of design. In the original designs, the pressures developed at these points were about equal, and the axial velocity was 450 ft. per sec. In the six-stage machine, the axial velocity is now about 5 per cent less than the entering velocity, while the axial velocity in the 13-stage machine has dropped to 7.8 per cent less than entering velocity. This corresponds to an efficiency of 83.1 per cent for the following stage of the six-stage unit and an efficiency of only 82 per cent for the following stage of the 13-stage unit.

The performance of the six- and eight-stage compressors was also calculated for 0.6 and 0.8 design r.p.m., although the accuracy of the calculations decreases with decreasing rotational speed. The results of these calculations, combined with the performance curves at the design r.p.m., are shown in Figs. 8 and 9. The steeper characteristics of the eight-stage machine are still noticeable. At 0.8 design r.p.m., the six-stage machine has a mass flow range of about 35 per cent more than the eight-stage machine (compared with 50 per cent more at the design r.p.m.). Below 0.8 design r.p.m., the conditions are so far from design that there is little effect of number of stage. It is interesting to note that the constant efficiency contours of Figs. 8 and 9 are of similar shape. Therefore, the mass-flow range of any machine depends primarily on the steepness of the pressure ratio curve; the flatter the curve, the greater the range.

(*B*) *The Effect of Single-Stage Efficiency Variation*

The entire analysis, so far, has been based on one single-stage efficiency curve (designated Curve A). This curve was obtained by assuming that a stage would have twice the losses found in the rotor tests of references 1 and 3. This assumption may be considered conservative, since the losses in a stator are not so large as those in a rotor. However, this efficiency variation with mass flow may be overly optimistic when applied to blading at the rear of a compressor where the flows are not uniform and the boundary-layer effects are large. This also may be the case at low Reynolds Numbers or high Mach Numbers. To study the effect on the material thus far presented of changing this efficiency curve, a second curve (designated Curve B) was derived. This curve had the same peak efficiency as the first curve but with losses twice that of Curve A off the design point. A third case, that of completely neglecting the efficiency variation (assuming a constant 90 per cent efficiency), was also studied. The three curves are presented in Fig. 1.

Spot checks were carried out on the six- and 13-stage compressors, and a complete study was made of the eight-stage compressor with efficiency Curves B and the constant 90 per cent curve. The effect on the overall performance caused by using Curve B is shown by the dashed lines in Figs. 2–4. The general effect is to flatten out the pressure curves and peak the efficiency curves, but the results presented in Section (A) are still valid. It is important to note that the greater the number of stages, the more sensitive the compressor is to changes in the efficiency curve.

The effect of using Curve B on the internal flows is shown as dashed lines in Figs. 5–7. The axial velocity in all cases is increased at the exit of the compressor and in most cases causes a reversal in slope of the velocity curve. Since the axial velocity through the whole compressor is increased to some degree, stalling will occur at a lower mass flow than in the original case. The range is therefore changed and is compared in Table 3. There is still a significant increase in range with fewer stages, but the increase is not so large as shown in Section (A) using efficiency Curve A.

The effect of neglecting the efficiency variation altogether means that the blade row is assumed to be able to operate over a wide range of angles of attack with no change in efficiency. The effect of such an assumption on the eight-stage compressor at 0.85 design mass flow is compared in Table 4 with the

TABLE 3
Range Analysis, Curve B

	Range, % Design Mass Flow
6-stage compressor	37
8-stage compressor	29
13-stage compressor	17

TABLE 4
The Eight-Stage Compressor, 0.85 Design Mass Flow
Design R.P.M.

	Pressure Ratio	Efficiency
Efficiency Curve A	3.6	80.6
Efficiency Curve B	3.3	76.6
Constant 90 per cent efficiency	4.1	88.2

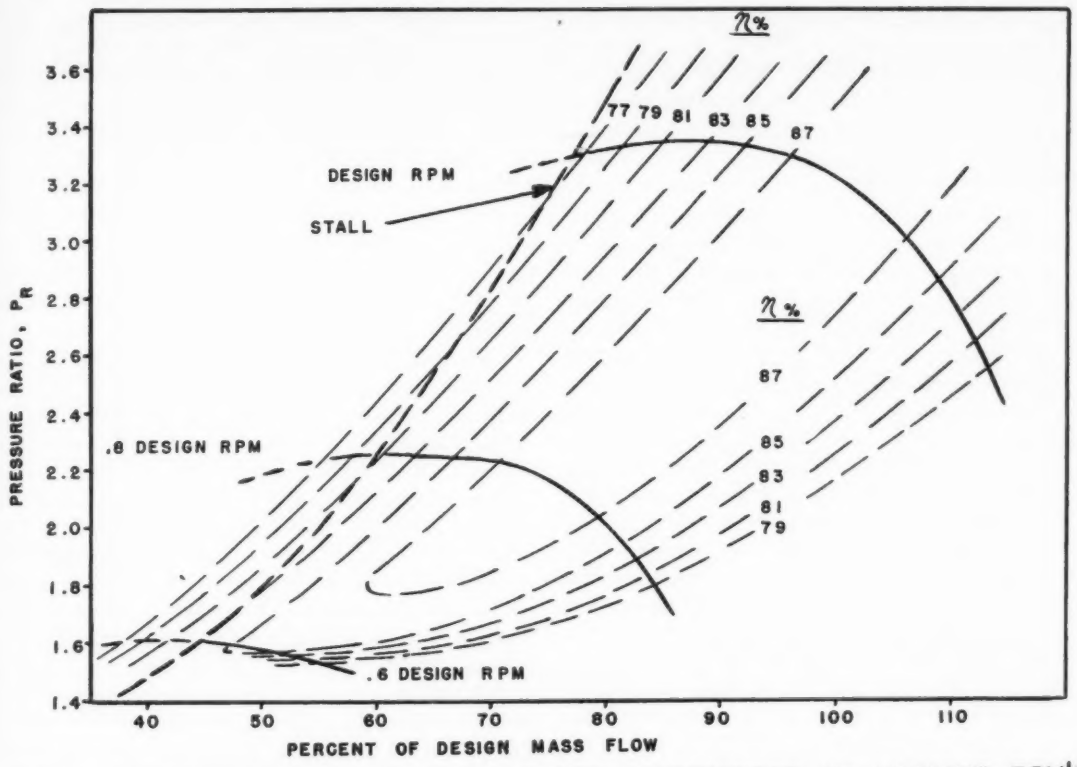

FIG. 8 PERFORMANCE OF THE SIX STAGE COMPRESSOR AT VARIOUS RPM'S

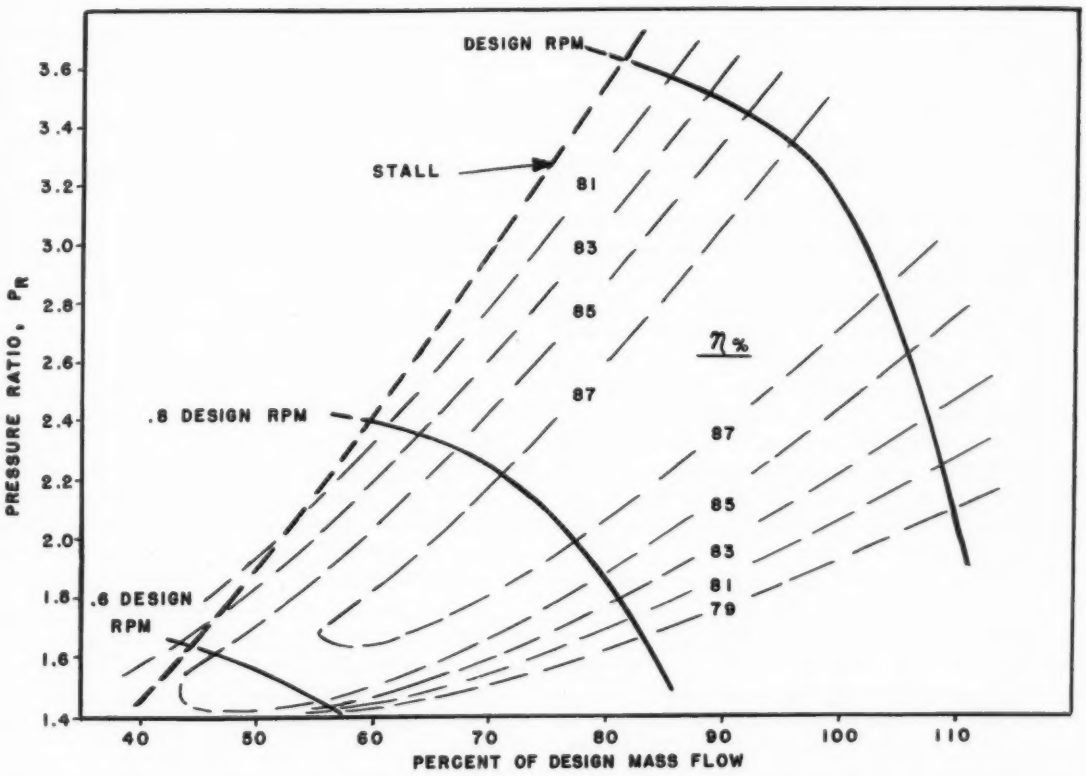

FIG. 9 PERFORMANCE OF THE EIGHT STAGE COMPRESSOR AT VARIOUS RPM'S

results obtained with efficiency Curves A and B. The effect on the axial velocity distribution is shown for the same cases in Fig. 10.

(*C*) *Stalling Characteristics*

In the previous sections of this paper, stalling of the compressor was taken as the point where the axial velocity entering any blade row dropped to the value that stalled the blade row in the tests of references 1 and 3. This point may or may not be the point at which the whole compressor stalls. It is generally believed that a multistage compressor stalls at the rear first. This conclusion is reached from the following simple picture of the flow through the compressor when the axial velocity entering the first stage is below the design velocity. The blade angle of attack will then be higher than the design angle, and the first stage will develop a pressure ratio that is also higher than the design. Since the flow area is fixed and the density is higher than design, the axial velocity entering the next stage will be lower than that entering the first stage. This leads to a still higher angle of attack and pressure ratio for the second stage, and, as a consequence, conditions entering the following stage are still further from design conditions. If this crude picture is carried to the end, it is at once obvious that the conditions at the exit of the compressor are furthest from design conditions and so will stall first.

If, however, this off-design flow is examined a little more carefully than above, the general results change completely. When a stage operates off its design point, the efficiency decreases and, to some degree, counteracts the increase in pressure rise caused by the increased angle of attack of the blades. This is clearly seen in the axial velocity profiles shown in Figs. 5, 6, 7, and 10.

It is apparent that only for the 13-stage compressor, with efficiency Curve A, is it possible for the last stages to stall first. In this one case it seems probable that as the mass flow is decreased the last stage stalls and that, with further decreases, more and more stages at the rear will stall. At some point the increased resistance of the stalled stages will completely stall the compressor. However, if the actual single-stage efficiency curve is similar to Curve B, then the above no longer holds true, since the axial velocity is almost constant through the compressor. The stalling of one blade row will, in all probability, stall the entire compressor.

This complete stalling will also hold true for the six- and eight-stage compressors with efficiency Curve A. With efficiency Curve B, the critical stages are definitely at the front of the compressor. The question that has yet to be answered is whether a blade row operating near its stall point will be stalled by the fluctuations in velocity caused by a preceding stalled blade row. Actually, this same question must also be answered for the case of a following stalled blade row. The answers to these questions are beyond the scope of this paper and must be determined by actual experiments. The answer will necessarily depend on how far from stall the blade row is operating. Below the design r.p.m., for example, the axial velocity increases rapidly through the compressor, Fig. 11, and so it is likely that, although the first stage or two may be stalled, the axial velocities at the rear of the compressor will be high enough for the rear blade rows to operate unstalled.

If it is desirable to have a "soft stall"—that is, have the last stages stall first to give warning of approaching complete stall—it seems possible to design blading to give this effect. If the original designs are used as examples, blade sections are alike for each blade row of each compressor, since all vector diagrams are similar and symmetrical. From the flat axial velocity distributions, all stages will stall almost simultaneously. If, however, the same blade section is not used for each row, some determination of the stalling is left with the designer. By using blades of higher camber than optimum at the front of the compressor and operating at lower angles of attack, the compressor will be forced to stall at the exit. The blade rows at the front will still be some distance from stall when conditions at the rear cause the unmodified blade rows at the rear to stall. This overcambering will cause a drop in efficiency, but, considering the flat efficiency curve of a well designed blade row,[1, 3] it may not be excessive. Of course, the high mass-flow end of the performance curve will also be affected, since the blade rows at the front of the compressor will be operating further from their optimum point than those in the original design.

(*D*) *Effects of Assumptions and Approximations*

(1) The choice of constant mean blade height was chosen only for ease of computation. The vector diagrams at the design conditions then become similar for all stages. This choice of geometry has no general effect on the conclusions reached.

(2) The choice of a constant value of $d\theta/d\alpha = 0.9$ was also based on ease of computation. However, the results of reference 4 show that this is a good average value in the operating range of blades with a solidity of about 1.0. The approximation becomes bad near the stall and turbine-action points. One check on the eight-stage compressor using an experimentally determined turning angle curve showed no serious deviations from the results presented.

(3) The efficiency Curve A was derived from tests of four blades of various loadings of references 1 and 3. The inclusion of results with efficiency Curve B and a constant 90 per cent efficiency allows the evaluation of any single-stage efficiency curve by direct comparison. The effect of having a lower peak efficiency is to accent the sensitivity of the compressor with the more numerous stages. The axial velocity at the exit for

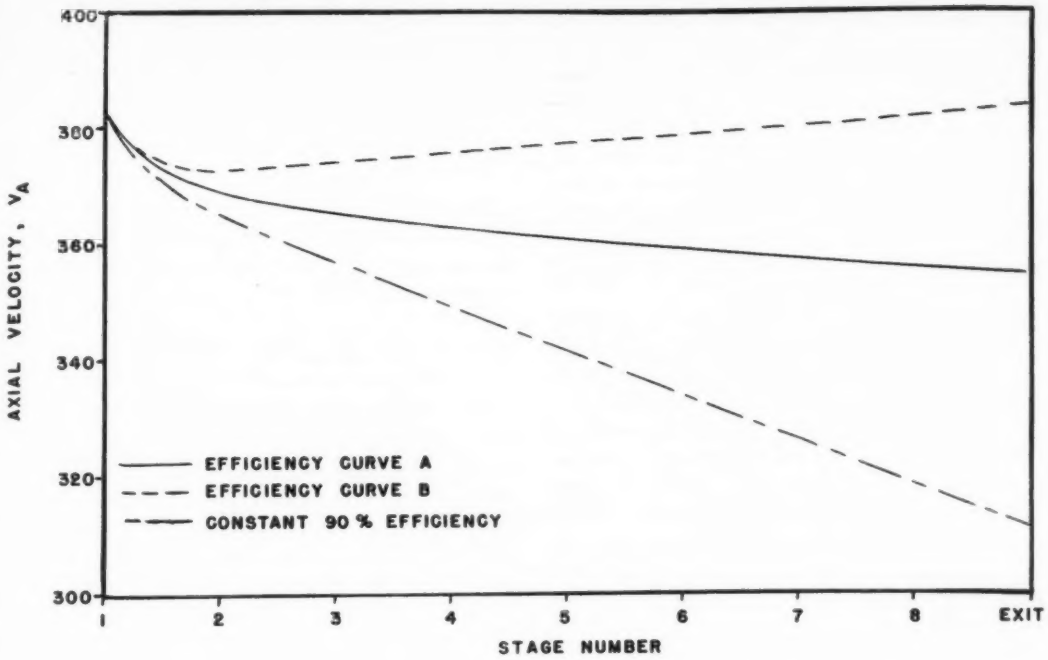

FIG. 10 COMPARISON OF AXIAL VELOCITY DISTRIBUTION FOR THE EIGHT STAGE COMPRESSOR AT .85 M_D WITH VARIOUS EFFICIENCY VARIATIONS

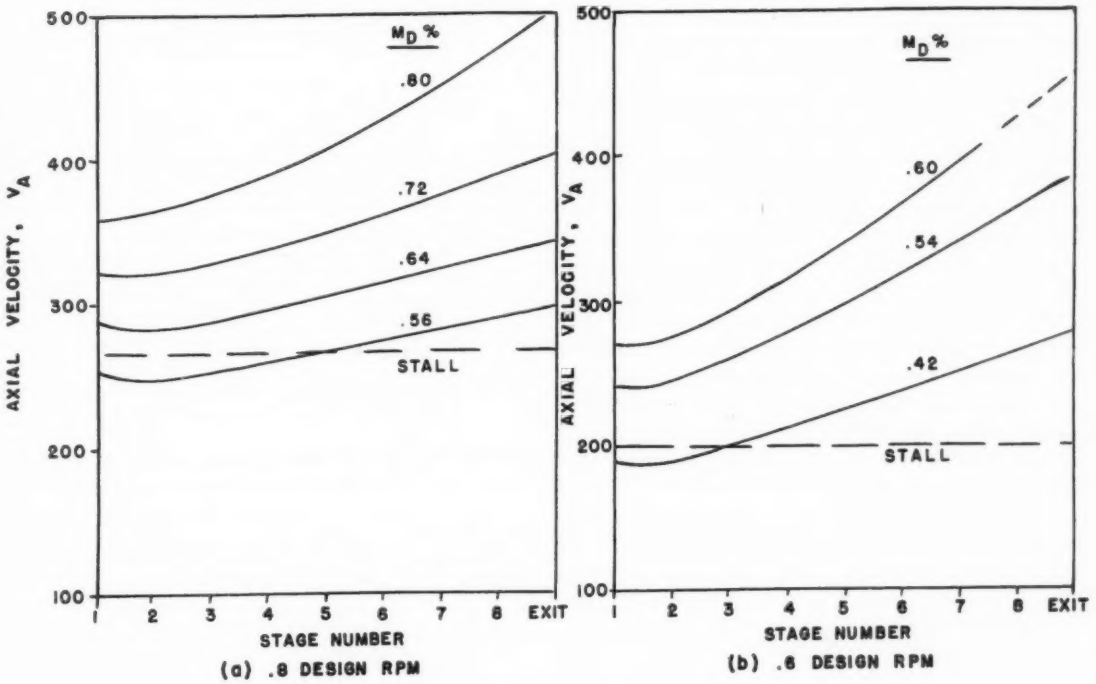

FIG. 11 VARIATION OF AXIAL VELOCITY OFF THE DESIGN RPM

off-design conditions will always be higher for the lower stage efficiencies.

(4) It was assumed that the blades were operating above a Reynolds Number of about 200,000 and far enough below the critical speed so that compressibility effects were not present. For the conditions studied, the Mach Number was considerably below critical conditions.[7] The effects of both Reynolds Number and Mach Number can be evaluated, if single-stage tests are available, by simply substituting the corrected efficiency and turning-angle results.

(5) No effect of the change in boundary-layer thickness on the walls was included because little information is available on the subject. These effects will be greatest at the rear of the machine, tending always to increase the axial velocities. There is no experimental basis for saying whether or not the effect will be greatest for the six- or 13-stage compressor. However, since both develop about the same pressure ratio and the 13-stage machine will be considerably longer than the six-stage machine, it seems probable that the effect will be greatest on the compressor with the greatest number of stages.

(6) Again, for ease of computation, performance of each blade row was based on the entering axial velocity. To be absolutely correct, the mean of the entering and leaving velocities should be used.[3, 5] For all cases at the design r.p.m., below the design mass flow, the effect of using the entering velocity is negligible because the velocity changes are small. Above the design mass flow for the eight- and 13-stage compressors, the effects are noticeable but small, tending to steepen the curves (increase the exit velocity). The same effect is found to a much greater degree for the 0.6 and 0.8 design r.p.m. cases. Spot checks indicate that the general results are still valid, but for better accuracy (if needed) the calculations should be done with the mean velocities.

(7) The entrance pressure and temperature were chosen to simulate normal sea-level operation. The choice of these factors has no effect on the general results, since all three basic designs operate at the same conditions.

(8) The effect of the important multistage effects of boundary-layer growth, trailing vortexes, and distortion of the velocity profiles cannot be evaluated by any means known to the author except by experiments. It is believed that these effects will undoubtedly change the actual figures that were obtained, but the general results will still be valid. The choice of axial and rotational velocities used in the calculations also have no significant effects as long as the blades operate in a region where Reynolds Number and Mach Number effects can be neglected.

(VI) Conclusions

A simplified performance analysis of multistage axial-flow compressors was used to compare the performance of a six-, an eight-, and a 13-stage compressor, each designed to handle the same mass flow and develop a pressure ratio of 3.2.

The following conclusions were reached:

(1) The compressor with the fewest stages (highest loaded stages) has the widest mass-flow range. The six-stage compressor has a range of mass flow of 41 per cent of design mass flow; the eight-stage, 28 per cent; and the 13-stage, only 14 per cent.

(2) The compressor with the fewest stages has the flattest pressure ratio and efficiency variation with mass flow. The more numerous the stages, the steeper the characteristics—i.e., the greater the pressure ratio range.

(3) The flat characteristics are due primarily to the fact that, for a given change in mass flow, the percentage change in developed pressure ratio or axial velocity is smallest for highly loaded blades.

(4) The calculations show that, for most configurations, stalling of a multistage compressor occurs throughout the compressor at the same instant. This is in contradiction to the usual belief that stalling occurs first at the rear and progresses forward.

(5) A method is suggested for forcing the compressor to stall at the rear first. This may be a way to eliminate the sudden sharp stall usually associated with multistage compressors.

References

[1] Bogdonoff, S. M., and Herrig, L. J., *Performance of Axial-Flow Fan and Compressor Blades Designed for High Loadings*, N.A.C.A. T.N. No. 1201, 1947.

[2] Bogdonoff, S. M., and Hess, E. E., *Axial-Flow Fan and Compressor Blade Design Data at 52.5° Stagger and Further Verification of Cascade Data by Rotor Tests*, N.A.C.A. T.N. No. 1271, 1947.

[3] Herrig, L. J., and Bogdonoff, S. M., *Performance of an Axial-Flow Compressor Rotor Designed for a Pitch-Section Lift Coefficient of 1.20*, N.A.C.A. T.N. No. 1388, 1947.

[4] Bogdonoff, S. M., and Bogdonoff, H. E., *Blade Design Data for Axial-Flow Fans and Compressors*, N.A.C.A. A.C.R. No. L5Fo7a, 1945.

[5] Kahane, A., *Investigation of Axial-Flow Fan and Compressor Rotors Designed for Three-Dimensional Flow*, N.A.C.A. T.N. No. 1652, 1948.

[6] Pfau, H., *Effect of the Performance of Individual Stages on the Overall Characteristics of Multi-stage Super-Chargers*, R.T.P. Translation No. 1425. (Jahrb. d. deutsch. L.F.F., Vol. II, pp. 196–202, 1938.)

[7] Bogdonoff, S. M., *Performance of Compressor Blade Cascades at High Mach Numbers*, N.A.C.A. Research Memorandum No. L7D11a, 1947.

Coupled Free Vibrations of a Swept Wing

A. E. ENGELBRECHT*
North American Aviation, Inc.

ABSTRACT

This paper presents a method by which the natural frequencies of the coupled free vibrations of a swept wing can be approximately determined.

The continuous elastic structure of the actual swept wing is approximated by a composite wing consisting of a finite number of sections. Each section contains a concentrated mass located at the outboard end of the section and an inboard weightless elastic bar of either straight or circular arc plan form. The choice as to whether the straight or circular arc bar is used in any section is determined by whichever form more nearly coincides with the locus of elastic centers of the section.

The usual assumptions of thin bar theory are made. Loads other than inertial loads are neglected, and the elements of the sections are assumed to be in harmonic motion.

A set of six equations is developed for each section. Each equation relates a shear, bending moment, slope, deflection, torque, or angle of twist at the inboard end of a section to the shear, bending moment, slope, deflection, torque, and angle of twist at the outboard end. The six relationships are then combined into a single matrix equation for each section. A trial frequency is then substituted into each of the section matrices, and by successive matrix multiplication a single matrix for the entire wing semispan is obtained. If the trial frequency chosen is a natural frequency, the boundary conditions will be satisfied. If the boundary conditions are not satisfied, additional trial frequencies must be tried. Methods for determining proper frequency choices are shown, together with a numerical example in the paper.

INTRODUCTION

ONE OF THE RECENT TRENDS in the aerodynamic design of high-speed airplanes is toward the use of the swept wing. This paper presents a method by which the natural frequencies of the coupled bending and torsional free vibrations of a swept wing can be approximately determined. The continuous elastic wing is replaced by a composite wing containing a finite number of masses connected by weightless supporting structure.

(A) *Methods of Solution*

The methods usually used to determine the natural frequencies and deflection patterns of composite wing replacements for actual straight wings fall into two broad classes. The one class contains the trial deflection methods in which an initial arbitrary bending and torsional deflection pattern is assumed, and the other class contains the trial frequency methods in which an initial arbitrary frequency is assumed.

Two methods of the first class that have been successfully used on straight wings are the method of numerical integration[1–3, 5] and the matrix iteration method.[4, 6, 13] The method of the second class follows the ideas developed by Holzer[3, 9, 10] and employs an arbitrarily chosen frequency. Operationally, the methods of these two classes are designed to converge the initial arbitrary choice of the deflection pattern in the trial deflection methods and frequency in the trial frequency method to its true value in the composite system. The method developed in this paper is an extension of the trial frequency method, which will determine the coupled free vibrations of a swept wing.

(B) *Procedure*

The composite wing used to approximate the actual swept wing consists of a finite number of sections where each section contains a concentrated mass at the outboard end and an inboard weightless bar of either straight or circular arc plan form.

A set of six equations relating the boundary conditions at one end of each section to the boundary conditions at the other end of the section is developed. These equations relate the shear, bending moment, slope, deflection, torque, or angle of twist at the inboard end of the section to the shear, bending moment, slope, deflection, torque, and angle of twist at the outboard end. The six relationships are then combined into a single matrix equation for each section.

After the matrix equations have been written for each section of the wing semispan, a trial value of the frequency is selected, and its value is substituted into the section matrices. Then the matrix representing the tip section is premultiplied by the matrix representing the section just inboard of the tip. The product of these two is then premultiplied by the matrix representing the next inboard section. This successive premultiplication is continued until a single matrix equation for the entire wing semispan is obtained.

The matrix equation for the entire wing semispan is then reduced to a set of six equations. Each equation relates one of the above-mentioned boundary conditions at the center of the wing span to the boundary conditions at the tip.

At the tip of the wing the shear, bending moment, and torque are equal to zero. At the midspan of the wing for symmetric free vibrations the shear, slope, and torque must equal zero. At the midspan of the wing for antisymmetric free vibrations the bending moment, deflection, and angle of twist must equal zero.

If the trial value of the frequency chosen were a natural symmetric or antisymmetric frequency, the

Received August 30, 1950.

* Vibration Engineer.

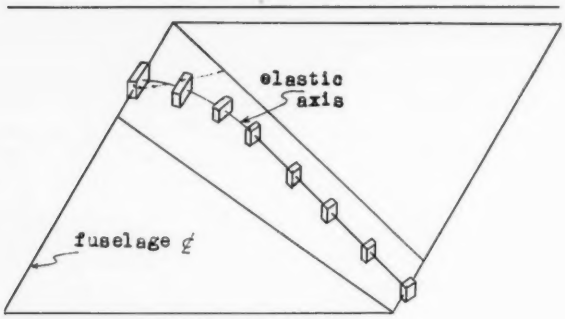

FIG. 1. Vibrating system.

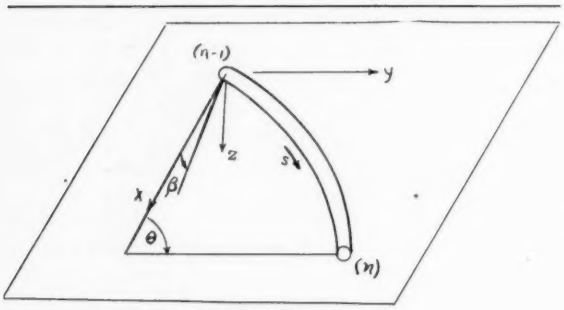

FIG. 2. Coordinate system.

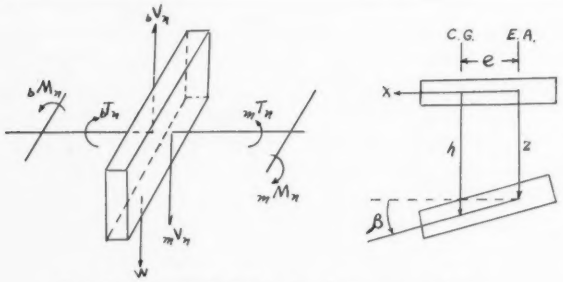

FIG. 3. Dynamic free body of concentrated mass.

applicable boundary conditions at the tip and the center of the wing span would be satisfied. If the boundary conditions are not satisfied, a new trial frequency must be selected and the procedure repeated. A procedure that also helps in choosing subsequent trial frequencies will be described in the next section.

SYMBOLS

W = weight of section of wing, lbs.
I = bending moment of inertia of area of section of wing with respect to chordwise axis, normal to elastic axis, in.^{4}
E = bending modulus of elasticity of beam, lbs. per in.^{2}
G = shear modulus of elasticity of beam, lbs. per in.^{2}
J = polar moment of inertia of area of section of wing with respect to the elastic axis, in.^{4}
S = static unbalance about wing elastic axis, in.lbs.
I = weight polar moment of inertia of wing section with respect to the elastic axis, lb.-in.^{2}
R = radius of curvature of bar section, in.
θ = circular arc bar section central angle, rad.
s = distance along elastic axis, measured from inboard end of section, in.
e = distance from elastic axis to center of gravity of section, in.
h = vertical displacement of section center of gravity, in.
L = length of bar between masses of straight bar section, in.
ω = frequency of coupled vibration, rad. per sec.
t = time, sec.
g = acceleration of gravity, in. per sec.^{2}
K = frequency factor, ω^2/g, rad.^{2} per in.
n = subscript denoting section number
m = subscript denoting mass
b = subscript denoting bar

DYNAMICAL ANALYSIS OF SWEPT WINGS

Consider a continuous elastic swept aircraft wing whose section properties and mass distribution are not uniform. The continuous elastic system is approximated by a system containing a finite number of masses connected by weightless elastic bars. The wing is thus divided into a finite number of sections, where each section contains a concentrated mass and its inboard weightless bar. A typical division is shown in Fig. 1.

A weightless bar of either straight or circular arc plan form is used in any particular section, depending on which plan form most nearly duplicates the locus of elastic centers of the actual wing. Angular continuity is maintained between sections.

An orthogonal coordinate system is used in the derivation of the section equations. The origin of the coordinate system is set at the inboard end of the section with positive directions as shown in Fig. 2.

The oscillation of the swept wing is considered as a combination of bending motion in the z direction and a torsional motion in a plane normal to the centerline of the bar. No chordwise motion in the x direction is considered, since chordwise stiffness of an airplane wing is much greater than the spanwise bending or torsion.

There are six boundary conditions inherent in this type of motion; these involve shear, bending moment, slope, deflection, torque, and angle of twist. A matrix equation relating these boundary conditions at each end of a vibrating section is developed.

(*A*) *Analysis of Circular Arc Section*

Consider the concentrated mass detached from the bar, Fig. 3. Six relations are obtained from the free body of the concentrated mass. Assume that the mass is in harmonic motion so that the vertical displacement

$$h = \bar{h} \sin \omega t$$

Then if one considers only the inertial loads, the summation of forces in the vertical direction reduces to (see Fig. 3)

$${}_mV_n - \frac{W}{g}\frac{\partial^2 (\bar{h} \sin \omega t)}{\partial t^2} = {}_bV_n$$

or

$$ {}_bV_n = {}_mV_n + (W/g)h\omega^2 $$

Since

$$ h = z + e\beta $$

$$ {}_bV_n = {}_mV_n + (\omega^2/g)\,(Wz + We\beta) $$

or

$$ {}_bV_n = {}_mV_n + KWz + KS\beta \tag{1} $$

where

K = frequency factor for coupled motion, ω^2/g
S = static unbalance, We

Also, from the free body,

$$ {}_bM_n = {}_mM_n \tag{2} $$

$$ {}_bz_n' = {}_mz_n' \tag{3} $$

$$ {}_bz_n = {}_mz_n \tag{4} $$

$$ {}_b\beta_n = {}_m\beta_n \tag{5} $$

and

$$ {}_bT_n = {}_mT_n - (W/g)e\ddot{h} $$

By the same analysis as was used to obtain Eq. (1), this becomes

$$ {}_bT_n = {}_mT_n + KS({}_mz_n) + KI_\beta({}_m\beta_n) \tag{6} $$

where I_β = weight moment of inertia.

Eqs. (1) through (6) are represented in matrix form by the following equation:

$$ \begin{bmatrix} {}_bV_n \\ {}_bM_n \\ {}_bz_n' \\ {}_bz_n \\ {}_bT_n \\ {}_b\beta_n \end{bmatrix} = \begin{bmatrix} 1 & 0 & 0 & KW & 0 & KS \\ 0 & 1 & 0 & 0 & 0 & 0 \\ 0 & 0 & 1 & 0 & 0 & 0 \\ 0 & 0 & 0 & 1 & 0 & 0 \\ 0 & 0 & 0 & KS & 1 & KI_\beta \\ 0 & 0 & 0 & 0 & 0 & 1 \end{bmatrix} \begin{bmatrix} {}_mV_n \\ {}_mM_n \\ {}_mz_n' \\ {}_mz_n \\ {}_mT_n \\ {}_m\beta_n \end{bmatrix} \tag{7} $$

Next consider a circular arc bar portion of a wing. The subscript b has been omitted from Eqs. (8) through (33), because these equations are needed only in the derivation of Eq. (34).

The shear, bending moment, and torsional relations for the bar portion of the section are found from the free body of the bar, shown in Fig. 4. These relations are

$$ V_{n-1} = V_n \tag{8} $$

$$ M_{n-1} = V_nR\sin(\theta - \theta_1) + M_n\cos(\theta - \theta_1) - T_n\sin(\theta - \theta_1) \tag{9} $$

$$ T_{n-1} = V_nR[1 - \cos(\theta - \theta_1)] + M_n\sin(\theta - \theta_1) + T_n\cos(\theta - \theta_1) \tag{10} $$

The three remaining relationships necessary to relate the boundary conditions at one end of the bar to those at the other end are found from the geometry of the bar when it is deflected and twisted from its original position. The usual thin bar assumptions are made. For small deflections the deformed shape of the bar is determined by the displacement of the section centroid and the rotation about the bar centerline. Under these conditions, the deflection and twist are

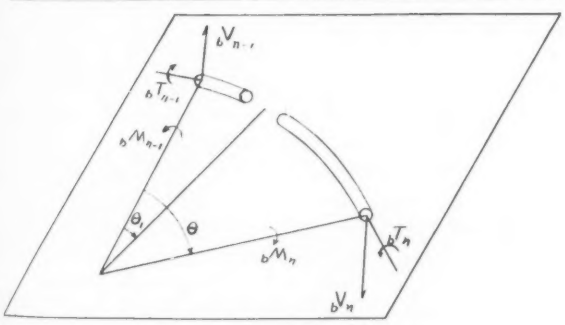

FIG. 4. Free body of bar.

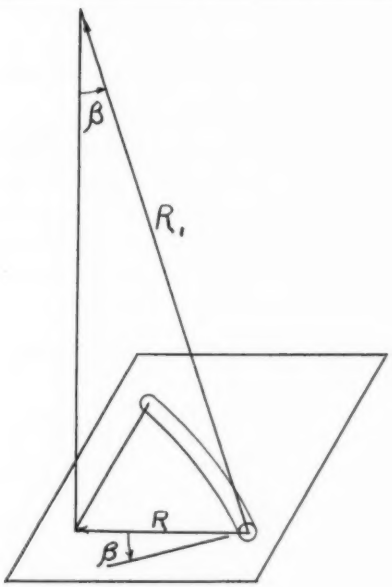

FIG. 5. Pure torsion.

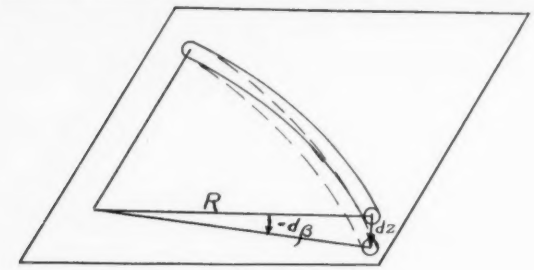

FIG. 6. Pure bending.

considered separately, and the final change in curvature and twist is obtained by adding the individual components.[12]

Consider the bar restrained in such a manner that only an angular displacement β is obtained. The curvature, after twist, as shown in Fig. 5, is

$$1/R_1 = -\sin \beta/R \backsimeq -\beta/R \tag{11}$$

and the change in angle of twist per unit length is

$$\phi = d\beta/ds \tag{12}$$

The bar is next considered restrained in such a manner that only a pure deflection is allowed. As previously stated, no motion in the chordwise plane is considered. From this geometric consideration, see Fig. 6, two more relations involving R_1 and ϕ are obtained.

$$1/R_1 = d^2z/ds^2 \tag{13}$$

$$\phi = -(1/R)\,(dz/ds) \tag{14}$$

since $-d\beta = dz/R = -\phi ds$.

Eqs. (8) through (14), together with the bar formulas,

$$EI(1/R_1) = M_{n-1} \tag{15}$$

$$GJ\phi = T_{n-1} \tag{16}$$

are sufficient to determine the relationships between the boundary conditions at each end of the curved bar.

The curvature for combined bending and torsion is obtained by adding the contributions of Eqs. (11) and (13).

$$1/R_1 = (d^2z/ds^2) - (\beta/R) \tag{17}$$

The angle of twist is given by the sum of Eqs. (12) and (14).

$$\phi = -[(1/R)\,(dz/ds)] + (d\beta/ds) \tag{18}$$

When the initial shape of the bar section is a circular arc, Eqs. (17) and (18) are written in terms of the central angle, $ds = R\,d\theta_1$. Then,

$$1/R_1 = (1/R^2)\,[(d^2z/d\theta_1^2) - R\beta] \tag{19}$$

$$\phi = (1/R^2)\,[-(dz/d\theta_1) + R\,(d\beta/d\theta_1)] \tag{20}$$

Substitution of Eqs. (8), (9), (10), and (20) into Eqs. (15) and (16) will yield

$$\frac{d^2z}{d\theta_1^2} - R\beta = \frac{R^2}{EI}\,[V_nR\sin(\theta - \theta_1) + M_n\cos(\theta - \theta_1) - T_n\sin(\theta - \theta_1)] \tag{21}$$

and

$$-\frac{dz}{d\theta_1} + R\frac{d\beta}{d\theta_1} = \frac{R^2}{GJ}\left\{V_nR[1 - \cos(\theta - \theta_1)] + M_n\sin(\theta - \theta_1) + T_n\cos(\theta - \theta_1)\right\} \tag{22}$$

Integration of Eq. (22) with respect to θ_1 and solving for $R\beta$ will give

$$R\beta = z + (R^2/GJ)\left\{V_nR[\theta_1 + \sin(\theta - \theta_1)] + M_n\cos(\theta - \theta_1) - T_n\sin(\theta - \theta_1)\right\} + C_1 \tag{23}$$

By substituting Eq. (23) into Eq. (21), the following differential equation is obtained:

$$(d^2z/d\theta_1^2) - z = V_nR[(A + B)\sin(\theta - \theta_1) + B\theta_1] + M_n(A + B)\cos(\theta - \theta_1) - T_n(A + B)\sin(\theta - \theta_1) + C_1 \tag{24}$$

where $A = R^2/EI$ and $B = R^2/GJ$.

The solution of Eq. (24) is effected by the operator method or variation of parameters and yields the following expression for z:

$$z = V_nR[-(1/2)\,(A + B)\sin(\theta - \theta_1) - B\theta_1] - (1/2)\,M_n(A + B)\cos(\theta - \theta_1) + (1/2)T_n(A + B)\sin(\theta - \theta_1) - C_1 + C_2\cosh\theta_1 + C_3\sinh\theta_1 \tag{25}$$

Replacing z of Eq. (23) with the value of z given by Eq. (25) and reducing, the value of $R\beta$ is

$$R\beta = -(1/2)V_nR(A - B)\sin(\theta - \theta_1) - (1/2)\,M_n(A - B)\cos(\theta - \theta_1) + (1/2)T_n \times (A - B)\sin(\theta - \theta_1) + C_2\cosh\theta_1 + C_3\sinh\theta_1 \tag{26}$$

The expression for z' is obtained by differentiation of Eq. (25) with respect to s. Since

$$dz/ds = (1/R)\,(dz/d\theta_1)$$

the expression for z' is as follows:

$$z' = V_n\left[\frac{1}{2}(A + B)\cos(\theta - \theta_1) - B\right] - M_n\left(\frac{A + B}{2R}\right)\sin(\theta - \theta_1) - T_n\left(\frac{A + B}{2R}\right) \times \cos(\theta - \theta_1) + \frac{C_2}{R}\sinh\theta_1 + \frac{C_3}{R}\cosh\theta_1 \tag{27}$$

The unknown constants C_1, C_2, and C_3 are evaluated in terms of the boundary conditions at the outboard end of the bar.

$$z' = z_n',\quad z = z_n,\quad \beta = \beta_n \quad (\text{when } \theta_1 = \theta) \tag{28}$$

When these conditions are imposed on Eqs. (25), (26), and (27), the following relations are obtained:

$$\left.\begin{aligned} z_n &= -V_nRB\theta - (1/2)M_n(A+B) - C_1 + C_2\cosh\theta + C_3\sinh\theta \\ Rz_n' &= (1/2)V_nR(A-B) - (1/2)T_n(A+B) + C_2\sinh\theta + C_3\cosh\theta \\ R\beta_n &= -(1/2)M_n(A-B) + C_2\cosh\theta + C_3\sinh\theta \end{aligned}\right\} \quad (29)$$

Solving these equations for C_1, C_2, and C_3 gives

$$\left.\begin{aligned} C_1 &= -V_nRB\theta - M_nB - z_n + \beta_nR \\ C_2 &= (1/2)V_nR(A-B)\sinh\theta + (1/2)M_n(A-B)\cosh\theta - z_n'R\sinh\theta - (1/2)T_n(A+B)\sinh\theta + \beta_nR\cosh\theta \\ C_3 &= -(1/2)V_nR(A-B)\cosh\theta - (1/2)M_n(A-B)\sinh\theta + z_n'R\cosh\theta + (1/2)T_n(A+B)\cosh\theta - \beta_nR\sinh\theta \end{aligned}\right\} \quad (30)$$

Substituting the values of the constants C_1, C_2, and C_3 of Eqs. (30) back into Eqs. (25), (26), and (27) and at the same time setting $\theta_1 = 0$, the following bar equations are obtained:

$$z_{n-1} = V_n\left[\frac{AR}{2}(\sinh\theta - \sin\theta) - \frac{BR}{2}(\sinh\theta + \sin\theta - 2\theta)\right] + M_n\left[\frac{A}{2}(\cosh\theta - \cos\theta) - \frac{B}{2}(\cosh\theta + \cos\theta - 2)\right] + z_n'(-R\sinh\theta) + z_n + T_n\left[-\frac{A}{2}(\sinh\theta - \sin\theta) - \frac{B}{2}(\sinh\theta - \sin\theta)\right] + \beta_n\left[R(\cosh\theta - 1)\right] \quad (31)$$

$$z_{n-1}' = V_n\left[-\frac{A}{2}(\cosh\theta - \cos\theta) + \frac{B}{2}(\cosh\theta + \cos\theta - 2)\right] + M_n\left[-\frac{A}{2R}(\sinh\theta + \sin\theta) + \frac{B}{2R}(\sinh\theta - \sin\theta)\right] + z_n'(\cosh\theta) + T_n\left[\frac{A}{2R}(\cosh\theta - \cos\theta) + \frac{B}{2R}(\cosh\theta - \cos\theta)\right] + \beta_n(-\sinh\theta) \quad (32)$$

and

$$\beta_{n-1} = V_n\left[\frac{A}{2}(\sinh\theta - \sin\theta) - \frac{B}{2}(\sinh\theta - \sin\theta)\right] + M_n\left[\frac{A}{2R}(\cosh\theta - \cos\theta) - \frac{B}{2R}(\cosh\theta - \cos\theta)\right] + z_n'(-\sinh\theta) + T_n\left[-\frac{A}{2R}(\sinh\theta - \sin\theta) - \frac{B}{2R}(\sinh\theta + \sin\theta)\right] + \beta_n(\cosh\theta) \quad (33)$$

The matrix equation [Eq. (34)], relating the boundary conditions at each end of the bar, is obtained by combining Eqs. (8), (9), (10), (31), (32), and (33).

The matrix equation relating the boundary conditions at each end of the section containing the concentrated mass and its inboard circular arc bar is obtained by replacing the right-hand column matrix of Eq. (34) with the right side of Eq. (7). This product is given by Eq. (35). See page 334 for Eqs. (34) and (35).

(*B*) *Reduction of Circular Arc Section to Straight Section*

The vibrating system, which has been selected to approximate the continuous structure of a swept wing, is represented by sections containing either the circular arc bar and a mass or a straight bar and a mass. Eq. (35) relates the various boundary conditions at the outboard end of the section to the boundary conditions at the inboard end.

The matrix equations relating the boundary conditions at the outboard end of a straight bar section to those conditions at the inboard end can be obtained by applying a limiting process to Eq. (35), the circular bar equation. Eq. (35) is first rewritten by replacing R with $R = L/\theta$, where L is the length of the section measured along the centerline of the bar. This will reduce the equation to a function of θ only. Passing to the limit, as $\theta \to 0$ ($R \to \infty$), the matrix equation of a circular arc bar section becomes the equation for a straight bar section. The six relationships thus derived agree with those used by Targoff[11] and Myklestad[9] for the determination of the vibration characteristics of a straight wing.

As an example of the limit procedure, consider the part of the matrix equation [Eq. (35)] which relates ${}_bz_{n-1}'$ with the boundary conditions at the outboard end of the section. Substitute $R = L/\theta$ and expand the equation to obtain the relation found at the top of page 335:

$$
\begin{bmatrix} b^{V}_{n-1} \\ b^{M}_{n-1} \\ b^{z'}_{n-1} \\ b^{z}_{n-1} \\ b^{T}_{n-1} \\ b\beta_{n-1} \end{bmatrix} = \left[\begin{array}{c|c|c|c|c|c} 1 & 0 & 0 & 0 & 0 & 0 \\ \hline R\sin\theta & \cos\theta & 0 & 0 & -\sin\theta & 0 \\ \hline \begin{matrix} -(A-B)\frac{\cosh\theta}{2} \\ +(A+B)\frac{\cos\theta}{2} \\ -B \end{matrix} & -\left(\frac{A-B}{R}\right)\frac{\sinh\theta}{2} & \cosh\theta & 0 & \left(\frac{A+B}{R}\right)\frac{\cosh\theta}{2} & -\sinh\theta \\ & -\left(\frac{A+B}{R}\right)\frac{\sin\theta}{2} & & & -\left(\frac{A+B}{R}\right)\frac{\cos\theta}{2} & \\ \hline \begin{matrix} R(A-B)\frac{\sinh\theta}{2} \\ -R(A+B)\frac{\sin\theta}{2} \\ +RB\theta \end{matrix} & \begin{matrix} (A-B)\frac{\cosh\theta}{2} \\ -(A+B)\frac{\cos\theta}{2} \\ +B \end{matrix} & -R\sinh\theta & 1 & \begin{matrix} -(A+B)\frac{\sinh\theta}{2} \\ +(A+B)\frac{\sin\theta}{2} \end{matrix} & R(\cosh\theta-1) \\ \hline R(1-\cos\theta) & \sin\theta & 0 & 0 & \cos\theta & 0 \\ \hline \begin{matrix} (A-B)\frac{\sinh\theta}{2} \\ -(A-B)\frac{\sin\theta}{2} \end{matrix} & \begin{matrix} \left(\frac{A-B}{R}\right)\frac{\cosh\theta}{2} \\ -\left(\frac{A-B}{R}\right)\frac{\cos\theta}{2} \end{matrix} & -\sinh\theta & 0 & \begin{matrix} -\left(\frac{A+B}{R}\right)\frac{\sinh\theta}{2} \\ +\left(\frac{A-B}{R}\right)\frac{\sin\theta}{2} \end{matrix} & \cosh\theta \end{array}\right] \begin{bmatrix} b^{V}_{n} \\ b^{M}_{n} \\ b^{z'}_{n} \\ b^{z}_{n} \\ b^{T}_{n} \\ b\beta_{n} \end{bmatrix} \tag{34}
$$

$$
\begin{bmatrix} b^{V}_{n-1} \\ b^{M}_{n-1} \\ b^{z'}_{n-1} \\ b^{z}_{n-1} \\ b^{T}_{n-1} \\ b\beta_{n-1} \end{bmatrix} = \left[\begin{array}{c|c|c|c|c|c} 1 & 0 & 0 & K\mathrm{W} & 0 & K\mathrm{S} \\ \hline R\sin\theta & \cos\theta & 0 & \begin{matrix} K(\mathrm{W}R\sin\theta \\ -S\sin\theta) \end{matrix} & -\sin\theta & \begin{matrix} K(SR\sin\theta \\ -I_{\beta}\sin\theta) \end{matrix} \\ \hline \begin{matrix} -(A-B)\frac{\cosh\theta}{2} \\ +(A+B)\frac{\cos\theta}{2} \\ -B \end{matrix} & \begin{matrix} -\left(\frac{A-B}{R}\right)\frac{\sinh\theta}{2} \\ -\left(\frac{A+B}{R}\right)\frac{\sin\theta}{2} \end{matrix} & \cosh\theta & \begin{matrix} K\Big[W\Big\{-(A-B)\frac{\cosh\theta}{2} \\ +(A+B)\frac{\cos\theta}{2} \\ -B\Big\} \\ +S\Big\{\left(\frac{A+B}{R}\right)\frac{\cosh\theta}{2} \\ -\left(\frac{A+B}{R}\right)\frac{\cos\theta}{2}\Big\}\Big] \end{matrix} & \begin{matrix} \left(\frac{A+B}{R}\right)\frac{\cosh\theta}{2} \\ -\left(\frac{A+B}{R}\right)\frac{\cos\theta}{2} \end{matrix} & \begin{matrix} K\Big[S\Big\{-(A-B)\frac{\cosh\theta}{2} \\ +(A+B)\frac{\cos\theta}{2} \\ -B\Big\} \\ +I_{\beta}\Big\{\left(\frac{A+B}{R}\right)\frac{\cosh\theta}{2} \\ -\left(\frac{A+B}{R}\right)\frac{\cos\theta}{2}\Big\}\Big] \\ -\sinh\theta \end{matrix} \\ \hline \begin{matrix} R(A-B)\frac{\sinh\theta}{2} \\ -R(A+B)\frac{\sin\theta}{2} \\ +RB\theta \end{matrix} & \begin{matrix} (A-B)\frac{\cosh\theta}{2} \\ -(A+B)\frac{\cos\theta}{2} \\ +B \end{matrix} & -R\sinh\theta & \begin{matrix} K\Big[W\Big\{R(A-B)\frac{\sinh\theta}{2} \\ -R(A+B)\frac{\sin\theta}{2} \\ +RB\theta\Big\} \\ +S\Big\{-(A+B)\frac{\sinh\theta}{2} \\ +(A+B)\frac{\sin\theta}{2}\Big\}\Big] \\ +1 \end{matrix} & \begin{matrix} -(A+B)\frac{\sinh\theta}{2} \\ +(A+B)\frac{\sin\theta}{2} \end{matrix} & \begin{matrix} K\Big[S\Big\{R(A-B)\frac{\sinh\theta}{2} \\ -R(A+B)\frac{\sin\theta}{2} \\ +RB\theta\Big\} \\ +I_{\beta}\Big\{-(A+B)\frac{\sinh\theta}{2} \\ +(A+B)\frac{\sin\theta}{2}\Big\} \\ +R(\cosh\theta-1) \end{matrix} \\ \hline \begin{matrix} R(1-\cos\theta) \\ \\ \end{matrix} & \sin\theta & 0 & \begin{matrix} K\{WR(1-\cos\theta) \\ +S\cos\theta\} \end{matrix} & \cos\theta & \begin{matrix} K\{SR(1-\cos\theta) \\ +I_{\beta}\cos\theta\} \end{matrix} \\ \hline \begin{matrix} (A-B)\frac{\sinh\theta}{2} \\ -(A-B)\frac{\sin\theta}{2} \end{matrix} & \begin{matrix} \left(\frac{A-B}{R}\right)\frac{\cosh\theta}{2} \\ -\left(\frac{A-B}{R}\right)\frac{\cos\theta}{2} \end{matrix} & -\sinh\theta & \begin{matrix} K\Big[W\Big\{(A-B)\frac{\sinh\theta}{2} \\ -(A-B)\frac{\sin\theta}{2}\Big\} \\ +S\Big\{-\left(\frac{A+B}{R}\right)\frac{\sinh\theta}{2} \\ +\left(\frac{A-B}{R}\right)\frac{\sin\theta}{2}\Big\}\Big] \end{matrix} & \begin{matrix} -\left(\frac{A+B}{R}\right)\frac{\sinh\theta}{2} \\ +\left(\frac{A-B}{R}\right)\frac{\sin\theta}{2} \end{matrix} & \begin{matrix} K\Big[S\Big\{(A-B)\frac{\sinh\theta}{2} \\ -(A-B)\frac{\sin\theta}{2}\Big\} \\ +I_{\beta}\Big\{-\left(\frac{A+B}{R}\right)\frac{\sinh\theta}{2} \\ +\left(\frac{A-B}{R}\right)\frac{\sin\theta}{2}\Big\}\Big] \\ +\cosh\theta \end{matrix} \end{array}\right] \begin{bmatrix} m^{V}_{n} \\ m^{M}_{n} \\ m^{z'}_{n} \\ m^{z}_{n} \\ m^{T}_{n} \\ m\beta_{n} \end{bmatrix} \tag{35}
$$

$$
\begin{aligned}
{}_bz_{n-1}' = {}_mV_n\left[-\frac{L^2}{EI}\left(\frac{\cosh\theta-\cos\theta}{2\theta^2}\right)+\frac{L^2}{GJ}\left(\frac{\cosh\theta+\cos\theta-2}{2\theta^2}\right)\right]+\\
{}_mM_n\left[-\frac{L}{EI}\left(\frac{\sinh\theta+\sin\theta}{2\theta}\right)+\frac{L}{GJ}\left(\frac{\sinh\theta-\sin\theta}{2\theta}\right)\right]+{}_mz_n'(\cosh\theta)+\\
{}_mz_n\left\{KW\left[-\frac{L^2}{EI}\left(\frac{\cosh\theta-\cos\theta}{2\theta^2}\right)+\frac{L^2}{GJ}\left(\frac{\cosh\theta+\cos\theta-2}{2\theta^2}\right)\right]+\right.\\
\left.KS\left[\frac{L}{EI}\left(\frac{\cosh\theta-\cos\theta}{2\theta}\right)+\frac{L}{GJ}\left(\frac{\cosh\theta-\cos\theta}{2\theta}\right)\right]\right\}+{}_mT_n\left[\frac{L}{EI}\left(\frac{\cosh\theta-\cos\theta}{2\theta}\right)+\right.\\
\left.\frac{L}{GJ}\left(\frac{\cosh\theta-\cos\theta}{2\theta}\right)\right]+{}_m\beta_n\left\{KS\left[-\frac{L^2}{EI}\left(\frac{\cosh\theta-\cos\theta}{2\theta^2}\right)+\frac{L^2}{GJ}\left(\frac{\cosh\theta+\cos\theta-2}{2\theta^2}\right)\right]+\right.\\
\left.K\left[\frac{L}{EI}\left(\frac{\cosh\theta-\cos\theta}{2\theta}\right)-\frac{L}{GJ}\left(\frac{\cosh\theta-\cos\theta}{2\theta}\right)\right]-\sinh\theta\right\} \qquad (36)
\end{aligned}
$$

The following limits are necessary:

$$
\left.\begin{gathered}
\lim_{\theta\to0}\frac{\cosh\theta-\cos\theta}{2\theta^2}=\frac{1}{2},\quad \lim_{\theta\to0}\frac{\cosh\theta+\cos\theta-2}{2\theta^2}=0,\quad \lim_{\theta\to0}\frac{\sinh\theta+\sin\theta}{2\theta}=1,\\
\lim_{\theta\to0}\frac{\sinh\theta-\sin\theta}{2\theta}=0,\quad \lim_{\theta\to0}[(\cosh\theta-\cos\theta)/2\theta]=0
\end{gathered}\right\} \qquad (37)
$$

Substituting the values obtained for the limits in Eq. (37) into Eq. (36) yields

$$
z_{n-1}' = -\frac{L^2}{2EI}V_n-\frac{L}{EI}M_n+z_n'-\frac{KWL^2}{2EI}z_n-\frac{KSL^2}{2EI}\beta_n \qquad (38)
$$

The same procedure is used on the remaining portions of Eq. (35). Thus, the straight bar section matrix is

$$
\begin{bmatrix} {}_bV_{n-1} \\ {}_bM_{n-1} \\ {}_bz_{n-1}' \\ {}_bz_{n-1} \\ {}_bT_{n-1} \\ {}_b\beta_{n-1} \end{bmatrix} = \left[\begin{array}{c|c|c|c|c|c} 1 & 0 & 0 & KW & 0 & KS \\ \hline L & 1 & 0 & KWL & 0 & KSL \\ \hline -\frac{L^2}{2EI} & -\frac{L}{EI} & 1 & -\frac{KWL^2}{2EI} & 0 & -\frac{KSL^2}{2EI} \\ \hline \frac{L^3}{6EI} & \frac{L^2}{2EI} & -L & \left(1+\frac{KWL^3}{6EI}\right) & 0 & \frac{KSL^3}{6EI} \\ \hline 0 & 0 & 0 & KS & 1 & KI_\beta \\ \hline 0 & 0 & 0 & -\frac{KSL}{GJ} & -\frac{L}{GJ} & \left(1-\frac{KI_\beta L}{GJ}\right) \end{array}\right] \begin{bmatrix} {}_mV_n \\ {}_mM_n \\ {}_mz_n' \\ {}_mz_n \\ {}_mT_n \\ {}_m\beta_n \end{bmatrix} \qquad (39)
$$

To handle an actual concentrated mass, such as tip tanks, bomb racks, and nacelles, Eq. (39) is used with $L = 0$.

Eq. (35) or (39), depending on whether the section contains a circular arc or straight bar, relates the boundary conditions at the ends of a section. Next, a single matrix equation for the composite wing, made up of all the sections, will be developed to relate each boundary condition at the wing center span to the boundary conditions at the tip. The composite wing is the replacement wing, composed of a finite number of sections, used to approximate the actual wing when the vibration analysis is made.

(C) *The Composite Wing*

Each section is assigned a section number starting with one (1) at the center of the wing span and continuing to n at the tip. The matrix equation, either Eq.

(35) or (39), which is used for the tip section is written symbolically as

$$[C_{n-1}] = [D_n]\,[C_n] \tag{40}$$

The equation form of the station just inboard of the tip is

$$[C_{n-2}] = [D_{n-1}]\,[C_{n-1}] \tag{41}$$

Eq. (40) is set into Eq. (41) to give

$$[C_{n-2}] = [D_{n-1}]\,[D_n]\,[C_n] \tag{42}$$

After n such substitutions,

$$[C_0] = [D_1]\,[D_2] \ldots [D_n]\,[C_n] \tag{43}$$

A trial value of the frequency factor K is then chosen and is substituted into the matrix equations for the various sections {noted symbolically as $[D_1]$ to $[D_n]$} in Eq. (43). The indicated matrix multiplication $[D_1][D_2] \ldots [D_n]$ is carried out, and the resulting matrix equation is reduced to its set of six linear equations. Each equation relates a shear, bending moment, slope, deflection, torque, or angle of twist at the center of the wing span to the shear, bending moment, slope, deflection, torque, and angle of twist at the tip.

The boundary conditions at the wing tip are

$$V_n = M_n = T_n = 0 \tag{44}$$

Additional boundary conditions for symmetric vibrations are

$$V_0 = z_0' = T_0 = 0 \tag{45}$$

and for antisymmetric vibrations

$$M_0 = z_0 = \beta_0 = 0 \tag{46}$$

Set $z_n = 1$, and for the symmetric case, for any particular choice of K, solve for z_n' and β_n from the equations $z_0' = 0$ and $T_0 = 0$. Substitute the values found for z_n' and β_n into the V_0 equation. The shear thus obtained is plotted against the frequency, and, wherever the resulting curve crosses the zero shear axis, a natural symmetric frequency occurs. For the antisymmetric case, set $z_n = 1$, $\beta_0 = z_0 = 0$ and solve for M_0. Plot the values obtained for the bending moment against the frequency, and, wherever the resulting curve crosses the zero bending moment axis, a natural antisymmetric frequency occurs.

Using this procedure, z_n is always set equal to 1. If, for a particular value of K, z_n is actually equal to 0 for the symmetric or antisymmetric mode, the value of V_0 or M_0 will be driven to ∞. Thus, for two values of K in this neighborhood, the curve may be drawn to cross the axis when actually an infinite discontinuity should occur. A little experience with curve shapes will indicate when such a possibility exists or an alternate procedure can be used.

The alternate procedure is based on the existence theorem for the solution of a set of homogeneous linear equations. Set the tip boundary conditions (44) into Eqs. (45) and (46). Then for each case calculate the value of the determinant of coefficients, and plot these values against the frequency. Wherever the resulting curve crosses the zero determinant value axis, a natural frequency occurs.

Illustrated Example

A preliminary sectioning of the wing is made. The total weight and center of gravity of each of these preliminary sections are determined. Also, the weight moment of inertia with respect to the elastic axis is determined for each of the preliminary sections. One-half the fuselage properties is assigned to a zero length section at the fuselage centerline and labeled Section 1. The total weight and moment of inertia of the second preliminary section are then considered concentrated at the spanwise location of the center of gravity of that section. The same thing is done in the remaining preliminary sections. The actual Section 2 used in the calculation is composed of the spanwise structure from the fuselage centerline to the location of the first outboard center of gravity. This process is continued to the tip, and the actual sections then used run from one mass just through the next outboard mass.

The average bending area moment of inertia and torsional polar moment of inertia of the actual sections used are assigned to the weightless bars in the actual sections. The static unbalance S for each section is determined by the weight W and the distance e from the center of gravity to the assumed elastic axis. The radius of curvature R and the central angle θ of any circular arc bar section is determined by the plan form of the circular arc chosen to approximate the locus of elastic centers of the section. The length L of any straight bar section is the distance along the elastic axis between the spanwise location of the mass of the section and the next inboard mass, measured positive from root to tip. Numerical values of the section properties of a typical wing are listed in Table 1.

The matrix equations for Wing Sections 2, 3, and 4 are obtained by substituting the properties listed in Table 1 into Eq. (35). The matrix equation for the zero length section (Section 1) and the equations for the straight bar sections (Sections 5, 6, 7, and 8) are obtained by using Eq. (39). In order to get a more uniform range of numerical values, the following substitutions are made:

$$\left.\begin{aligned} z &= \bar{z}(10^{-6}) \\ z' &= \bar{z}'(10^{-6}) \\ \beta &= \bar{\beta}(10^{-6}) \end{aligned}\right\} \tag{47}$$

The matrix equations for Sections 3 and 8, for $K = 20$, are shown in Table 2.

When the matrix equation for each section has been evaluated, a trial value for the frequency factor K is substituted into the matrix equation for each section.

TABLE 1
Basic Wing Data

Section	W (Lbs.)	I (In.^{4})	J (In.^{4})	L (In.)	e (In.)
1	5,226	776.7	1,650	0	15
2	503	558.3	1,342	..	..
3	413	475.7	1,056	..	..
4	350	378.7	809	..	..
5	112	208.7	517	37	0
6	68	97.1	198	37	0
7	68	58.3	99	37	0
8	52	34.0	44	41	8

$E = 10.3 \times 10^6$ lb./in.^{2}
$G = 3.5 \times 10^6$ lb./in.^{2}

Section	S (Lb.-In.)	I_β (Lb.-In.^{2})	R (In.)	θ (Rad.)
1	78,390	64,112,000	...	...
2	2,012	110,336	110	0.28
3	4,543	130,808	175	0.14
4	−350	71,400	175	0.21
5	0	40,000	...	...
6	0	23,800	...	...
7	0	18,240	...	...
8	416	7,740	...	...

TABLE 2

Matrix Equation for Section 3, $K = 20$

$$\begin{bmatrix} V_2 \\ M_2 \\ \bar{z}_2' \\ \bar{z}_2 \\ T_2 \\ \bar{\beta}_2 \end{bmatrix} = \left[\begin{array}{cccccc} 1 & 0 & 0 & 0.008260 & 0 & 0.090860 \\ 24.4195 & 0.990220 & 0 & 0.189026 & -0.13954 & 1.85370 \\ -0.061085 & -0.004978 & 1.00982 & -0.000431 & 0.000814 & -0.14388 \\ 0.503171 & 0.061085 & -24.581 & 1.00355 & -0.00669 & 1.74672 \\ 1.71150 & 0.139540 & 0 & 0.104108 & 0.99022 & 2.74608 \\ -0.000937 & -0.000114 & -0.14046 & -0.000612 & -0.00665 & 0.992348 \end{array}\right] \begin{bmatrix} V_3 \\ M_3 \\ \bar{z}_3' \\ \bar{z}_3 \\ T_3 \\ \bar{\beta}_3 \end{bmatrix}$$

Matrix Equation for Section 8, $K = 20$

$$\begin{bmatrix} V_7 \\ M_7 \\ \bar{z}_7' \\ \bar{z}_7 \\ T_7 \\ \bar{\beta}_7 \end{bmatrix} = \left[\begin{array}{cccccc} 1 & 0 & 0 & 0.001040 & 0 & 0.008320 \\ 41 & 1 & 0 & 0.042640 & 0 & 0.341120 \\ -2.40148 & -0.117141 & 1 & -0.002498 & 0 & -0.01998 \\ 32.8202 & 2.40148 & -41 & 1.03414 & 0 & 0.273060 \\ 0 & 0 & 0 & 0.008320 & 1 & 0.154800 \\ 0 & 0 & 0 & -0.002216 & -0.26625 & 0.958780 \end{array}\right] \begin{bmatrix} V_8 \\ M_8 \\ \bar{z}_8' \\ \bar{z}_8 \\ T_8 \\ \bar{\beta}_8 \end{bmatrix}$$

TABLE 3
Wing Matrix for $K = 20$

$$\begin{bmatrix} V_0 \\ M_0 \\ \bar{z}_0' \\ \bar{z}_0 \\ T_0 \\ \bar{\beta}_0 \end{bmatrix} = \left[\begin{array}{cccccc} \cdots & \cdots & -49.4739 & 0.716660 & \cdots & 6.46987 \\ \cdots & \cdots & -342.682 & 5.11064 & \cdots & 22.2424 \\ \cdots & \cdots & 4.27681 & -0.064939 & \cdots & -0.78055 \\ \cdots & \cdots & -399.423 & 5.84252 & \cdots & 42.9245 \\ \cdots & \cdots & -1,695.08 & 20.9030 & \cdots & 1,261.78 \\ \cdots & \cdots & -0.728831 & 0.007562 & \cdots & 0.919914 \end{array}\right] \begin{bmatrix} V_8 \\ M_8 \\ \bar{z}_8' \\ \bar{z}_8 \\ T_8 \\ \bar{\beta}_8 \end{bmatrix}$$

Then the matrix of Station 8 is premultiplied by the matrix of Station 7. This product is premultiplied by the matrix of Eq. (6), and the process is continued until the matrix for the entire wing semispan has been calculated. In this manner each boundary condition at the center of the wing span is related to the boundary conditions at the tip. The first, second, and fifth columns of the section products are not calculated, since $V_8 = M_8 = T_8 = 0$ (boundary conditions at the tip). Table 3 shows the matrix of the wing for $K = 20$.

The matrix equation for the wing is then reduced to a set of six equations. The three equations used to calculate the unbalance for the symmetric case are

$$V_0 = -49.4739\bar{z}_8' + 0.71666\bar{z}_8 + 6.46987\bar{\beta}_8$$
$$\bar{z}_0' = +4.27681\bar{z}_8' - 0.064939\bar{z}_8 - 0.780549\bar{\beta}_8$$
$$T_0 = -1{,}695.08\bar{z}_8' + 20.9030\bar{z}_8 + 1{,}261.78\bar{\beta}_8$$

Set $\bar{z}_8 = 1$, $\bar{z}_0' = T_0 = 0$ and solve for $\bar{z}_8'$ and $\bar{\beta}_8$. Substitute these values into the V_0 equation and find $V_0 = -0.047566$. Had $V_0 = 0$, the value $K = 20$ would have been the frequency factor of one of the natural

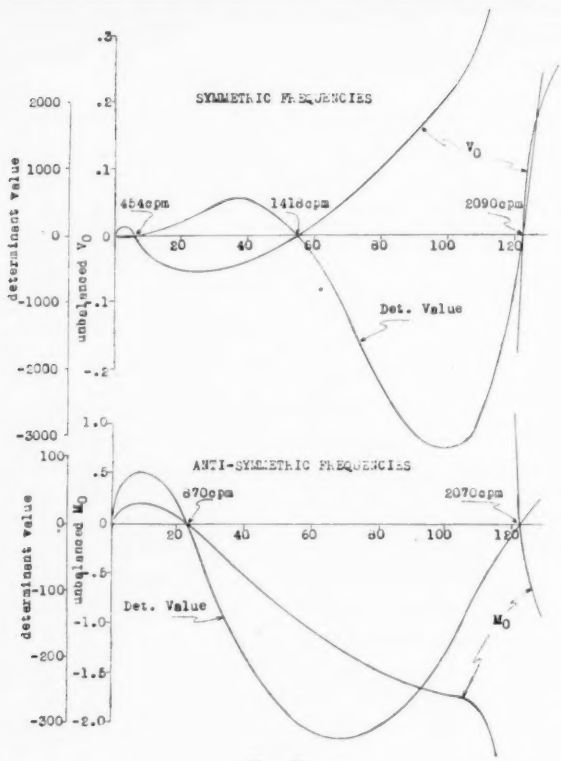

FIG. 7.

symmetric frequencies of coupled wing vibration. Since $V_0 \neq 0$ for $K = 20$, more values of K must be chosen and the unbalance graphed as shown on Fig. 7. The natural symmetric frequencies occur where $V_0 = 0$.

The conditions used to calculate the unbalance for the antisymmetric case for $K = 20$ are

$$M_0 = -342.682\bar{z}_8' + 5.11064\bar{z}_8 + 22.2424\bar{\beta}_8$$
$$\bar{z}_0 = -399.423\bar{z}_8' + 5.84252\bar{z}_8 + 42.9245\bar{\beta}_8$$
$$\bar{\beta}_0 = -0.728831\bar{z}_8' + 0.007562\bar{z}_8 + 0.919914\bar{\beta}_8$$

Set $\bar{z}_8 = 1$, $\bar{z}_0 = \bar{\beta}_0 = 0$ and solve for $\bar{z}_8'$ and $\bar{\beta}_8$. Substitute these values into the M_0 equation and find $M_0 = 0.044425$. Plot the unbalanced M_0 against the frequency factor K as on Fig. 7.

The determination of the unbalanced V_0 and M_0 for $K = 20$ illustrates the procedure used for any particular choice of K. No natural frequency was found for $K = 20$, since the boundary conditions were not satisfied. Therefore, more trial frequencies must be tried in order to locate the natural frequencies. Plotting the values of the unbalanced V_0 and M_0 as soon as they are obtained will aid in making more intelligent choices of future trial frequency factors. Fig. 7 shows that $V_0 = 0$ at approximately $K = 5.85$, 57, and 124 and that $M_0 = 0$ at approximately $K = 21.5$ and 122. Therefore, the symmetric natural frequencies occur at nearly 454, 1,418, and 2,090 cycles per min. and the antisymmetric frequencies occur at nearly 870 and 2,070 cycles per min. By successive choices of K, the frequencies can be determined to any desired degree of accuracy. The deflection pattern or any of the other four properties can be determined directly from their equations.

The values of the determinant of coefficients, described as an alternate procedure to determine the natural frequencies, are also plotted on Fig. 7.

REFERENCES

[1] Beskin, L., and Rosenburg, R. M., *Higher Modes of Vibration by the Method of Sweeping*, Journal of the Aeronautical Sciences, Vol. 13, No. 11, pp. 597–604, November, 1946.

[2] Boukidis, N. A., and Ruggiero, R. J., *An Iterative Method for Determining Dynamic Deflections and Frequencies*, Journal of the Aeronautical Sciences, Vol. 11, No. 4, pp. 319–328, October, 1944.

[3] Den Hartog, J. P., *Mechanical Vibrations;* McGraw-Hill Book Company, Inc., New York, 1940.

[4] Duncan, W. J., and Collar, A. R., *A Method for the Solution of Oscillation Problems by Matrices*, The London, Edinburgh, and Dublin Philosophical Magazine and Journal of Science, Series 7, Vol. 17, pp. 866–909, May, 1934.

[5] Fettis, H. E., *The Calculation of Coupled Modes of Vibration by the Stodola Method*, Journal of the Aeronautical Sciences, Vol. 16, No. 5, pp. 259–271, May, 1949.

[6] Frazer, R. A., Duncan, W. J., and Collar, A. R., *Elementary Matrices*, pp. 140–145; The MacMillan Company, New York, 1947.

[7] Houbolt, J. C., and Anderson, R. A., *Calculation of Uncoupled Modes and Frequencies in Bending and Torsion of Nonuniform Beams*, N.A.C.A. T.N. No. 1522, pp. 1–75, February, 1948.

[8] Levy, Sam, *Computation of Influence Coefficients for Aircraft Structures with Discontinuities and Sweepback*, Journal of the Aeronautical Sciences, Vol. 14, No. 10, pp. 547–560, October, 1947.

[9] Myklestad, N. O., *A New Method of Calculating Natural Modes of Uncoupled Bending Vibration of Airplane Wings and Other Types of Beams*, Journal of the Aeronautical Sciences, Vol. 11, No. 2, p. 153, April, 1944.

[10] Myklestad, N. O., *Vibration Analysis;* McGraw-Hill Book Company, Inc., New York, 1944.

[11] Targoff, W. P., *The Associated Matrices of Bending and Coupled Bending—Torsion Vibrations*, Journal of the Aeronautical Sciences, Vol. 14, No. 10, pp. 579–582, October, 1947.

[12] Timoshenko, S., *Strength of Materials*, Part II, Chapt. II, D. Van Nostrand Company, Inc., New York, 1930.

[13] von Kármán, Th., and Biot, M. A., *Mathematical Methods in Engineering*, McGraw-Hill Book Company, Inc., New York, 1940.

[14] Zahorski, A. T., *Free Vibrations of Sweptback Wings*, Journal of the Aeronautical Sciences, Vol. 14, No. 12, pp. 683–692, December, 1947.

Analysis of the Elastic and Plastic Stability of Sandwich Plates by the Method of Split Rigidities—I*

P. P. BIJLAARD†
Cornell University

SUMMARY

The author gives a detailed but simple derivation of his formula of the critical thrust for antisymmetrical buckling of sandwich plates

$$P_{cr} = P_0 + (P_1^{-1} + P_2^{-1})^{-1}$$

in which P_0 is the joint critical thrust of the single faces (Case 0), P_1 is the critical thrust without taking account of the shear deformation of the core (Case 1), and P_2 obtains if only shear deformations of the core would occur (Case 2). In computing P_1 and P_2, the flexural rigidity of the faces is not taken into account.

The method is applied to twelve different cases of loading and boundary conditions, for which the reduction coefficients for buckling in the plastic domain are also given and presented in graphs. A detailed explanation is included showing how the resulting formulas must be used to find the critical load P_{cr}. The critical load P_{crw} for wrinkling of the faces is also considered.

INTRODUCTION

THE RIGOROUS DETERMINATION of buckling loads of sandwich plates is extremely difficult because of the involved interaction of the core and the face plates. An approximate solution of satisfactory accuracy can be obtained by subdividing the complex interaction into its component parts and computing for each of them their individual critical loads. An interaction formula that combines these individual critical loads then gives the buckling load of the assembly.

The basic principle of this approach is first illustrated on a simple example. A simply supported homogeneous bar (Fig. 1a) buckles in a half sine wave, whereby in the elastic domain in any cross section the internal moment M_i is equal to the external moment $M_e = P_E w$, in which P_E is the Euler load and w is the deflection of the bar at the cross section involved. The internal moment M_i depends only on the curvature of the bar, so that with bending in a half sine wave, as it does with buckling, the inner moment will always be equal to $P_E w$, independent of the fact whether the bar is subjected to an axial force or not; hence,

$$M_i = P_E w \tag{1}$$

As a simple application of this conclusion, the resulting deflection w of a bar, with an initial inelastic deflection w_i, after application of an axial load P, will be calculated (Fig. 1b). Assuming the initial deflection w_i as a half sine wave, the thrust P will cause an excess deflection w_e. Since, before P was applied, the internal moment was zero, the internal moment is caused by the deflection w_e alone. If w_e also follows a half sine wave, it will cause an internal moment $M_i = P_E w_e$, which likewise varies as a half sine wave. The external moment

$$M_e = P(w_i + w_e) = Pw$$

also will vary according to a half sine wave, so that at any point equilibrium exists if[1]

$$M_i = M_e$$

or

$$P_E w_e = Pw \tag{2}$$

or

$$w = (P_E/P)w_e = (P_E/P)\,(w - w_i)$$

or

$$w = \{(P_E/P)/[(P_E/P) - 1]\}w_i \tag{3}$$

DERIVATION OF THE GENERAL EQUATION FOR THE CRITICAL THRUST OF SANDWICH PLATES

The same principle is now applied to the computation of the critical thrust of sandwich plates, consisting for example of metal faces and a core of light material of small rigidity, of which Fig. 2 gives a cross section. First, the cylindrical buckling of a plate with free unloaded edges is considered (Fig. 3).

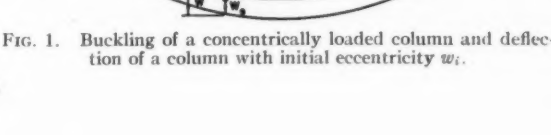

FIG. 1. Buckling of a concentrically loaded column and deflection of a column with initial eccentricity w_i.

Presented at the Structures Session, Eighteenth Annual Meeting, I.A.S., New York, January 23–26, 1950. Revised and received December 15, 1950.

* On request of the Editor, the author split his original paper in two parts, of which this first part gives the derivation of the general formula and the necessary information for the structural analyst to use it. The second part will contain those theoretical derivations that are not available elsewhere.

† Associate Professor.

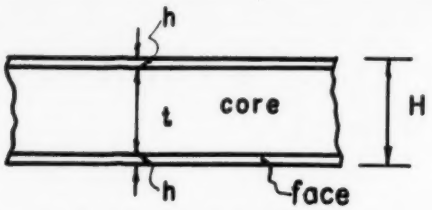

FIG. 2. Cross section of sandwich plate.

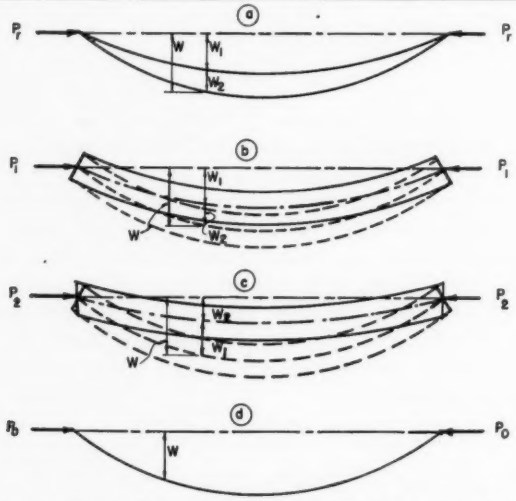

FIG. 3. Comparing external and internal moments for a sandwich column.

With buckling of homogeneous plates, only deformation by bending needs to be taken into account. With sandwich plates, however, the modulus of rigidity of the core is relatively so small that deformations by shear in the core must also be taken into account. The shear deformation of the faces may be neglected, since its effect is negligible with respect to that of the shear in the core. Moreover, it follows from a more exact calculation[2,3] that the strains of the core in a direction perpendicular to the middle plane may be neglected in practical cases of plate buckling (half wave length-thickness ratio larger than, say, 5). This does not apply, however, to wrinkling of the faces, which will be considered later.

The rigidity of the structure is now split into two parts in such a way that the following two cases are considered: In *Case 1*, the sandwich plate has its actual bending rigidity, but the core is assumed to be infinitely rigid against shear. In *Case 2*, the core is assumed to have its actual shearing rigidity, but the sandwich plate is assumed to be infinitely rigid against bending. As, however, in the latter case, the shear deformation of the core would not be possible if the proper rigidity of the faces, being that against bending with respect to their proper middle plane, also would be infinite, this proper bending rigidity of the faces is assumed to be zero, so that the deformations according to Cases 1 and 2 may proceed independently of each other. The effect of the bending rigidity of the faces is taken into account separately afterward in *Case 0*. The critical loads per unit width for Cases 0, 1, and 2 are denoted by P_0, P_1, and P_2, respectively.

Accordingly, first a reduced sandwich plate—i.e., with faces of zero proper rigidity—is considered. If it buckles, its total deflection w will consist of a deflection w_1 from deformation according to Case 1 and a deflection w_2 from Case 2 (Fig. 3a). Its reduced load P_r will be smaller than the real critical load P_{cr} of the complete sandwich.

Now it is assumed that only a deformation from Case 1 occurs, in which case the critical load will be P_1 (Fig. 3b). Since only a deflection w_1 occurs, the condition that the internal and external moments must be equal leads to

$$M_i = M_e$$

or

$$M_i = P_1 w_1 \tag{4}$$

according to Eq. (1).

Assume, subsequently, that, while the internal moment and shear remain the same, the rigidity of the core decreases from infinite to its real value. Consequently, the core is now deformed by the shearing stresses. This will increase the deflection by an amount w_2 (dotted in Fig. 3b), so that it acquires its final value $w = w_1 + w_2$. Since the internal moment remains constant and thus equals $P_1 w_1$, according to Eq. (4), the compressive force required to maintain the equilibrium will decrease now to its reduced value P_r. It has to satisfy the condition of equality of internal and external moments

$$M_i = M_e$$

or

$$P_1 w_1 = P_r w \tag{5}$$

yielding

$$w_1 = (P_r/P_1)\, w \tag{6}$$

If the deflections w_1 and w_2 and, hence, w_1 and w have the same form, Eqs. (5) and (6) will be valid for any point of the plate, so that indeed at any point the equilibrium is satisfied. Since in any section the shear then will be proportional to P and w, according to Eq. (5) the shear remained constant during the extra deflection w_2. Comparing Eqs. (2) and (5), it is clear that the deflection w_2 here plays the same role as the initial deflection w_i in case of the bar, Fig. 1, since both w_2 and w_i increase the external but not the internal moment.

It is next assumed that only a deformation according to Case 2 occurs (Fig. 3c) and, hence, that the faces are infinitely rigid against tension or compression and that only a shear deformation of the core takes place.

Since the critical thrust is P_2, it follows from $M_i = M_e$ that

$$M_i = P_2 w_2 \tag{7}$$

Now let, with constant internal moment and shear, the rigidity of the faces decrease to its actual value, by which the deflection increases by an amount w_1 (dotted in Fig. 3c). In a similar way, it follows then from $M_i = M_e$ that

$$P_2 w_2 = P_r w \tag{8}$$

yielding

$$w_2 = (P_r/P_2)\, w \tag{9}$$

As the plate is here again in its reduced state, the value P_r is the same as in Eqs. (5) and (6). If in Figs. 3b and 3c the deflections w_1 and w_2 of the first step are assumed to have the same ratio as in the buckled reduced plate in Fig. 3a, then the values w in Eqs. (6) and (9) are equal, and $w_1 + w_2 = w$. Hence, it follows from Eqs. (6) and (9) that

$$w = w_1 + w_2 = [(1/P_1) + (1/P_2)]P_r w$$

or

$$P_r = (P_1^{-1} + P_2^{-1})^{-1} \tag{10}$$

In order to take account of the proper rigidity of the faces, it is noted that, if their joint critical load is denoted by P_0 (Case 0), the extra compressive force, in order to give them the same deflection w as the reduced plate, is equal to P_0 (Fig. 3d). Hence, it follows that the actual critical load of the complete sandwich plate is, according to Eq. (10),

$$P_{cr} = P_0 + P_r = P_0 + (P_1^{-1} + P_2^{-1})^{-1} \tag{11}$$

If at the critical load the stress in the faces is in the plastic region, this has to be taken into account by multiplying P_0 and P_1 by a reduction factor η. For this purpose the safe assumption is made that the entire force P_{cr} is carried by the faces, so that η refers to the buckling stress $\sigma_{cr} = P_{cr}/2h$. It can be found by trial and error from the appropriate diagram (Fig. 4), as will be explained in an example at the end of this paper.

Consider, furthermore, a sandwich plate subjected to compression and supported at one or both of the unloaded edges. Here, it is difficult to compare internal and external moments, and it is more convenient to compare the restraining forces R and the deflecting forces D acting on an element $H\,dx\,dy$ (Fig. 5a). Assume again a reduced plate of which the rigidity is split into Cases 1 and 2. Assume first a deformation according to Case 1 alone, so that the critical thrust is P_1. The deflecting force D_1, caused by the transverse components of the compressive force P_1, is held in equilibrium by the restraining force R_1, given by the transverse shearing stresses. At a certain point and with a certain form of the middle plane, the deflecting force D_1 is proportional to P_1 and to w_1, and, hence, it may be denoted by cP_1w_1. Consequently, $R = D$ or

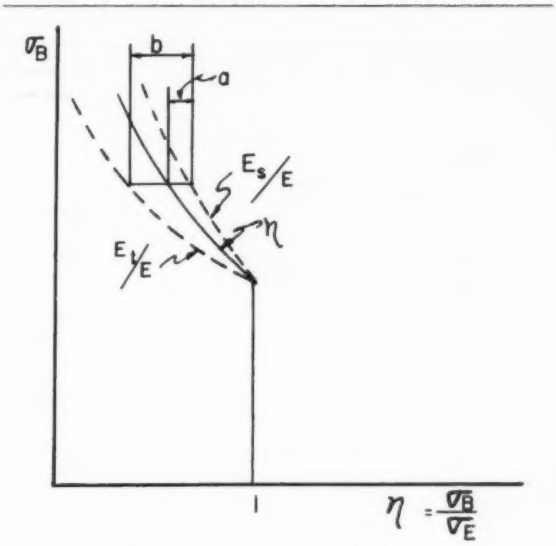

FIG. 4. Typical $\sigma_B - \eta$ diagram.

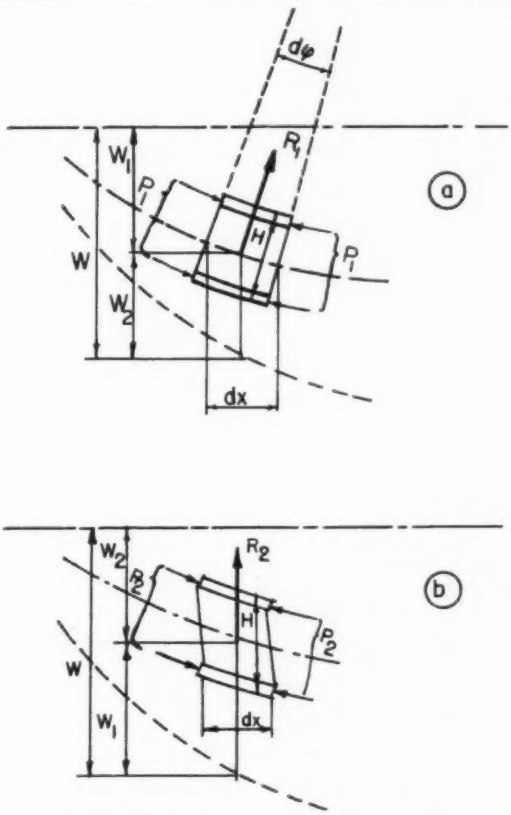

FIG. 5. Comparing deflecting and restraining forces for an element of a sandwich plate.

$$R_1 = cP_1w_1 \tag{12}$$

Again, let the shearing rigidity of the core decrease to its real value, by which the deflection increases by an

TABLE 1

CASE	BOUNDARY CONDITIONS AND LOADING	k_0	$\eta = \sigma_B / \sigma_E$	GRAPH FIG.	α
A.1	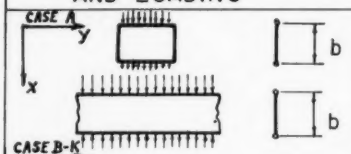	CASE 0: 1 CASE 1: 0.91	CASE 0: $\eta_0 = 0.91A$ CASE 1: $\eta_1 = E_t/E$	7	1
A.2		1	$0.91A$		
B	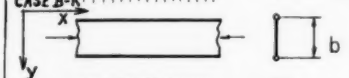	p = 2, q = 1	$0.91\,\frac{A/\beta^2 + p(B+2F) + qD\beta^2}{1/\beta^2 + p + q\beta^2}$	8	$1+\beta^2$
C	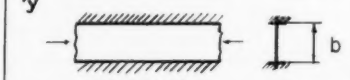	p = 2.5, q = 5		9	
D	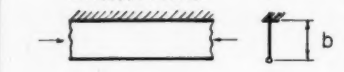	p = 2.27, q = 2.45		10	
E	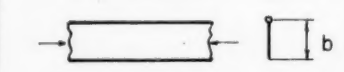	p = 0.425, q = 0	$0.91\,\frac{A/\beta^2 + 1.21F}{1/\beta^2 + 0.425}$	11	$1+(\beta^2/4)$
F	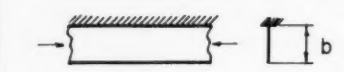	p = 0.57, q = 0.125	$0.91\,\frac{A/\beta^2 - 0.25B + 1.84F + 0.125D\beta^2}{1/\beta^2 + 0.57 + 0.125\beta^2}$	12	
G		$(k_0)_G$	Eq. (26)	13	$(1+\beta^2)^{1/2}$
H		$(k_0)_H$			
I	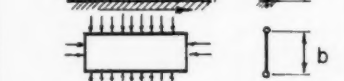	$1 + (b^2/a^2)$	$0.91A$	7	1
J		5.95			
K		Eq. (25)	$\frac{\gamma^2 \eta_B + 3\eta_G}{\gamma^2 + 3}$ $\gamma = P_x/P_{xy} = \sigma_x/\tau_{xy}$		$-\frac{\gamma}{2} + \left(\frac{\gamma^2}{4} + 1 + \beta^2\right)^{1/2}$

FIG. 6

CASE A.1

$$P_{cr} = \pi^2 D_e / b^2$$
$$D_e = \eta_0 D_f + 0.91 \eta_1 \varphi D_t$$
$$\varphi = \frac{\alpha}{0.91 \eta_1 r + \alpha}$$
(32)

ALL OTHER CASES

$$P_{cr} = \eta k_0 \pi^2 D_e / b^2$$
$$D_e = D_f + \varphi D_t$$
$$\varphi = \frac{\alpha}{\eta k_0 r + \alpha}$$
(31)

$\beta = L/b$, in which L is the half wave length in X- direction. β has to be chosen such as to make P_{cr} a minimum.

$D_f = E_f h^3 / 6(1-\nu^2)$; $D_t = E_f h (t+h)^2 / 2(1-\nu^2)$; $r = (\pi^2 D_t t) / (b^2 G_c (t+h)^2)$; G_c = modulus of rigidity core.
h = thickness faces ; t = thickness core ; E_f = elastic modulus faces, ν = Poisson's ratio faces.

amount w_2, while the internal stresses on the element remain constant and, hence, also R_1. Assuming the deflection surface w_2 to have the same form as w_1 and, hence, also as $w = w_1 + w_2$, it follows that the reduced critical thrust P_r now must satisfy, for any point of the plate, the condition $R = D$ or

$$cP_1w_1 = cP_rw \tag{13}$$

so that

$$w_1 = (P_r/P_1)w \tag{14}$$

being identical to Eq. (6).

Assuming, finally, Case 2 to occur (Fig. 5b), the critical thrust will be P_2, so that with the deflection w_2 it follows that $R = D$ or

$$R_2 = cP_2w_2 \tag{15}$$

Keeping the internal stresses on the element and, hence, R_2 constant and letting the rigidity of the faces decrease to its real value, the deflection increases by an amount w_1. It is now $R = D$ or

$$cP_2w_2 = cP_rw \tag{16}$$

so that

$$w_2 = (P_r/P_2)w \tag{17}$$

Eqs. (14) and (17) are identical to Eqs. (6) and (9), so that they also lead to Eq. (10) and, finally, to Eq. (11).

It will be clear that Eq. (11) also obtains if the plate is subjected to compression in two directions and to shear or a combination of these forces. With shear forces P_{xy} alone, with a certain form of the deflection surface w, the deflecting force D for a certain element is proportioned to P_{xy} and to w, so that it can be expressed as $cP_{xy}w$, which leads in the same way to Eq. (11). If at the same time compressive forces are present with a fixed ratio of these forces to P_{xy}, again the force D is proportional to P_{xy} and w, so that Eq. (11) also obtains.

In this derivation it was assumed that the deflection surfaces had the same form, so that the ratios w_1/w and w_2/w were the same for any point. This obtains indeed for Cases A_1, A_2, I, and J and for Case B of Table 1 if P_0, P_1, and P_2 are computed for the same half wave length in the X-direction. In the latter case, this half wave length has to be chosen such as to make P_{cr} a minimum. Hence, for these cases, Eq. (11) yields accurate results.

In other cases, the surfaces w_1, w_2, and w have different forms, but, since P_0, P_1, and P_2 are always calculated for the same half wave length, the difference is never extravagant. Since, in addition, admission of diverging deflection surfaces means a lack of restraint, Eq. (11) will yield conservative results for these cases. Indeed, by allowing the plate to choose for Cases 1 and 2 that deflection surface which makes P_1 and P_2 a minimum, it is provided with more choice than it actually has, so that the computed critical thrust from Eq. (11) may be smaller but never larger than the actual one. Seide[4] computed the buckling strength of sandwich plates with simply supported loaded and clamped unloaded edges, assuming the faces to act as membranes. The author has shown that, after taking account of the thickness and proper flexural rigidity of the faces, it follows from his results that, even for this very unfavorable case where the shapes of w_1 and w_2 differ considerably, Eq. (11) yields results that are only from 0 to 4 per cent conservative.[5] For pure shear,[6-8] although w_1 and w_2 have different forms, the discrepancies seem to be smaller than 1 per cent and not more than those obtaining for more laborious methods.

The author gives the above rather lengthy proof of his formula because it appears, from papers that refer to his method, that the more condensed version of it given previously[9, 3, 10] was not fully understood.

P_{cr} must be calculated from Eq. (11) for several half wave lengths L in order to find its minimum value, so that it is necessary to assemble data for P_0, P_1, and P_2 as functions of $\beta = L/b$ for several cases of loading and boundary conditions, as for example for Cases A–K in Table 1.

The Critical Loads P_0 and P_1 for Cases 0 and 1

For all cases represented in Table 1, the critical loads P_0 and P_1 may be expressed as

$$P_0 = \eta k_0 \pi^2 D_f/b^2 \tag{18}$$

$$P_1 = \eta k_0 \pi^2 D_t/b^2 \tag{19}$$

in which D_f is the joint flexural rigidity of the faces, being (Fig. 2)

$$D_f = E_f h^3/6(1 - \nu^2) \tag{20}$$

where E_f and ν are the elastic modulus and Poisson's ratio of the faces. D_t is the flexural rigidity of the plate as a whole, so that

$$D_t = E_f h(t + h)^2/2(1 - \nu^2) \tag{21}$$

It should have an additional term $E_c t^3/12(1 - \nu_c^2)$, in which E_c and ν_c refer to the core, to take care of the flexural rigidity of the core, but this term is so small that it nearly always may be neglected. Values h and t are the thicknesses of faces and core, respectively (Fig. 2). Value b is the width of the plates, as indicated in Table 1. Except for Cases $A.1$, I, and J, the plates are assumed to have infinite lengths. η is the reduction coefficient for plasticity.

Values k_0

Values k_0 in Eqs. (18) and (19) depend on loading and boundary conditions and follow from the theory of elastic stability of homogeneous plates.[11-14] The pertinent values are given in Table 1 as functions of the ratio β between half wave length L and width b. They are given graphically in Fig. 6 for Cases G and H. For Cases A, I, and J, the load P_2 is independent of the form of the deflection surface, so that the plate will buckle here in that form, which makes P_0 and P_1 minimum. Hence, for these cases, only minimum values

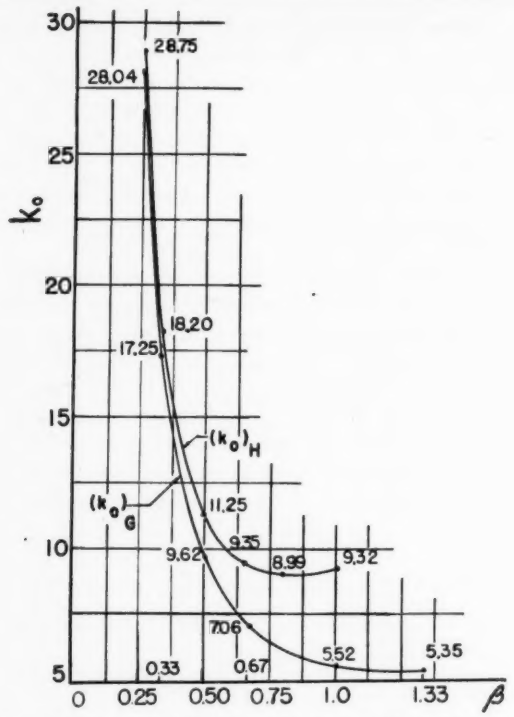

FIG. 6. Coefficients k_0 for Cases G and H as functions of $\beta = L/b$.

of P_0 and P_1 are needed, so that here only minimum values of k_0 are given. More details may be found in reference 15.

It is known[16] that, if minimum buckling stresses are compared, the interaction curve for shear stresses τ_{xy} and longitudinal normal stresses σ_x, as occur in Case K of Table 1, is the parabola

$$(\tau_{xy}/\tau_{xycr})^2 + \sigma_x/\sigma_{xcr} = 1 \tag{22}$$

in which τ_{xycr} and σ_{xcr} are the critical stresses if τ_{xy} and σ_x work alone. The author[15] found that the same relation holds if all critical stresses refer to the same wave length, which case has to be considered here. This is plausible, because it may be shown that this parabolic relation means that the so-called reduced principal compressive stress governs the buckling.

If for a certain half wave length L in X-direction the critical stress for pure compression (Case B) is σ_{xcr} and that for pure shear (Case G) is τ_{xycr}, it follows that, since for pure shear the principal compressive stress is also τ_{xycr}, in shear a principal compression is $(\sigma_{xcr} \div \tau_{xycr})$ as dangerous as in pure compression. If in combined loading by τ_{xy} and σ_x the shearing stresses are accordingly replaced by what will be called their reduced value $\tau_{xyr} = (\sigma_{xcr}/\tau_{xycr})\tau_{xy}$, also in shear buckling occurs at a reduced principal stress

$$\rho_{1r} = \tau_{xyr} = (\sigma_{xcr}/\tau_{xycr})\tau_{xycr} = \sigma_{xcr}$$

Hence, it may be expected that also in combined shear (τ_{xy}) and compression (σ_x) buckling occurs if the so-called reduced principal compressive stress is equal to σ_{xcr} or if

$$\rho_{1r} = (\sigma_x/2) + [(\sigma_x/2)^2 + \tau_{xyr}^2]^{1/2} = \sigma_{xcr}$$

or

$$\frac{\sigma_x^2}{4} + \frac{\sigma_{xcr}^2}{\tau_{xycr}^2}\tau_{xy}^2 = \left(\sigma_{xcr} - \frac{\sigma_x}{2}\right)^2$$

The latter equation is identical to Eq. (22). Denoting for Case K

$$\sigma_x/\tau_{xy} = P_x/P_{xy} = \gamma \tag{23}$$

Eq. (22) yields for Case K

$$(\tau_{xy})_K = \tau_{xycr}\left\{-\frac{\tau_{xycr}}{\sigma_{xcr}}\frac{\gamma}{2} + \left[1 + \left(\frac{\tau_{xycr}}{\sigma_{xcr}}\frac{\gamma}{2}\right)^2\right]^{1/2}\right\} \tag{24}$$

In reference 15, the author checked this equation by calculating σ_{xcr} (Case B), τ_{xycr} (Case G), and $(\tau_{xy})_K$. The last value, referring to Case K, was calculated for plastically equivalent stresses σ_x and τ_{xy} (i.e., $\sigma_x = \tau_{xy} \times \sqrt{3}$ or $\gamma = \sqrt{3}$). The accuracy of Eq. (24) was found to be satisfactory. From Eq. (24), k_0 for Case K may be expressed in the k_0 values for Cases B and G by the formula

$$(k_0)_K = (k_0)_G\left(-\frac{(k_0)_G}{(k_0)_B}\frac{\gamma}{2} + \left\{1 + \left[\frac{(k_0)_G}{(k_0)_B}\frac{\gamma}{2}\right]^2\right\}^{1/2}\right) \tag{25}$$

Hence, for Cases G, H, and K, the critical loads P_0 and P_1 in Eqs. (18) and (19) refer to the shear forces P_{xy} per unit length of the plate.

The Reduction Coefficients for Plasticity

Values η in Eqs. (18) and (19) represent the ratios between the plastic and elastic buckling stresses for the given half wave lengths L or ratios $\beta = L/b$. They follow from the author's theory of the plastic stability of plates and shells.[17–19] He derived the coefficients η in reference 15. For Cases A–F, I, and J, values η are given in Table 1, while for Cases G and H,[15]

$$\eta_G = \eta_H = 0.91\,\frac{(\alpha^{-1}\{[A(1+\alpha^4) + 2(B+2F)\alpha^2]\,\beta^{-2} + 2(3A\alpha^2 + B + 2F) + A\beta^2\})_{min.}}{\{\alpha^{-1}\,[(1+\alpha^2)^2\beta^{-2} + 2(3\alpha^2+1) + \beta^2]\}_{min.}} \tag{26}$$

The subscript (*min.*) indicates that α has to be chosen such that both numerator and denominator obtain minimum values. Furthermore, it was shown[15] that for combined compression σ_x and shear τ_{xy}, Case K, η_K may be expressed in η_B and η_G for Cases B and G for the same ratio $\beta = L/b$ and the same equivalent stress

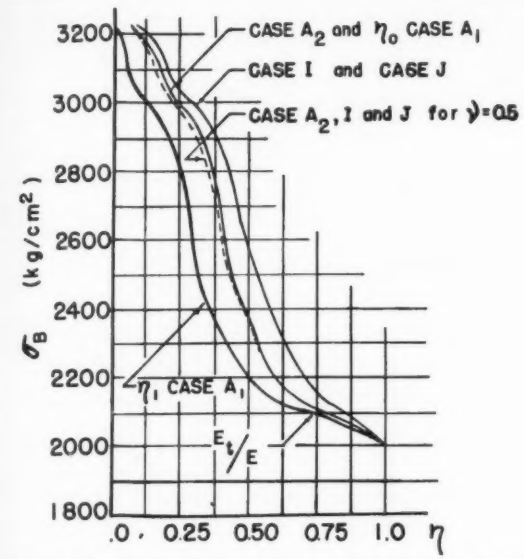

FIG. 7. Plastic reduction coefficients η for Cases A_1, A_2, I and J as functions of the equivalent buckling stress $\sigma_B = (\sigma_x^2 - \sigma_x\sigma_y + \sigma_y^2)^{1/2}$ for several ratios $\beta = L/b$.

$\sigma_B = (\sigma_x^2 + 3\tau_{xy}^2)^{1/2}$. Hence, η_B refers to $\sigma_x = \sigma_B$ and η_G to $\tau_{xy} = \sigma_B/\sqrt{3}$. η_K is given by the relation

$$\eta_K = (\gamma^2\eta_B + 3\eta_G)/(\gamma^2 + 3) \qquad (27)$$

where γ is given by Eq. (23). Also η_K is given in Table 1.

For Cases A–F, I, and J, where the coordinate axes coincide with the principal axes of the state of stress, values A, B, D, and F in the formulas for η are given by Eqs. (21) and (21a) of reference 19. For Cases A–F in these Eqs. (21) and (21a), the ratio $\beta = \rho_2/\rho_1$ of the principal stresses (which has nothing to do with the ratio $\beta = L/b$ in the present paper) has to be equated to zero. This yields

$$A = [1 + 3(1 + e)E_t/E]/\psi$$
$$B = 2[1 - (1 - 2\nu)E_t/E]/\psi$$
$$D = 4/\psi$$

where

$$\psi = 5 - 4\nu + 3e - (1 - 2\nu)^2E_t/E$$
$$F = 1/(2 + 2\nu + 3e)$$

Here, E_t is the tangent modulus and $e = (E/E_s) - 1$, where E_s is the secant modulus. More directly, $e = \epsilon_p/\epsilon_e$, where $\epsilon_p = \epsilon - \epsilon_e$ and $\epsilon_e = \sigma/E$ are the plastic and elastic strains at the buckling stress just before buckling.

For Cases I and J, $\beta = \rho_2/\rho_1$ is equal to unity, by which, for these cases, in Table 1

$$A = \frac{1 + 3(1 + e)E_t/E}{(2 + 2\nu + 3e)\,[1 + (1 - 2\nu)E_t/E]}$$

For Cases G and H, where the coordinate axes are in the planes of pure shear, values A, B, and F are given by Eqs. (57) of reference 17 or Eqs. (67) of reference 18.

$$A = \frac{4(1 + e)}{4(1 - \nu^2) + 4(2 - \nu)e + 3e^2}$$

$$B = \frac{2(2\nu + e)}{4(1 - \nu^2) + 4(2 - \nu)e + 3e^2}$$

$$F = \frac{E_t/E}{3 - (1 - 2\nu)E_t/E}$$

In all these cases, values E_t and e or E_s in these equations refer to a pure compressive stress equal to the equivalent buckling stress

$$\sigma_B = (\sigma_x^2 - \sigma_x\sigma_y + \sigma_y^2 + 3\tau_{xy}^2)^{1/2} \qquad (28)$$

In Case B, for example, $\sigma_B = \sigma_{xcr}$ and, in Case G, $\sigma_B = \tau_{xycr}\sqrt{3}$.

In Figs. 7–13, the coefficients η according to the formulas in Table 1 are given graphically as functions of this equivalent buckling stress σ_B for several ratios $\beta = L/b$ for avional, a Swiss aluminum alloy, to which Figs. 11–13 in reference 19 also apply. Similar graphs may be made for any other metal. Until these are available, a rough estimate may be made by an approximate derivation of the $\sigma_B - \eta$ relation for a given metal from the given graphs for avional. This could be done by drawing first the E_t/E and E_s/E curves for the given metal, as sketched in Fig. 4 by the dashed curves. Then, for a given equivalent buckling stress $(\sigma_B)_m$

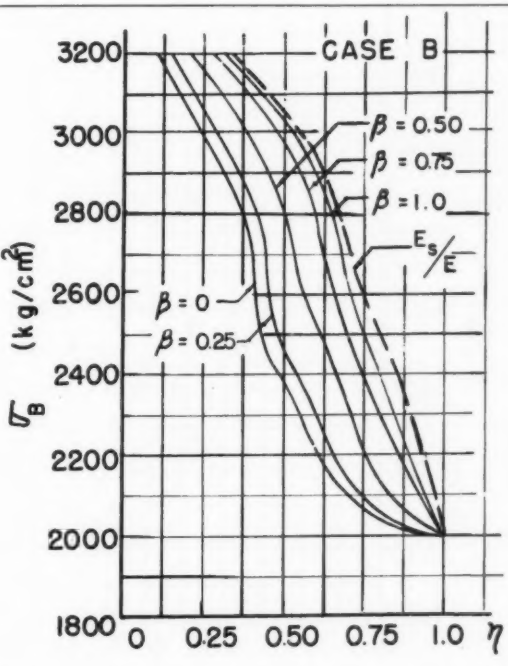

FIG. 8. Plastic reduction coefficients η for Case B as functions of the equivalent buckling stress $\sigma_B = \sigma_x$ for several ratios $\beta = L/b$.

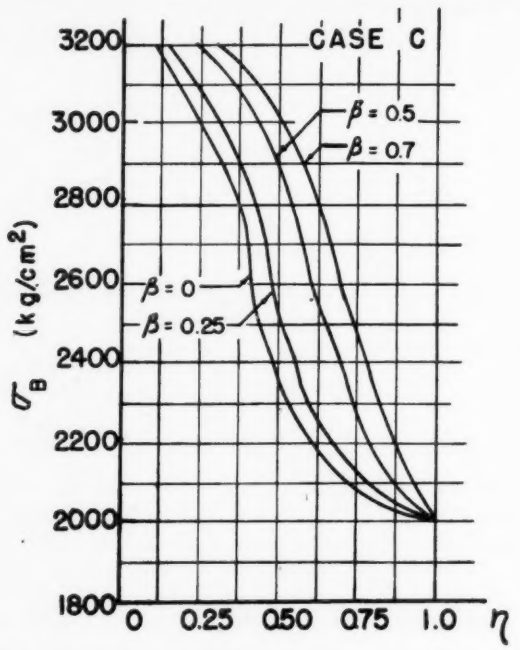

FIG. 9. Plastic reduction coefficients η for Case C as functions of the equivalent buckling stress $\sigma_B = \sigma_x$ for several ratios $\beta = L/b$.

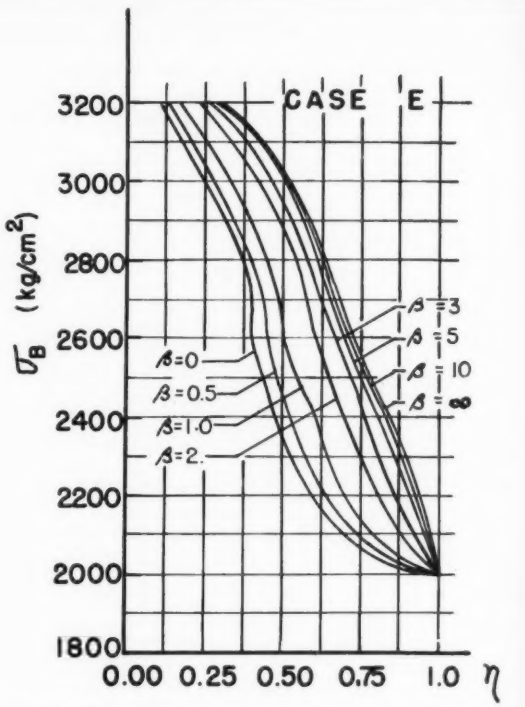

FIG. 11. Plastic reduction coefficients η for Case E as functions of the equivalent buckling stress $\sigma_B = \sigma_x$ for several ratios $\beta = L/b$.

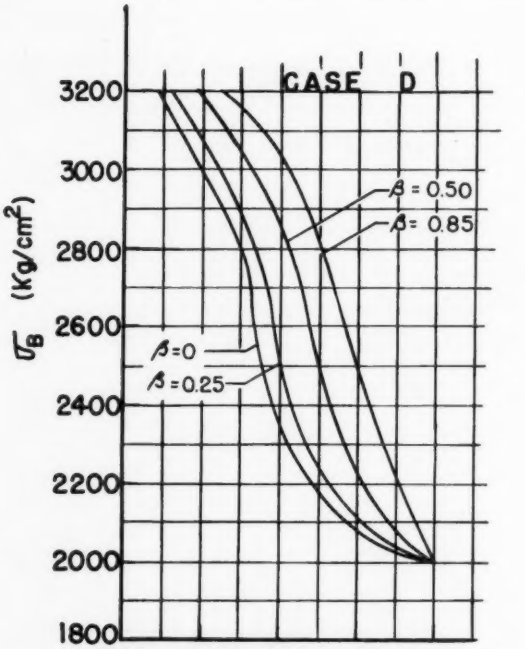

FIG. 10. Plastic reduction coefficients η for Case D as functions of the equivalent buckling stress $\sigma_B = \sigma_x$ for several ratios $\beta = L/b$.

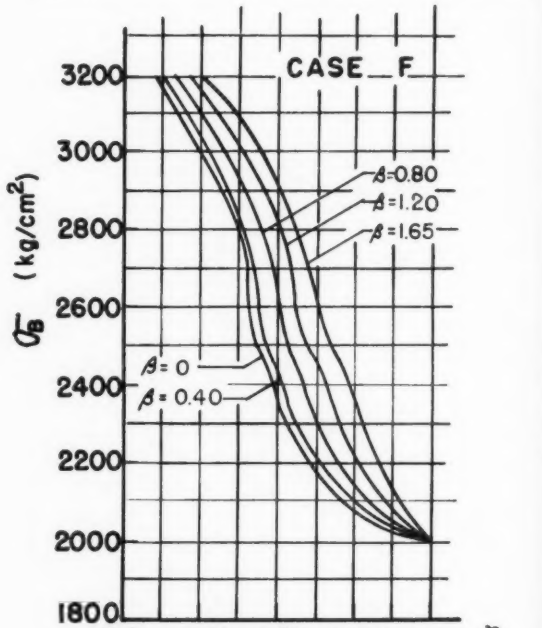

FIG. 12. Plastic reduction coefficients η for Case F as functions of the equivalent buckling stress $\sigma_B = \sigma_x$ for several ratios $\beta = L/b$.

of the metal, E_s/E is read from Fig. 4. Subsequently, $(\sigma_B)_a$, belonging to the same ratio E_s/E for avional, is read from Fig. 8, where E_s/E is given by the dashed curve. Then, E_t/E and η, belonging to $(\sigma_B)_a$ for avional, are found from the E_t/E curve in Fig. 7 and from the diagram for the pertinent case and for the chosen ratio $\beta = L/b$, respectively. The actual η value for the given metal is then found by assuming that, for $\sigma_B = (\sigma_B)_m$, the ratio

$$a/b = [(E_s/E) - \eta]/[(E_s/E) - (E_t/E)] \quad (29)$$

in Fig. 4 is the same as that found with $(\sigma_B)_a$ for avional.

The Critical Loads P_2 for Case 2

The critical loads P_2 for all cases of Table 1 may be expressed as

$$P_2 = \alpha[(t + h)^2/t]G_c \quad (30)$$

where G_c is the modulus of rigidity of the core. The pertinent coefficients α for various cases are given in Table 1. The author derived these coefficients in references 3 (Case *A*), 6 (Cases *B–D* and *G–H*), and 15 (Cases *A–K*). For Cases *G*, *H*, and *K*, the critical loads P_2 from Eq. (30) refer to the shear forces P_{xy}.

Computation of the Critical Loads P_{cr} of the Sandwich Plates

A more direct expression for the critical load P_{cr} is obtained by inserting Eqs. (18), (19), and (30) into Eq. (11), which yields

$$\left.\begin{aligned} &P_{cr} = \eta k_0 \pi^2 D_e/b^2 \\ &\text{where} \\ &D_e = D_f + \varphi D_t \\ &D_f = E_f h^3/6(1 - \nu^2) \\ &D_t = E_f h(t + h)^2/2(1 - \nu^2) \\ &\varphi = \alpha/(\eta k_0 r + \alpha) \\ &r = (\pi^2 D_t t)/[b^2 G_c (t + h)^2] \end{aligned}\right\} \quad (31)$$

Since for Case *A.1* values k_0 and η_0 for P_0 differ from values k_0 and η_1 for P_1 (Table 1), for this case Eq. (11) transforms to

$$\left.\begin{aligned} &P_{cr} = \pi^2 D_e/b^2 \\ &\text{where} \\ &D_e = \eta_0 D_f + 0.91\, \eta_1 \varphi D_t \\ &\varphi = \alpha/(0.91\, \eta_1 r + \alpha) \\ &D_t, D_f, \text{and } r \text{ according to Eqs. (31)} \end{aligned}\right\} \quad (32)$$

Values η, k_0, and α in Eqs. (31) all refer to the same wave length L and ratio $\beta = L/b$. If only buckling in the elastic range is considered, $\eta = 1$. In this case, P_{cr} is calculated for some ratios β in order to find its minimum value. However, in actual cases, r will practically always be found smaller than 0.1, in which case it is sufficiently accurate to calculate P_{cr} for the ratio β which makes P_1, and thus k_0, a minimum. These values β and the pertinent k_0 values may be found directly from reference 14; for Cases *G* and *H*, they may be found from Fig. 6. For Case *B*, for example, $\beta = 1$ and $k_0 = 4$, so that $\alpha = 2$. For Cases *G*, *H*, and *K*, the critical loads P_{cr} from Eqs. (31) refer to the critical shear forces $P_{xy} = 2h\tau_{xy}$.

With buckling in the plastic range, P_{cr} has to be calculated for some ratios $\beta = L/b$. After finding a first approximation of the buckling load, as explained in the numerical example below, values η that belong to the stress σ_B from Eq. (28), which is equivalent to this approximated state of stress at buckling, are found from the pertinent graph. For Cases *A–F*, for example, in Eq. (28), $\sigma_x = P_{cr}/2h$ and $\sigma_y = \tau_{xy} = 0$; for Case *K*, $\tau_{xy} = P_{xy}/2h = P_{cr}/2h$ and, from Eq. (23), $\sigma_x = \gamma\tau_{xy}$. After finding for which ratio β P_{cr} is minimum, the assumed approximated load has to be adjusted such that it checks with the thus computed more exact load.

Wrinkling of the Faces

Up to now, only buckling in relatively large half waves was considered, so that the strains of the core perpendicular to the middle plane could be neglected. This is, however, not allowed if buckling in waves of very small wave length, so-called wrinkling, is considered. The experimental wrinkling stress[2] was found to be considerably lower than the theoretical one.[2, 3] Obviously, this is caused by the unreliable properties of the core, since in this case the critical stress depends on the local rigidity of the core, so that irregularities diminish directly the buckling stress. With buckling as a plate, with larger wave length, only the average rigidity plays a role. Therefore, in the elastic domain, the wrinkling stress σ_{crw} found by Hoff and Mautner (reference 2, page 71) from tests should be adopted here, from which

$$P_{crw} = 2h\sigma_{crw} = h(E_f E_c G_c)^{1/3} \quad (33)$$

where E_c is the elastic modulus of the core in a direction perpendicular to the middle plane. This formula may be applied to any state of buckling stress if σ_{crw} is considered as the principal compressive stress.

In the plastic range, E_f has to be replaced by ηE_f. Since, here, practically cylindrical buckling occurs, for pure compression η is equal to its value for Case *A.2* of Table 1, so that

$$P_{crw} = 2h\sigma_{crw} = h(\eta E_f E_c G_c)^{1/3} = h(0.91 A E_f E_c G_c)^{1/3} \quad (34)$$

With an arbitrary state of stress, wrinkling occurs in waves perpendicular to the maximum principal compressive stress, so that Eq. (34) applies for any state of stress if the X-axis is assumed in the direction of the principal compressive stress. Value A has to be calculated from Eqs. (21a) of reference 19. In the ratio

TABLE 2

β	1	0.90	0.85	0.80
$(\sigma_{cr})_a$	2,250 kg. per sq.cm.			
η	0.87	0.85	0.84	0.83
k_0	4	4.04	4.104	4.20
α	2	1.81	1.7225	1.64
φ	0.89	0.883	0.877	0.87
D_e(in.lbs.)	23,660	23,500	23,350	23,150
$(P_{cr})_r$ (lbs. per in.)	1,300	1,275	1,271	1,275
$(\sigma_{cr})_r$ (lbs. per sq.in.)	32,500	31,900	31,770	31,900
$(\sigma_{cr})_r$ (kg. per sq.cm.)	2,290	2,245	2,236	2,245

$\beta = \rho_2/\rho_1$ in Eqs. (21a), ρ_1 and ρ_2 are here the principal compressive stresses at the buckling load and $\rho_2 < \rho_1$. Furthermore, E_t and $e = (E/E_s - 1)$ in these equations belong to the equivalent stress

$$\sigma_B = (\rho_1^2 - \rho_1\rho_2 + \rho_2^2)^{1/2}$$

or, with reference to the coordinate axes given in Table 1, to σ_B from Eq. (28). For Case K, for example,

$$\rho_{1,2} = (\sigma_x/2) \pm [(\sigma_x^2/4) + \tau_{xy}^2]^{1/2} \qquad (35)$$

For Cases A–F in Table 1, value $\eta = 0.91A$ in Eq. (34) is given for avional by the curves for Case $A.2$ in Fig. 7 or by the curves $\beta = L/b = 0$ for Cases B–F in Figs. 8–12, which are all similar. For Cases I and J, it is given by the curve for these cases in Fig. 7.

P_{cr} has to be calculated from Eqs. (31) or (32), as well as from Eq. (33) or (34). The smallest value P_{cr} is governing.

Numerical Example

Given a metalite-type sandwich plate. The thickness of the aluminum faces is $h = 0.02$ in.; that of the balsa core is $t = 0.46$ in. The plate is compressed in longitudinal direction and is simply supported at its unloaded sides (Case B). It has a width $b = 25$ in. Find its critical load.

Elastic Buckling

In this case, $\eta = 1$. Furthermore, Poisson's ratio ν for the faces is 0.3, $E_f = 10{,}500{,}000$ lbs. per sq.in., and $G_c = 12{,}000$ lbs. per sq.in. Hence, from Eqs. (31),

$$D_f = E_f h^3/6(1 - \nu^2) = 15.4 \text{ in.lbs.}$$
$$D_t = E_f h(t + h)^2/2(1 - \nu^2) = 26{,}600 \text{ in.lbs.}$$
$$r = (\pi^2 D_t t)/[b^2 G_c(t + h)^2] = 0.07$$

Since $r < 0.1$, it is sufficiently accurate (discrepancy about 1 per cent) to assume $\beta = L/b$ equal to that for buckling of homogeneous plates. Since, from Table 1, for Case B,

$$k_0 = (1/\beta^2) + 2 + \beta^2$$

this is the ratio β for which k_0 becomes minimum, being $\beta = 1$, from which $k_0 = 4$. Hence, from Table 1, value $\alpha = 1 + \beta^2 = 2$. This yields, from Eqs. (31),

$$\varphi = \alpha/(k_0 r + \alpha) = 0.878$$
$$D_e = D_f + \varphi D_t = 23{,}375 \text{ in.lbs.}$$

$$P_{cr} = k_0\pi^2 D_e/b^2 = 1{,}476 \text{ lbs. per in.}$$
$$\sigma_{cr} = P_{cr}/2h = 36{,}900 \text{ lbs. per sq.in.}$$

From Eq. (33), with $E_c = 330{,}000$ lbs. per sq.in.,

$$P_{crw} = h(E_f E_c G_c)^{1/3} = 6{,}920 \text{ lbs. per in.}$$

Hence, the governing critical load is 1,476 lbs. per in.

Plastic Buckling

If the critical stress $\sigma_{cr} = 36{,}900$ lbs. per sq.in. is above the proportional limit of the face material, the actual buckling stress will be less than 36,900 lbs. per sq.in. but higher than the proportional (elastic) limit. Assuming the faces to be made of avional, with an elastic limit of 2,000 kg. per sq.cm. = 28,400 lbs. per sq.in., an approximate value of the actual buckling stress σ_{cr} may be obtained as follows: From Eqs. (31), P_{cr} or σ_{cr} are approximately $\eta(P_{cr})_e$ or $\eta(\sigma_{cr})_e$, where $(\sigma_{cr})_e$ is the elastic buckling stress of 36,900 lbs. per sq.in. = 2600 kg. per sq.cm., so that $\sigma_{cr}/\eta = 2{,}600$ kg. per sq. cm., where η belongs to $\sigma_B = \sigma_{cr}$ in Fig. 8. Assuming also $\beta = 1$, from Fig. 8, $\sigma_B/\eta = \sigma_{cr}/\eta = 2{,}600$ kg. per sq. cm. if $\sigma_B = 2{,}250$ kg. per sq.cm. and $\eta = 0.87$, so that approximately $\sigma_{cr} = 2{,}250$ kg. per sq.cm. = 32,000 lbs. per sq.in. and $P_{cr} = (0.04)\ (32{,}000)$ lbs. per in. = 1,280 lbs. per in.

More accurately, σ_{cr} is found by assuming this approximate buckling stress $(\sigma_{cr})_a = 2{,}250$ kg. per sq.cm., reading the accessory η from Fig. 8 for several β values and calculating the resulting P_{cr} from Eqs. (31), denoted by $(P_{cr})_r$ in Table 2, where some intermediate values are also given.

Hence, $(P_{cr})_r$ is minimum for $\beta = L/b = 0.85$. To find the real value of P_{cr}, which may be assumed also to be minimum for $\beta = 0.85$, the assumed and resulting values, $(\sigma_{cr})_a = 2{,}250$ kg. per sq.cm. and $(\sigma_{cr})_r = 2{,}236$ kg. per sq.cm., should coincide. This appears to occur if $(\sigma_{cr})_a = (\sigma_{cr})_r = 2{,}245$ kg. per sq.cm. Hence, $\sigma_{cr} = 2{,}245$ kg. per sq.cm. = 31,900 lbs. per sq.in., and $P_{cr} = 2h\sigma_{cr} = 1{,}275$ lbs. per in.

Obviously, the first found approximate value $P_{cr} = \eta(P_{cr})_e = 1{,}280$ lbs. per in. was sufficiently accurate in this case. It underestimates P_{cr} for $\beta = 1$, but, since actually P_{cr} for $\beta < 1$ is smaller than for $\beta = 1$, it yields a fairly accurate result. It would be worth-while to check some cases in this respect, since this would highly simplify the calculation.

Assuming $P_{cr} = 1{,}275$ lbs. per in. and $\sigma_B = \sigma_{cr} = 2{,}245$ kg. per sq.cm., η in Eq. (34) is found from Fig. 8 for $\beta = 0$, yielding $\eta = 0.91A = 0.56$. Hence, from Eq. (34), $(P_{crw})_r = 5{,}700$ lbs. per in. Consequently, P_{crw} will be between 1,275 and 5,700 lbs. per in., so that the governing critical load is $P_{cr} = 1{,}275$ lbs. per in.

Shear Strength

Analogous to the design of lattice bars the plate should have a given shear strength in order to prevent failure by small irregularities. Requiring a shear strength of 3 per cent of P_{cr}, this yields for the above cases of elastic or plastic buckling $(0.03)(1{,}476) = 44$ lbs. per in. or $(0.03)(1{,}275) = 38$ lbs. per in. With a shear strength for balsa wood of $\tau_z = 175$ lbs. per sq.in., the shear strength of the plate is[5, 15] $S_z = (t + h)\tau_z = (0.48)(175) = 84$ lbs. per in. and is thus sufficient.

Applications of the Same Method to Other Problems

The author's method of split rigidities is more general than exposed here for the case of sandwich plates and may be applied to many other problems, as, for example, the buckling of latticed columns with batten plates or lacing,[9, 10] rammed piles surrounded by soil,[10] and torsional and flexural buckling of open sections.[20] It was also used to establish simple formulas for the interaction of column and plate buckling in built-up columns of various cross sections, which will be reported in an N.A.C.A. paper.

Acknowledgment

The graphs in Figs. 8–13 were calculated from the pertinent formulas by H. K. Lee, graduate student, which could be done because of a grant from the Cornell Faculty Research Grants Committee.

References

[1] Bijlaard, P. P., *Knikzekerheid van den bovenrand van open wandbruggen*, De Ingenieur, No. 4, footnote 2, 1932.

[2] Hoff, N. J., *The Strength of Laminates and Sandwich Structural Elements*, in *Engineering Laminates*, edited by A. G. H. Dietz; John Wiley and Sons, Inc., New York, 1949.

[3] Bijlaard, P. P., *On the elastic stability of thin plates, supported by a continuous medium*, Proc. Kon. Akad. v. Wetensch, Amsterdam, Vol. 49, No. 10, pp. 1189–1199, December, 1946.

[4] Seide, P., *Compressive Buckling of Flat Rectangular Metalite Type Sandwich Plates with Simply Supported Loaded Edges and Clamped Unloaded Edges*, N.A.C.A. T.N. No. 1886, May, 1949.

[5] Bijlaard, P. P., *Stability of Sandwich Plates*, Journal of the Aeronautical Sciences, Vol. 16, No. 9, pp. 573–574, September, 1949.

[6] Bijlaard, P. P., *On the Elastic Stability of Sandwich Plates, I–II*, Proc. Kon. Akad. v. Wetensch, Amsterdam, Vol. 50, Nos. 1 and 2, pp. 79–87 and 186–193, January–February, 1947.

[7] Seide, P., *Shear Buckling of Infinitely Long Simply Supported Metalite Type Sandwich Plates*, N.A.C.A. T.N. No. 1910, July, 1949.

[8] Plantema, F. J., and deKock, A. C., *The Elastic Overall Instability of Sandwich Plates with Simply Supported Edges*, Rep. S. 346, Nationaal Luchtvaart Laboratorium, Amsterdam, December, 1948.

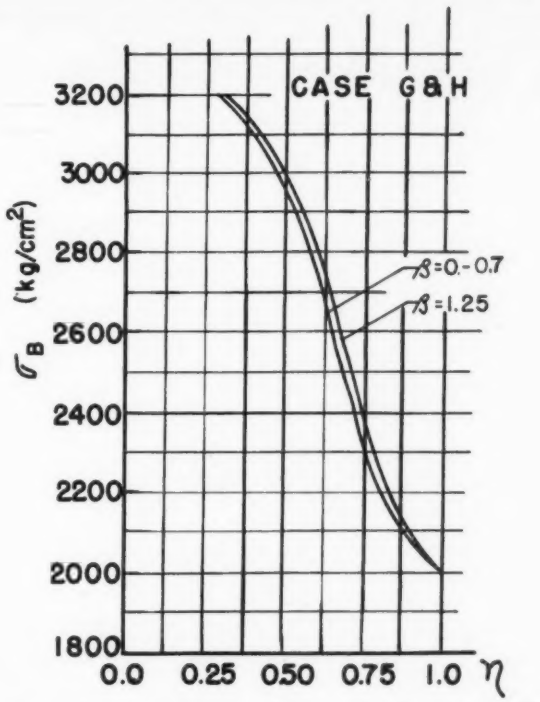

FIG. 13. Plastic reduction coefficients η for Cases *G* and *H* as functions of the equivalent buckling stress $\sigma_B = \tau_{zy}\sqrt{3}$ for several ratios $\beta = L/b$.

[9] Bijlaard, P. P., *Berekening van de knikspanning van gekoppelde profielen volgens een nieuwe methode*, De Ingenieur in Ned. Indie, No. 3, 1939.

[10] Bijlaard, P. P., *Some Contributions to the Theory of Elastic and Plastic Stability*, Publ. Internat. Assoc. of Bridge and Struct. Engineering, Zürich, Vol. 8, pp. 17–80, 1947.

[11] Bleich, F., *Theorie and Berechnung der eisernen Brücken;* Springer, Berlin, 1924.

[12] Kollbrunner, C. F., *Das Ausbeulen der auf einseitigen gleichmässig verteilten Druck beanspruchten Platten im elastischen und plastischen Bereich*, Mitt. a. d. Institut f. Baustatik a. d. E.T.H., Zürich, No. 17, 1946.

[13] Southwell, R. V., and Skan, Sylvia W., *On the Stability Under Shearing Forces of a Flat Elastic Strip*, Proc. Roy. Soc. London, Ser. A, Vol. 105, No. 733, pp. 582–607, May, 1924.

[14] Timoshenko, S., *Theory of Elastic Stability;* McGraw-Hill Book Company, Inc., New York, 1936.

[15] Bijlaard, P. P., *Analysis of the Elastic and Plastic Stability of Sandwich Plates by the Method of Split Rigidities*, Preprint No. 259, Institute of the Aeronautical Sciences, January, 1950.

[16] Batdorf, S. B., and Stein, M., *Critical Combinations of Shear and Direct Stress for Simply Supported Rectangular Flat Plates*, N.A.C.A. T.N. No. 1223, March, 1947.

[17] Bijlaard, P. P., *A theory of plastic stability and its application to thin plates of structural steel*, Proc. Kon. Akad. v. Wetensch, Amsterdam, Vol. 41, No. 7, pp. 731–743, September, 1938.

[18] Bijlaard, P. P., *Theory of the plastic stability of thin plates*, Publ. Internat. Assoc. f. Bridge and Struct. Engineering, Zürich, Vol. 6, pp. 45–69, 1940–1941.

[19] Bijlaard, P. P., *Theory and Tests on the Plastic Stability of Plates and Shells*, Journal of the Aeronautical Sciences, Vol. 16, No. 9, pp. 529–541, September, 1949.

[20] Bijlaard, P. P., *On the torsional and flexural stability of thin walled open sections*, Proc. Kon. Akad. v. Wetensch, Amsterdam, Vol. 51, No. 3, pp. 314–321, March, 1948.

Readers' Forum

BRIEF REPORTS of investigations in the aeronautical sciences and discussions of papers published in the JOURNAL are presented in this special department. The publication will be completed approximately 8 to 10 weeks after receipt of the material. The Editorial Committee does not hold itself responsible for the opinions expressed by the correspondents. Contributions should not exceed 800 words in length.

New Compressibility Correction for Two-Dimensional Subsonic Flow

E. V. Laitone
Associate Professor, University of California at Berkeley
February 26, 1951

SUMMARY

By using the local Mach Number rather than the free-stream Mach Number in the ordinary Prandtl-Glauert correction for subsonic two-dimensional isentropic gas flow, a simple new relation is obtained between the compressible and the incompressible surface pressure coefficient. The new relation includes the effect of the specific heat ratio and gives a better agreement with experimental data than does the von Kármán-Tsien relation.

INTRODUCTION

THE PRANDTL-GLAUERT COMPRESSIBILITY CORRECTION for the local surface pressure coefficient is generally written (see reference 1, page 140) as

$$C_p = C_{p_0}/\sqrt{1 - M_\infty^2} \tag{1}$$

Eq. (1) is derived from the linearized potential equation by neglecting all the square or higher order terms of the perturbation potential (see reference 1, page 125). The surface pressure coefficient C_p is then of the same order as the first power of the perturbation potential (see reference 1, page 126).

In this form, Eq. (1) is rigorously applicable only to a very slender body having a cusped nose with no stagnation point. When applied to even relatively thin airfoils, it gives a reasonable prediction only for the portions near free-stream pressure and only for low values of the free-stream Mach Number.

By an analytical continuation it is easily shown, however, that a better approximation for the local compressibility effect on any finite body is obtained by replacing the free-stream Mach Number M_∞ by the local Mach Number M_L so that

$$C_p = C_{p_0}/\sqrt{1 - M_L^2} \tag{2}$$

This essentially applies the Prandtl-Glauert linearized potential equation to the local flow field considered approximately uniform. The same procedure, using the local Mach Number in the Prandtl-Glauert correction, was first suggested in reference 2 and was later justified by the experimental results presented in reference 3 for the particular case of the subsonic flow field existing behind a detached shock wave in transonic flow.

THE NEW COMPRESSIBILITY CORRECTION

The surface pressure coefficient may be written (see reference 1, page 28) as

$$C_p = \frac{p_L - p_\infty}{(1/2)\rho_\infty U_\infty^2} = \frac{2}{\gamma M_\infty^2}\left(\frac{p_L}{p_\infty} - 1\right) \tag{3}$$

where for isentropic flow (see reference 1, page 125)

$$\frac{p_L}{p_\infty} = \left\{\frac{1 + [(\gamma - 1)/2]M_\infty^2}{1 + [(\gamma - 1)/2]M_L^2}\right\}^{\gamma/(\gamma - 1)} \tag{4}$$

Then substituting Eq. (4) into Eq. (3) and solving for the local Mach Number M_L, we obtain the exact expression

$$M_L^2 = \left(M_\infty^2 + \frac{2}{\gamma - 1}\right)\left(1 + \frac{\gamma M_\infty^2}{2} C_p\right)^{-(\gamma-1)/\gamma} - \frac{2}{\gamma - 1} \tag{5}$$

Now, before substituting Eq. (5) into Eq. (2), we must be cognizant of the fact that only the first-order terms of C_p, corresponding to the first order of the local perturbation potential, were retained in deriving Eq. (2) for the local flow field. Consequently, Eq. (5) must be reduced to the first order in C_p so that

$$M_L^2 = M_\infty^2 - \left(1 + \frac{\gamma - 1}{2} M_\infty^2\right) M_\infty^2 C_{p_0} \tag{6}$$

Then, substituting Eq. (6) into Eq. (2) and retaining only the first-order term of C_p in the local flow field correction in the denominator, we obtain

$$C_p = \frac{C_{p_0}}{\sqrt{1 - M_\infty^2} + \dfrac{M_\infty^2}{\sqrt{1 - M_\infty^2}} \dfrac{C_{p_0}}{2}\left(1 + \dfrac{\gamma - 1}{2} M_\infty^2\right)} \tag{7}$$

Eq. (7) is a new relation for the two-dimensional compressible pressure coefficient and provides a better agreement with experimental data for airfoils than does the von Kármán-Tsien relation (see either reference 4 or reference 1, page 185)

$$C_p = \frac{C_{p_0}}{\sqrt{1 - M_\infty^2} + \dfrac{M_\infty^2}{1 + \sqrt{1 - M_\infty^2}} \dfrac{C_{p_0}}{2}} \tag{8}$$

It is interesting to note that the term containing the specific heat ratio γ is associated with the term M_∞^4, as would be expected from a comparison of the von Kármán-Tsien straight-line pressure-density variation (corresponding to $\gamma = -1$) with the exact isentropic variation (see reference 1, page 173).

REFERENCES

[1] Liepmann, H. W., and Puckett, A. E., *Introduction to Aerodynamics of a Compressible Fluid;* John Wiley & Sons, Inc., New York, 1947.

[2] Laitone, E. V., and Pardee, Otway O., *Location of Detached Shock Wave in Front of a Body Moving at Supersonic Speeds,* N.A.C.A. R.M. No. A7B10, May 6, 1947.

[3] Laitone, E. V., *An Experimental Investigation of Transonic and Accelerated Supersonic Flow by the Hydraulic Analogy,* University of California, Institute of Engineering Research, Berkeley, Series No. 3, Issue No. 315, July 3, 1950.

[4] von Kármán, Theodore, *Compressibility Effects in Aerodynamics,* Journal of the Aeronautical Sciences, Vol. 8, No. 9, pp. 337–356, July, 1941.

Note on the Minimum Critical Reynolds Number and the Form Parameter*

John C. Freeman, Jr.
Department of Meteorology, The University of Chicago
February 9, 1951

IN THE THEORY OF THE BOUNDARY LAYER of an incompressible fluid, the "form parameter" $H = \delta_1/\vartheta$,[1] where δ_1 is the displacement thickness and ϑ is the momentum thickness, has been found useful as a parameter to characterize turbulent boundary layers[1] and (empirically) as a parameter that determines R_1 (the minimum critical Reynolds Number based on the displacement thickness) for laminar boundary-layer profiles on a porous flat plate

* This work was started at Brown University.

with two different types of suction.[2] In this note it will be shown that, if sufficient suction of the type $v_0(x) \sim x^{(m-1)/2}$ is introduced on a flat plate with pressure gradient [such that the free-stream velocity $u_0(x) = U_0 x^m$], R_1 for many of the resulting profiles is essentially determined by H. The proof will be accomplished by showing that, following a suitable change of scale, all of the profiles mentioned above can be closely approximated by members of the family of profiles computed by Schlichting and Bussmann[3] for the case for which the suction velocity $v_0(x) \sim 1/\sqrt{x}$ and for which there is no pressure gradient (i.e., $m = 0$). R_1 and H are both unchanged by the transformations involved, and thus the dependence of R_1 on H is established.

These results should be useful in the study of boundary-layer control along a curved surface.

Suction is introduced on a flat plate with pressure gradient such that $u_0(x) = U_0 x^m$ [with Hartree parameter $\beta = 2m \div (m+1)$] so that the velocity into the plate is

$$v_0(x) = -c_1\sqrt{\nu U_0(m+1)\,x^{m-1}/2} \tag{1}$$

If the stream function is assumed to be of the form

$$\psi(x, y) = \sqrt{2\nu U_0 x^{m+1}/(m+1)}\, f(z) \tag{2}$$

where

$$z = y\sqrt{U_0 x^m (m+1)/2\nu x} \tag{3}$$

then the Prandtl boundary-layer equation becomes the familiar Hartree equation

$$f''' + ff'' = \beta(f'^2 - 1) \tag{4}$$

with the new boundary conditions

$$\left.\begin{aligned} f'(0) &= 0, \qquad f(0) = C_1 \\ f'(\infty) &= 1 \end{aligned}\right\} \tag{5}$$

This equation has been solved numerically by Hartree[4] for $C_1 = 0$ and several values of β and by Schlichting and Bussmann[3] with $\beta = 0$ and 1 for several values of C_1. We are not interested here in exact solutions to Eq. (4) but rather in the approximate solutions obtained as follows: We set

$$f + K = w \tag{6}$$

where

$$K = \beta/f''(0) \tag{7}$$

and neglect the right-hand side of the resulting equation,

$$w''' + ww'' = \beta\{[w''/w''(0)] + w'^2 - 1\} \tag{8}$$

with boundary conditions

$$\left.\begin{aligned} w'(0) &= 0, \qquad w(0) = C_1 + K = \rho \\ w'(\infty) &= 1 \end{aligned}\right\} \tag{9}$$

This gives us

$$w''' + ww'' = 0 \tag{10}$$

with boundary conditions above.

This equation has been solved numerically by Schlichting and Bussmann[3] for several values of ρ from $-3/2$ to $+5$. For values of $\rho > 0$, the quantity

$$\beta\{[w''/w''(0)] + w'^2 - 1\} \leq w'''/8 \tag{11}$$

for all z and thus can be neglected. This is sufficient to show that each one of all the classes of profiles obtained when β is varied between -0.198 and 2 is approximately the same as the c'ass for $\beta = 0$, provided C_1 is such that $\rho > 0$ (i.e., the profiles depend essentially on ρ and not on β).

A similar but slightly less satisfactory demonstration that the profiles for arbitrary suction on a plate with pressure gradient depend only on ρ can be given.

Lin's formula for the minimum value of R_1[5] is written as follows:

$$R_1 = 25w''(0)\int_0^\infty (1 - w')dz/[w'(z_1)]^4 \tag{12}$$

where z_1 is the value of z for which

$$\pi w''(0)\left[\frac{2w''(0)z}{w'(z)} - 3\right]\frac{w'(z)w'''(z)}{[w''(z)]^2} = 0.58 \tag{13}$$

Thus, it is obvious that R_1 is essentially independent of β and $v_0(x)$ and depends only on ρ. Since

$$H = \delta_1/\vartheta = \int_0^\infty (1 - w')dz \Big/ \int_0^\infty w'(1 - w')dz \tag{14}$$

for all of these profiles, it also depends essentially on ρ. Thus, the empirical results that H determines R_1 for any of the profiles with $\beta = 0$ [$v_0(x) \sim 1/\sqrt{x}$] and $\rho = 0$ (see Fig. 18 of the Stability Monograph[6]) are given a theoretical basis and are seen to be only special cases of a more general result.

References

[1] Tetervin, N., *A Review of Boundary-Layer Literature*, N.A.C.A. T.N. No. 1384, July, 1947.

[2] Ulrich, A., *Die Stabilität der laminaren Reibungszschict an der ebenen Platte mit homogener Absaugung*, ZWB UM 2033, November, 1943. (Summary by Brown University, No. A-9106.)

[3] Schlicting, H., and Bussmann, K., *Exakte Lösungen für die laminare Grenzschicht mit Absaugung und Ausblasen*, Schriftum der deutschen Akademie der Luftfahrtforschung, Vol. 7B, pp. 25–69, 1943.

[4] Hartree D. R., *On an Equation Occurring in Falkner and Skan's Approximate Treatment of the Equation of the Boundary Layer*, Proc. Camb. Phil. Soc., Vol. 33, pp. 222–239, 1937.

[5] Lin, C. C., *On the Stability of Two-Dimensional Parallel Flows, III*, Q. Appl. Math., Vol. 3, pp. 277–301, 1945.

[6] Chiarulli, P., and Freeman, J. C., *Monograph VI, Stability of the Boundary Layer*, Air Material Command Technical Report No. F-TR-1197-IA, 1948.

The Influence of the Temperature Variation of the Specific Heats of Air in Shock-Wave Calculations

J. Kestin

Head, Department of Mechanical Engineering, Polish University College, London, England

February 1, 1951

In a recent paper on the structure of shock waves, Meyerhoff[1] discusses the influence of the temperature variation of the specific heats of air on shock-wave calculations. The method of calculation requires a great deal of numerical computation that can be avoided by an approximate, but sufficiently accurate, method.

The shock transition is defined by the following three equations:

$$\rho_0 u_0 = \rho_1 u_1 = m \tag{1}$$

$$p_0 + mu_0 = p_1 + mu_1 = mC \tag{2}$$

$$h_0 + (1/2)u_0^2 = h_1 + (1/2)u_1^2 = H \tag{3}$$

where h denotes enthalpy, H is the constant stagnation enthalpy, and the remaining symbols have the same meaning as in reference 1. These equations, together with the perfect gas equation

$$p = RT\rho \tag{4}$$

and the condition that for a perfect gas, the enthalpy is a function of temperature alone

$$h = h(T) \tag{5}$$

with h given in tabulated form,[2] provide all the equations needed to calculate quantities with subscript 1 if those with subscript 0 are given. Apart from the trivial solution

$$u_0/u_1 = p_0/p_1 = T_0/T_1 = \ldots = 1 \tag{6}$$

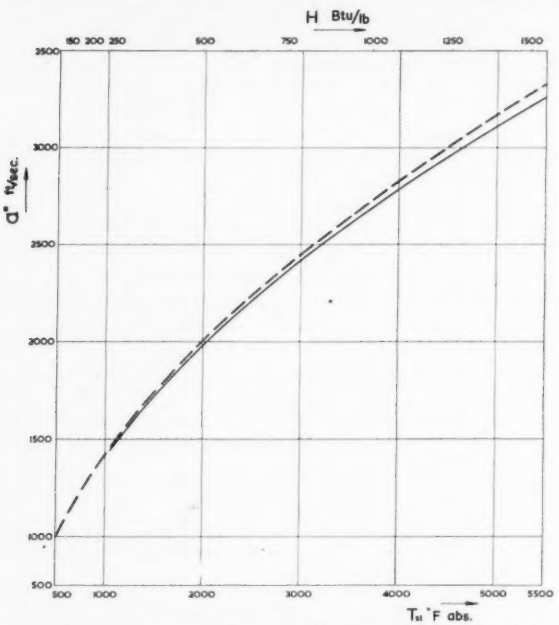

FIG. A. Sonic stream velocity, a^* ft. per sec., in terms of the stagnation temperature, T_{st} °F. abs. —— variable specific heats. – – – constant specific heats, $\gamma = 1.400$.

the set of equations leads to one solution for which the ratios in Eq. (6) differ from unity.

If we analyze the dimensionless function

$$\left.\begin{aligned} z &= \frac{C}{a^*} = \frac{p}{\rho u a^*} + \frac{u}{a^*} \\ &= \frac{R}{a^{*2}}\left[\frac{T(h)}{x}\right] + x \end{aligned}\right\} \tag{7}$$

where $x = u/a^*$ and a^* is the sonic stream velocity, determined solely by the value of H, we can easily prove that it has a minimum at

$$u = a^* \quad \text{or} \quad x = 1 \tag{7a}$$

it being evident that it remains constant across a shock transition. In Eq. (7) $T(h)$ is the inverse of Eq. (5). Moreover, z is a function of a single variable, since, by Eq. (3),

$$\left.\begin{aligned} h &= H - (1/2)u^2 \\ &= H - (1/2)a^{*2}x^2 \end{aligned}\right\} \tag{3a}$$

We shall now inquire into the conditions under which the very well known Prandtl[3] equation

$$u_0 u_1 = a^{*2} \quad \text{or} \quad x_0 x_1 = 1 \tag{8}$$

which is rigorous for constant specific heats applies to cases with variable specific heats. For this to be so, the relationship between T and h must be such as to render the expression

$$z = \frac{R}{a^{*2}}\left\{\frac{T[H - (1/2)a^{*2}x^2]}{x}\right\} + x \tag{7b}$$

invariant with respect to the transformation of x to $1/x$, in view of Eq. (8). Limiting our considerations to elementary functions, we see that this condition can be fulfilled only if T is proportional to $H - (1/2)a^{*2}x^2$ (i.e., if T and h are linearly dependent). Thus, the validity of the Prandtl equation is limited to temperature ranges over which a linear relation between T and h offers a good approximation to the tabulated function $h(T)$. From Fig. 7, reference 1, we can see that this is the case over relatively large ranges of temperature, and, consequently, Eq. (8) can be expected to lead to sufficiently accurate results if the initial supersonic Mach Number and the stagnation enthalpy are not too large.

The assumption of a linear relationship between enthalpy, h, and absolute temperature, T, is equivalent to the assumption of a constant value for c_p, c_v, and γ, but by the use of Eq. (8) the cumbersome calculation of the appropriate mean value of γ is

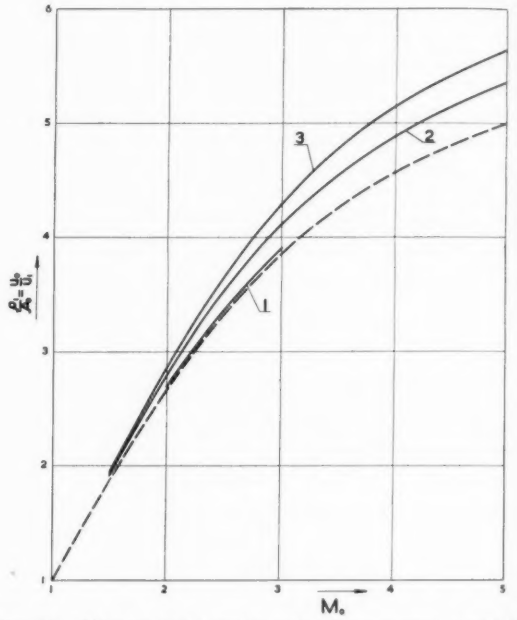

FIG. B. Velocity and density ratio across normal shock for various stagnation temperatures. —— variable specific heats; (1) T_{st} = 1,000°F. abs.; (2) T_{st} = 2,000°F. abs.; (3) T_{st} = 3,000°F. abs. – – – constant specific heats, $\gamma = 1.400$.

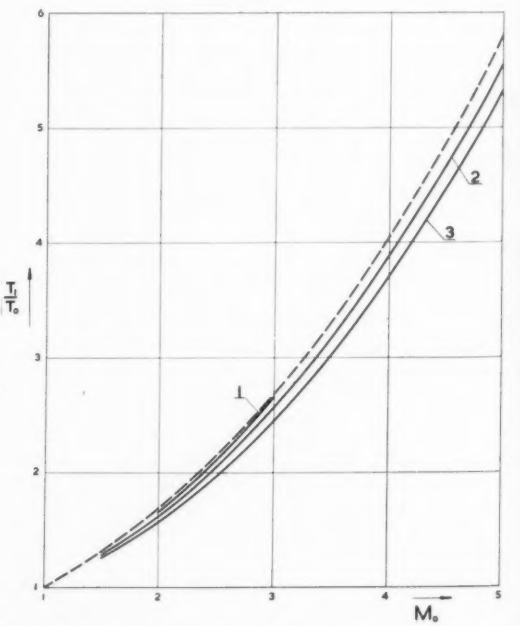

FIG. C. Temperature ratio across normal shock for various stagnation temperatures. —— variable specific heats; (1) T_{st} = 1,000°F. abs.; (2) T_{st} = 2,000°F. abs.; (3) T_{st} = 3,000°F. abs. – – – constant specific heats, $\gamma = 1.400$.

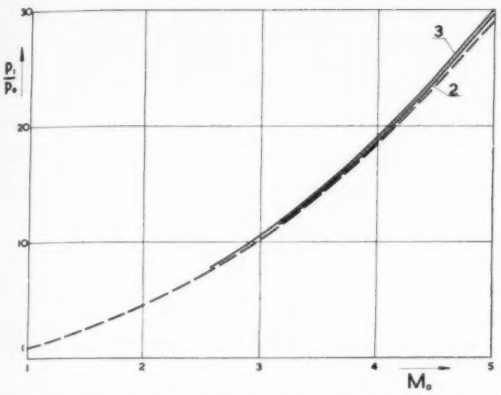

FIG. D. Pressure ratio across normal shock for various stagnation temperatures. —— variable specific heats; (2) T_{st} = 2,000°F. abs.; (3) T_{st} = 3,000°F. abs. – – – constant specific heats, γ = 1.400.

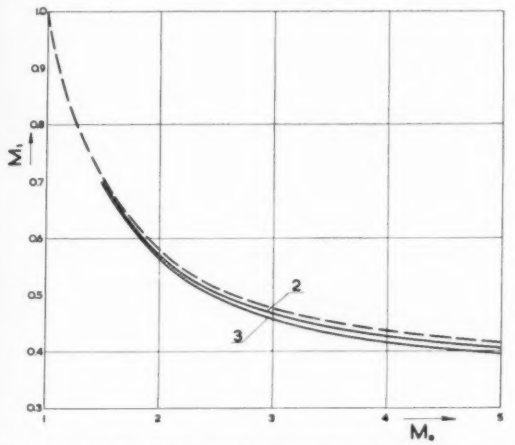

FIG. E. Mach Number behind normal shock wave. —— variable specific heats; (2) T_{st} = 2,000°F. abs.; (3) T_{st} = 3,000°F. abs. – – – constant specific heats, γ = 1.400.

avoided. Furthermore, the approximation is used only in one step—i.e., in that involving the calculation of u_1 from u_0.

The values of sonic stream temperatures, T^*, and the corresponding sonic stream velocities, a^*, have been calculated elsewhere[4] for a number of stagnation temperatures and enthalpies H, on the basis of reference 2. Fig. A gives a plot of a^* in terms of H and the corresponding stagnation temperature T_{st}. With the aid of these values we can use Eq. (8) to calculate the velocity ratio

$$U_1 = u_1/u_0 = a^{*2}/u_0^2 = (a^*/a_0)^2/M_0^2 \qquad (9)$$

from which all other quantities can be easily deduced, as shown in reference 1, particularly with the aid of the tables in reference 4.

The error can be assessed by calculating u_0 and u_1 with the aid of Eq. (8) and by comparing the values of z: For example, for T_{st} = 3,000°F. abs. (H = 790.68 B.t.u. per lb. °F.), M_1 = 5, we obtain

a^* = 2,419 ft. per sec.
u_0 = 5,748 ft. per sec. $z_0 = 2.46$
u_1 = 1,018 ft. per sec. $z_1 = 2.44$

and $\Delta z/z \simeq 0.8$ per cent, which is negligible.

Figs. B, C, D, and E contain some results from which the influence of the stagnation temperature can be assessed. The graphs also contain curves calculated with γ = 1.400 for comparison.

REFERENCES

[1] Meyerhoff, L., *An Extension of the Theory of the One-Dimensional Shock-Wave Structure*, Journal of the Aeronautical Sciences, Vol. 17, No. 12, p. 775, December, 1950.

[2] Keenan, J. H., and Kaye, J., *Gas Tables;* John Wiley & Sons, Inc., New York, 1947.

[3] Liepmann, H. W., and Puckett, A. E., *Introduction to Aerodynamics of a Compressible Fluid*, Galcit Series, p. 39; John Wiley & Sons, Inc., New York, 1947.

[4] Kestin, J., *Influence of Variable Specific Heats on the High-Speed Flow of Air*, Aer. Res. Council, Current Papers Series (to be published).

Convective Heat Transfer from Spheres in a Free-Molecule Flow

F. M. Sauer
Assistant Professor of Mechanical Engineering, University of California at Berkeley
January 19, 1951

THE PURPOSE OF THIS NOTE is to extend the heat-transfer calculations of Stalder and Jukoff[1] in the free-molecule flow régime of rarefied gas dynamics to include the case of heat transfer from spheres.

Using the conventional methods of kinetic theory, in reference 1 is developed an analysis for the heat transfer from a plane surface inclined at an angle to the flow velocity. If the surface of the sphere to be investigated is postulated to be isothermal, the results of reference 1 may be integrated over the sphere to yield the average heat-transfer rate.

The convective heat flux from an elementary plane surface, dA, inclined at an angle θ with the flow velocity, is, for a monatomic gas, given as*

$$dq/dA = 2\alpha nkT_p - \alpha E_t \qquad (1)$$

and for a diatomic gas (dumbbell type molecule) as

$$dq/dA = 3\alpha nkT_p - \alpha(E_t + nkT_i) \qquad (2)$$

where

$$E_t = n[(mU^2/2) + \varphi kT_i]$$
$$n = (NV_m/2\sqrt{\pi})\{e^{-s^2} + \sqrt{\pi}\, s[1 + erf(s)]\}$$

* The symbols used are as far as possible those of reference 1. Eqs. (1) and (2) are the corrected form of equations presented in the reference.

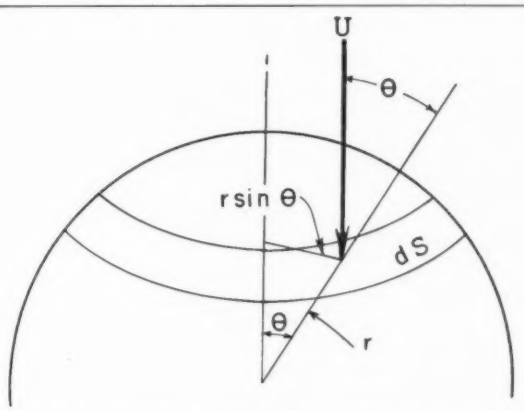

FIG. 1. The coordinate system used in the analysis.

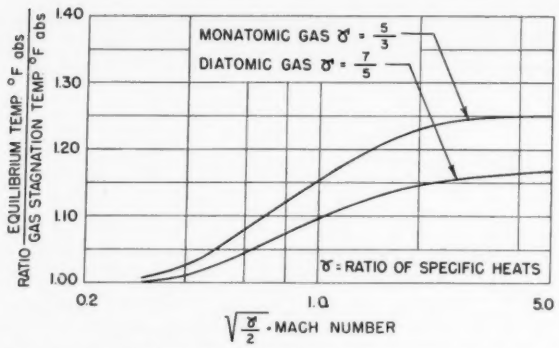

FIG. 2. Equilibrium sphere surface temperature in a free-molecule flow.

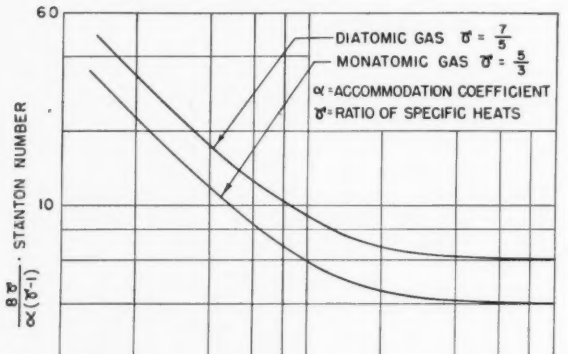

FIG. 3. Convective heat transfer from spheres in a free-molecule flow.

$$\varphi = 1 + \frac{1 + {}^3/_2\sqrt{\pi}\, x[1 + erf(x)]e^{x^2}}{1 + \sqrt{\pi}\, x[1 + erf(x)]e^{x^2}}$$

$$x = (U/V_m)\cos\theta$$

and from Fig. 1, $dA = 2\pi r^2 \sin\theta\, d\theta$.

Substituting the above into Eq. (1) the heat flux (in dimensionless form) into a monatomic gas becomes

$$\frac{4\sqrt{\pi}}{\alpha N k T_i V_m}\left(\frac{dq}{dA}\right) = \left(4\frac{T_p}{T_i} - \gamma M_0^2 - 4\right)e^{-x^2} + \left(4\frac{T_p}{T_i} - \gamma M_0^2 - 5\right)\sqrt{\pi}x[1 + erf(x)] \quad (3)$$

The average convective heat transfer rate per unit area, assuming T_p to be constant, is found by integrating Eq. (3) over the sphere. The result is

$$8Q/\alpha N k T_i U = g(z)\,(T_p/T_i) - f(z) \quad (4)$$

where

$$g(z) = 4\left[1 + \frac{1}{z}\,ierfc\,(z) + \frac{1}{2z^2}\,erf(z)\right]$$

$$f(z) = (2z^2 + 5)\left[1 + \frac{1}{z}\,ierfc(z)\right] + (2z^2 + 3)\,\frac{erf(z)}{2z^2}$$

$$z^2 = (\gamma/2)\,M_0^2$$

In the same manner the average heat-transfer rate per unit area into a diatomic gas is found using Eq. (2). This result is

$$8Q/\alpha N k T_i U = p(z)\,(T_p/T_i) - q(z) \quad (5)$$

where

$$p(z) = 6\left[1 + \frac{1}{z}\,ierfc(z) + \frac{1}{2z^2}\,erf(z)\right]$$

$$q(z) = (2z^2 + 7)\left[1 + \frac{1}{z}\,ierfc(z)\right] + (2z^2 + 5)\,\frac{erf(z)}{2z^2}$$

The equilibrium temperature for the sphere neglecting radiation, T_{aw}, may be found by setting the heat transfer equal to zero. For the monatomic gas,

$$T_{aw}/T_i = f(z)/g(z) \quad (6)$$

For the diatomic gas,

$$T_{aw}/T_i = q(z)/p(z) \quad (7)$$

The average convective heat-transfer coefficient for high-speed flow is defined as

$$h = Q/(T_p - T_{aw}) \quad (8)$$

Substituting Eqs. (6) and (8) into Eq. (4) and writing a dimensionless heat-transfer coefficient in terms of the Stanton Number gives, for the monatomic gas,

$$St = \frac{Nu}{Re \cdot Pr} = \frac{\alpha(\gamma - 1)}{8\gamma}\,q(z) \quad (9)$$

Similarly, substitution of the corresponding equations for the diatomic gas yields

$$St = [\alpha(\gamma - 1)/8\gamma]p(z) \quad (10)$$

The results of the foregoing analysis are plotted in Figs. 2 and 3. The ratio of the gas stream to stagnation temperature was calculated from the well-known equation

$$T_s/T_i = 1 + [(\gamma - 1)/2]M_0^2$$

REFERENCE

[1] Stalder, R., and Jukoff, D., *Heat Transfer to Bodies Traveling at High Speed in the Upper Atmosphere*, Journal of the Aeronautical Sciences, Vol. 15, No. 7, pp. 381–391, July, 1948.

Heat Transfer by Laminar Flow from a Rotating Plate

Knox Millsaps and Karl Pohlhausen
Office of Air Research, U.S.A.F.
February 9, 1951

THE EQUATION OF CONTINUITY, the Navier-Stokes equations, and the energy equation for the steady motion of an incompressible fluid when expressed in cylindrical coordinates (r, ϑ, z) and with velocity components (u_r, u_ϑ, u_z) are, respectively,

$$\frac{\partial u_r}{\partial r} + \frac{u_r}{r} + \frac{1}{r}\frac{\partial u_\vartheta}{\partial \vartheta} + \frac{\partial u_z}{\partial z} = 0$$

$$u_r\frac{\partial u_r}{\partial r} + \frac{u_\vartheta}{r}\frac{\partial u_r}{\partial \vartheta} - \frac{u_\vartheta^2}{r} + u_z\frac{\partial u_r}{\partial z} = -\frac{1}{\rho}\frac{\partial p}{\partial r} + \nu\left(\frac{\partial^2 u_r}{\partial r^2} + \frac{1}{r}\frac{\partial u_r}{\partial r} - \frac{u_r}{r^2} + \frac{1}{r^2}\frac{\partial^2 u_r}{\partial \vartheta^2} - \frac{2}{r^2}\frac{\partial u_\vartheta}{\partial \vartheta} + \frac{\partial^2 u_r}{\partial z^2}\right)$$

$$u_r\frac{\partial u_\vartheta}{\partial r} + \frac{u_\vartheta}{r}\frac{\partial u_\vartheta}{\partial \vartheta} + \frac{u_r u_\vartheta}{r} + u_z\frac{\partial u_\vartheta}{\partial z} = -\frac{1}{\rho}\frac{\partial p}{r\partial \vartheta} + \nu\left(\frac{\partial^2 u_\vartheta}{\partial r^2} + \frac{1}{r}\frac{\partial u_\vartheta}{\partial r} - \frac{u_\vartheta}{r^2} + \frac{1}{r^2}\frac{\partial^2 u_\vartheta}{\partial \vartheta^2} + \frac{2}{r^2}\frac{\partial u_r}{\partial \vartheta} + \frac{\partial^2 u_\vartheta}{\partial z^2}\right)$$

$$u_r\frac{\partial u_z}{\partial r} + \frac{u_\vartheta}{r}\frac{\partial u_z}{\partial \vartheta} + u_z\frac{\partial u_z}{\partial z} = -\frac{1}{\rho}\frac{\partial p}{\partial z} + \nu\left(\frac{\partial^2 u_z}{\partial r^2} + \frac{1}{r}\frac{\partial u_z}{\partial r} + \frac{1}{r^2}\frac{\partial^2 u_z}{\partial \vartheta^2} + \frac{\partial^2 u_z}{\partial z^2}\right)$$

$$c_v\left[u_r\frac{\partial T}{\partial r}+\frac{u_\vartheta}{r}\left(\frac{\partial T}{\partial \vartheta}\right)+u_z\left(\frac{\partial T}{\partial z}\right)\right]=\frac{k}{\rho}\left(\frac{\partial^2 T}{\partial r^2}+\frac{1}{r}\frac{\partial T}{\partial r}+\frac{1}{r^2}\frac{\partial^2 T}{\partial \vartheta^2}+\frac{\partial^2 T}{\partial z^2}\right)+\frac{\nu}{2}\left(e_{rr}^2+e_{\vartheta\vartheta}^2+e_{zz}^2+2e_{r\vartheta}^2+2e_{rz}^2+2e_{z\vartheta}^2\right)$$

The case of a rotating infinite plate (constant angular velocity ω) heated at a constant temperature (t_0) is characterized by the boundary conditions

$$u_r(r,\vartheta,0)=0,\qquad u_z(r,\vartheta,0)=0$$
$$u_r(r,\vartheta,\infty)=0,\qquad u_\vartheta(r,\vartheta,\infty)=0$$
$$u_\vartheta(r,\vartheta,0)=\omega r$$

The partial differential system may be separated and reduced[3] for laminar flow to ordinary nonlinear differential equations by assuming

$$u_r=rf(z),\qquad u_\vartheta=rg(z)$$
$$u_z=h(z),\qquad p=p(z)$$
$$T=r^2S(z)+q(z)+t_0$$

The reduced equations are, respectively,

$$2f+h'=0$$
$$f^2-g^2+hf'=\nu f''$$
$$2fg+hg'=\nu g''$$
$$hh'=-(1/\rho)\,p'+\nu h''$$
$$2c_v fS+c_v hS'=(k/\rho)S''+\nu(f'^2+g'^2)$$
$$c_v hq'=(k/\rho)\,(4S+q'')+\nu(4f^2+2h'^2)$$

where primes denote differentiation with respect to z.

This system can be integrated numerically[4] or analogically. A dimensionless representation, together with a physical discussion, will be given in a later paper.

References

[1] These forms of the continuity and dynamical equations are given by L. Hopf, *Handbuch der Physik*, Bd VII, Mechanik der flüssigen und gasförmigen Körper, p. 95.

[2] The energy equation may be inferred from S. Goldstein, *Modern Developments in Fluid Dynamics*, pp. 104 and 606.

[3] The separating transformations for the velocities are due to Theodore von Kármán, *Zeits. für angw. Math u. Mech*, Vol. 1, p. 245, 1921.

[4] Numerical results for f, g, and h have been given by W. G. Cochran, *Proc. Camb. Phil. Soc.*, Vol. 30, p. 365, 1934.

Proper Use of the M.I.T. Tables for Supersonic Flow Past Inclined Cones

Milton D. Van Dyke,* George B. W. Young, and Charles Siska
The RAND Corporation, Santa Monica, Calif.

February 1, 1951

In applying the M.I.T. tables[1] to inclined cones, confusion can arise because the results are tabulated in wind axes rather than body axes. In the notation of the tables (which is used here throughout), the velocity components, pressure, and density at any point are, to first order in ϵ,

$$u=\bar{u}+x\epsilon\cos\phi \tag{1a}$$
$$v=\bar{v}+y\epsilon\cos\phi \tag{1b}$$
$$w=z\epsilon\sin\phi \tag{1c}$$
$$p=\bar{p}+\eta\epsilon\cos\phi \tag{1d}$$
$$\rho=\bar{\rho}+\xi\epsilon\cos\phi \tag{1e}$$

The coefficients ($\bar{u}$, $\bar{v}$, $\bar{p}$, $\bar{\rho}$, x, y, z, η, ξ) are tabulated as functions of θ. Evaluating these expressions at $\theta=\theta_s$ does not, in general, yield values of the flow quantities on the surface of the cone; it yields values at the position occupied by the cone before it was yawed (shown dotted in Fig. 1), which are of no interest.

* Now at Ames Aeronautical Laboratory, Moffett Field, Calif.

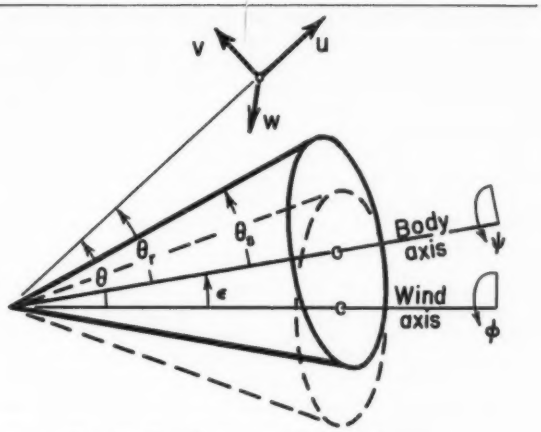

Fig. 1. Coordinate axes for inclined cone.

Values on the surface can be found only after the results have been transformed from wind to body axes. To first order in ϵ, the flow quantities in body axes (subscript r) are found to be

$$u_r=\bar{u}+(x+\bar{v})\,\epsilon\cos\psi \tag{2a}$$
$$v_r=\bar{v}+\left[y-\frac{\bar{a}^2(\bar{u}+\bar{v}\cot\theta)}{\bar{a}^2-\bar{v}^2}-\bar{u}\right]\epsilon\cos\psi \tag{2b}$$
$$w_r=(z-\bar{v}\csc\theta)\,\epsilon\sin\psi \tag{2c}$$
$$p_r=\bar{p}+\left[\eta+\bar{\rho}\bar{v}\frac{\bar{a}^2(\bar{u}+\bar{v}\cot\theta)}{\bar{a}^2-\bar{v}^2}\right]\epsilon\cos\psi \tag{2d}$$
$$\rho_r=\bar{\rho}+\left(\xi+\bar{\rho}\bar{v}\frac{\bar{u}+\bar{v}\cot\theta}{\bar{a}^2-\bar{v}^2}\right)\epsilon\cos\psi \tag{2e}$$

Here, the quantities ($\bar{a}$, $\bar{u}$, $\bar{v}$, etc.) are to be evaluated from the tables using, for θ, the angle θ_r measured from the body axis (Fig. 1).

On the surface of the cone, $\bar{v}=0$, and (except for the trivial case of v) Eqs. (2) reduce to Eqs. (1) with ϕ replaced by ψ. Therefore, the conversion is unnecessary if values are required only on the surface and only to first order in ϵ, but this fact is not evident until the conversion has been carried out.

When terms in ϵ^2 are retained, the conversion must be made even for surface values and is rather complicated. For example, the one quantity of greatest interest to aerodynamicists—the pressure on the surface—is found in terms of tabulated results as

$$p_r/\bar{p}=1+(\eta/\bar{p})\epsilon\cos\psi+[(p_0/\bar{p})+(\gamma\bar{u}^2/2\bar{a}^2)+{}^1/_2\cot\theta_s(\eta/\bar{p})]\epsilon^2+[(p_2/\bar{p})+(\gamma\bar{u}^2/2\bar{a}^2)-{}^1/_2\cot\theta_s(\eta/\bar{p})]\epsilon^2\cos 2\psi \tag{3}$$

where all quantities are evaluated from the tables at $\theta=\theta_s$. Away from the surface, of course, the expression is even more complicated.

As the cone rotates through an angle ϵ, the shock wave remains a circular cone to first order, and rotates through an angle δ. First-order values of flow quantities just behind the shock wave can be found from a slight modification of Eqs. (2). In the coefficients of ϵ, each term but the first should be multiplied by $\alpha=\delta/\epsilon$; for example, at the shock wave,

$$u_r=\bar{u}+(x+\alpha\bar{v})\epsilon\cos\psi \tag{4}$$

with ($\bar{u}$, $\bar{v}$, x) evaluated at $\theta=\theta_w$. The corresponding modification of terms in ϵ^2 would involve also the factors β_0 and β_2 of *Report No. 5*.

It appears that the usefulness of the M.I.T. tables could be greatly increased by retabulating them in body coordinates. That is, the expression $(x+\bar{v})$ appearing in Eq. (2a) would be tabulated instead of x, etc. The special values required for de-

termining the flow just behind the shock wave could be included separately.

The values of flow quantities calculated just behind the shock wave join smoothly to the remainder of the flow field only if ϵ is infinitesimal. Discrepancies arise if the results are applied as an approximation for finite values of ϵ (as is done in starting a characteristic solution for an inclined ogival body). Preliminary study indicates that this defect can be eliminated by using relations such as Eq. (4) everywhere, with α, β_0, and β_2 varying through the flow field. For example, to first order in ϵ, let

$$\alpha = 1 - [1 - (\delta/\epsilon)]\,(\theta - \theta_s)/(\theta_w - \theta_s)$$

It should also be observed that the notation for drag coefficient is not uniform throughout the three volumes of tables. The symbol K_D has one meaning in *Report No. 1*, another meaning in *Report No. 3* and most of *Report No. 5*, and a third meaning in Eq. (41) of *Report No. 5*. In terms of tabulated quantities, the conventional aerodynamic drag coefficient (referred to base area) is given to order ϵ^2 by

$$C_D = AK_D + \{K_{DYH}[AK_D + (2/\gamma M^2)] + (1/\gamma M^2)\}\epsilon^2 \quad (5)$$

where $A = 2$ if K_D is taken from *Report No. 1* and where $A = 8/\pi$ if K_D is taken from *Report No. 3*.

REFERENCE

[1] Staff of the Computing Section, Center of Analysis (under the direction of Zdenek Kopal), *Tables of Supersonic Flow Around Cones*, Technical Report No. 1, 1947; *Tables of Supersonic Flow Around Yawing Cones*, Technical Report No. 3, 1947; *Tables of Supersonic Flow Around Cones of Large Yaw*, Technical Report No. 5, 1949 (Massachusetts Institute of Technology, Cambridge, Mass.).

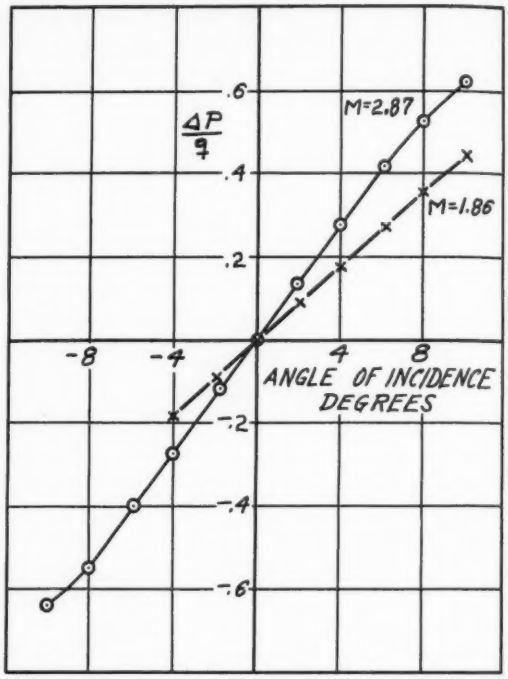

FIG. 2 PROBE CALIBRATION

A Probe for Measuring Flow Inclination in a Supersonic Air Stream

Robert D. Fusfeld

Aerophysics Laboratory, North American Aviation, Inc., Inglewood, Calif.

February 5, 1951

THE USUAL DEVICE for measuring flow inclination in a supersonic air stream makes use of a thin two-dimensional wedge or some modification of a wedge. Orifices placed on opposite sides of the wedge experience a pressure differential that serves as an indication of the inclination of the air stream. However, as the Mach Number becomes large, the pressure coefficient differential due to the inclination angle becomes small. Other difficulties are that wedge-type devices are not especially easy to construct, they have a relatively large size, there is a tendency to deflect under air loads, etc.

Other instruments sometimes used to measure flow inclination are free floating vanes, hot-wire probes, and blunt bodies with pressure orifices near the leading edge. The last devices, similar to typical subsonic yaw heads, show most promise. The probe described here is a form of blunt body specially designed for use in supersonic flows.

The probe is shown in Fig. 1. It consists of four small-diameter tubes soldered together with the leading edges cut off at some large angle with the axis. A conical nose shape is the simplest to make and is one that gives satisfactory results. A probe of this design can easily be fabricated in large numbers for use in rakes, etc. By making the instrument as small as possible, the disturbance introduced into the air stream can be minimized. It is, therefore, suitable for use in close proximity to small models in wind-tunnel testing. Although designed specifically for use at supersonic speeds, the probe can also be used at subsonic and transonic speeds.

Sample calibration curves for inclination angles in the plane of one pair of tubes are shown in Fig. 2. The pressure differentials at $M = 2.87$ are about two and one-half times as great as would be obtained on a thin wedge. At $M = 1.86$, the pressures are approximately the same as for a wedge.

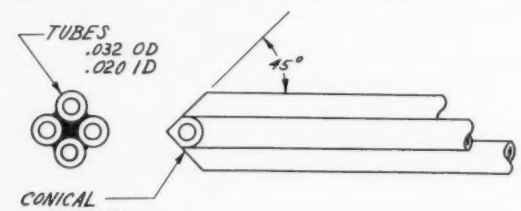

FIG. 1 FLOW INCLINATION PROBE

Formulas for Bending with Axial Tension

Alfred S. Niles

Professor of Aeronautical Engineering, Aeronautics Laboratory, Stanford University, Stanford, Calif.

February 21, 1951

THE GENERAL DIFFERENTIAL EQUATION for a beam-column with axial compression is

$$(d^2M/dx^2) + (PM/EI) = \phi(w) \quad (1)$$

where M is the bending moment, P is the axial load, E is the modulus of elasticity, I is the moment of inertia of the section, and $\phi(w)$ is a function of the transverse loading that is independent of P. P is considered positive, and EI/P may be replaced by j^2, also a positive quantity. The general solution of Eq. (1) is then

$$M = C_1 \sin (x/j) + C_2 \cos (x/j) + f(w) \quad (2)$$

When the axial load is tensile, in order to be able to continue to consider EI/P a positive quantity, Eq. (1) is usually replaced by

$$(d^2M/dx^2) - (PM/EI) = \phi(w) \quad (3)$$

which has the general solution

$$M = T_1 \sinh (x/j) + T_2 \cosh (x/j) + g(w) \quad (4)$$

Formulas for C_1, C_2, and $f(w)$ for various types of transverse load are presented in Table 14:3 of *Airplane Structures*, Vol. II, by Niles and Newell,[1] and parallel formulas for what are here termed T_1, T_2, and $g(w)$ are to be found in Table 14:5 of the same volume. Comparison of the tables shows that wherever W, w, or j appear in a formula for axial compression, they appear in the same place in the conjugate formula for axial tension. Also, whenever a trigonometric function appears in a compression formula, the corresponding hyperbolic function appears in the same place in the conjugate formula for axial tension. Sometimes the signs in the conjugate formulas are the same. However, sometimes they are reversed, and there is no obvious rule by which the signs in a formula for axial tension can be determined from those in the conjugate formula for axial compression. The purpose of this note is to demonstrate a rule by which this can be accomplished.

Eq. (1) would apply to the beam-column with axial tension if P were assumed to have a negative value. Then, if j^2 were taken as EI divided by the absolute value of P, it would be a positive quantity with a real square root, but Eq. (1) would become

$$d^2M/dx^2 + [M/(ij)^2] = \phi(w) \quad (5)$$

and its general solution would be

$$M = K_1 \sin (x/ij) + K_2 \cos (x/ij) + g(w) \quad (6)$$

where K_1, K_2, and $g(w)$ for any given type of transverse load would have the same forms as C_1, C_2, and $f(w)$, except that j would be consistently replaced by ij.

But, from the theory of complex numbers,

$$\sin (x/ij) = -i \sinh (x/j) \qquad \cos (x/ij) = \cosh (x/j)$$
$$\tan (x/ij) = -i \tanh (x/j) \quad (7)$$

Substituting Eq. (7) into Eq. (6), the latter takes the from

$$M = T_1 \sinh (x/j) + T_2 \cosh (x/j) + g(w) \quad (4)$$

where $T_1 = -iK_1$ and $T_2 = K_2$.

Thus we arrive at the following rules for developing the formulas for a given transverse load and axial tension from the conjugate formula for axial compression:

(a) Substitute ij for j wherever the latter appears as a dimension, as in Wj or wj^2.

(b) For each trigonometric function, substitute the corresponding hyperbolic function, multiplying the resulting hyperbolic sines and tangents by $-i$ and the hyperbolic cosines and secants by $+1$.

For example, the formula for the bending moment on a pin-ended beam-column of length, L, due to an axial compression, P, and a transverse concentrated load, W, acting at a distance, a, from the left end, is, for $x > a$ (see Case 4, Table 14:3, *Airplane Structures*, Vol. II, pages 92–93),

$$M = \frac{Wj \sin (a/j) \sin (x/j)}{\tan (L/j)} - Wj \sin (a/j) \cos (x/j) \quad (8)$$

Making the specified substitutions, the conjugate formula for axial tension will be

$$M = \frac{Wij(-i) \sinh (a/j)(-i) \sinh (x/j)}{-i \tanh (L/j)} - Wij(-i) \sinh (a/j) \cosh (x/j)$$
$$= \frac{Wj \sinh (a/j) \sinh (x/j)}{\tanh (L/j)} - Wj \sinh (a/j) \cosh (x/j) \quad (9)$$

Eq. (9) agrees with Case 4 of Table 14:5.[1]

For a transverse load varying uniformly from zero at $x = 0$ to w at $x = L$, the formula for bending moment due to axial compression is (Case 5, Table 14:3[1])

$$M = -[wj^2 \sin (x/j)/\sin (L/j)] + (wj^2x/L) \quad (10)$$

Making the specified substitutions, the formula for axial tension is

$$M = -\frac{w(ij)^2(-i) \sinh (x/j)}{-i \sinh (L/j)} + \frac{w(ij)^2x}{L}$$
$$= [wj^2 \sinh (x/j)/\sinh (L/j)] - (wj^2x/L) \quad (11)$$

For a uniformly distributed load w and end moments M_1 and M_2, the formula for axial compression is (Case 3, Table 14:3[1])

$$M = \frac{M_2 - wj^2 - (M_1 - wj^2) \cos (L/j)}{\sin (L/j)} \sin (x/j) + (M_1 - wj^2) \cos (x/j) + wj^2 \quad (12)$$

Making the specified substitutions, the formula for axial tension is

$$M = \frac{M_2 - w(ij)^2 - (M_1 - wi^2j^2) \cosh (L/j)}{-i \sinh (L/j)} \times (-i) \sinh (x/j) + (M_1 - wi^2j^2) \cosh (x/j) + wi^2j^2$$
$$= \frac{M_2 + wj^2 - (M_1 + wj^2) \cosh (L/j)}{\sinh (L/j)} \sinh (x/j) + (M_1 + wj^2) \cosh (x/j) - wj^2 \quad (13)$$

It may be noted that in the first example the signs of the terms in the two formulas were the same; in the second, they were reversed; and in the third, some were reversed while others remained unchanged.

All of the expressions of Table 14:5,[1] including the terms for the Three Moment Equation, can be obtained in this manner from those of Table 14:3. In obtaining the expressions for C_1 (called T_1 in this note), the results must be multiplied by $-i$ to take account of the substitution of $-i \sinh (x/j)$ for the $\sin (x/j)$ by which the C_1 of Table 14:3[1] would be multiplied in a formula for bending moment.

The formulas for the total shear on a beam-column can be treated in the same manner as those for bending moment. The formulas for slope and deflection under axial tension can be developed by using a negative value for P in those for axial compression, and vice versa.

In making this study, a typographical error was found in Case 10 of Table 14:5[1] (axial tension and a clockwise couple applied in the span). The constant C_1 for $x < a$ should be preceded by a minus sign.

Reference

[1] Niles, A. S., and Newell, J. S., *Airplane Structures*, 3rd Ed., Vol. 2 John Wiley & Sons, Inc., New York, 1943.

Simplified Compressible Laminar Boundary-Layer Theory*

Arthur N. Tifford
Department of Aeronautical Engineering, The Ohio State University, Columbus
January 29, 1951

DURING RECENT YEARS several excellent mathematical analyses of the compressible laminar boundary layer have been published. Unfortunately, however, the essential unity of the analytical results at Mach Numbers as high as 5 (under some circumstances) has apparently not been noted by others. It is the purpose of this communication to emphasize that unity.

The writer was first concerned with the effect of variable fluid properties upon the surface characteristics of the boundary layer when doing the research reported in reference 1. Busemann[2] and Eckert and Drewitz[3] had already shown that, in the case of a compressible gas flowing along a flat plate, the effect is very small when the Mach Number of the flow is not too large—e.g., 3 per cent at Mach Number = 2. The writer concluded on the basis of qualitative reasoning that it must also be small in the general case of a surface of arbitrary shape (except in the neighborhood of a shock wave) if the "local" Mach Number of the external flow is somewhat lower.

More recently, Howarth[4] has studied the effect of compressibility upon the boundary layer at Mach Numbers near unity when the local free-stream velocity increases or decreases linearly with the distance along the surface. Let us reconsider his results.

In the case of the linearly increasing local free-stream velocity, $U = \beta x$, he found the local skin friction coefficient, $\tau/\rho_0\nu_0^{1/2}\beta^{3/2}x$ or $\tau/\rho_0 U^2\,(\nu_0/Ux)^{1/2}$, to decrease from 1.23 to 0.87 as the local Mach Number increases from 0 to $\beta x/a_0 = 1$—i.e., local Mach Number based on free-stream static temperature increases from 0 to 1.12. The quantity, $\nu_0^{1/2}\beta^{-3/2}x^{-1}(\partial u/\partial Y)_0$, on the other hand, increases only 5 per cent, from 1.23 to 1.29, over the same range of Mach Numbers. However, the latter quantity is "identically" the local skin friction coefficient based upon the local fluid properties at the wall, $\tau/\rho_w U^2(\nu_w/Ux)^{1/2}$. The expectation of the writer, that regardless of pressure gradient only very small surface compressibility effects (properly defined) exist in this Mach Number range, is thus supported.†

Let us turn now to the case of the linearly decreasing local free-stream velocity,‡ $U = U_0 - U_1x$. Howarth has found that, at the point at which $8(U_1x/U_0) = 0.1$, the friction coefficient, $4\tau x^{1/2}/\rho_0\nu_0^{1/2}\,U_0^{3/2}$ or $4\tau/\rho_0 U_0^2\,(\nu_0/U_0x)^{1/2}$, is 1.228 when $M_0 = 1$ as compared with 1.226 in the incompressible flow case—excellent agreement. When we define the local friction coefficient in terms of the local free-stream velocity and the local fluid properties at the wall—as before—excellent agreement (i.e., better than 1 per cent) with the incompressible flow case is still obtained.

It does not seem out of place to remark here that in a Readers' Forum note,[5] Chapman and Rubesin's results for the nonisothermal flat plate[6] have been shown to be essentially the same as those obtainable on the basis of fluid properties being "effectively" constant at the local wall value. The argument is probably more easily followed when the local surface shearing stress and the local rate of heat transfer are examined, rather than their average

* Work supported by the Office of Air Research, U.S.A.F.

† It is interesting to replot the boundary-layer velocity profiles of Fig. 5, reference 4, as in Fig. A. The merging of the profiles associated with different local Mach Numbers is due solely to the use of the local fluid kinematic viscosity at the wall, instead of its stagnation value, in the nondimensional boundary-layer thickness coordinate.

‡ The subscript zero refers in this case to conditions in the free stream at the leading edge rather than to conditions at a stagnation point.

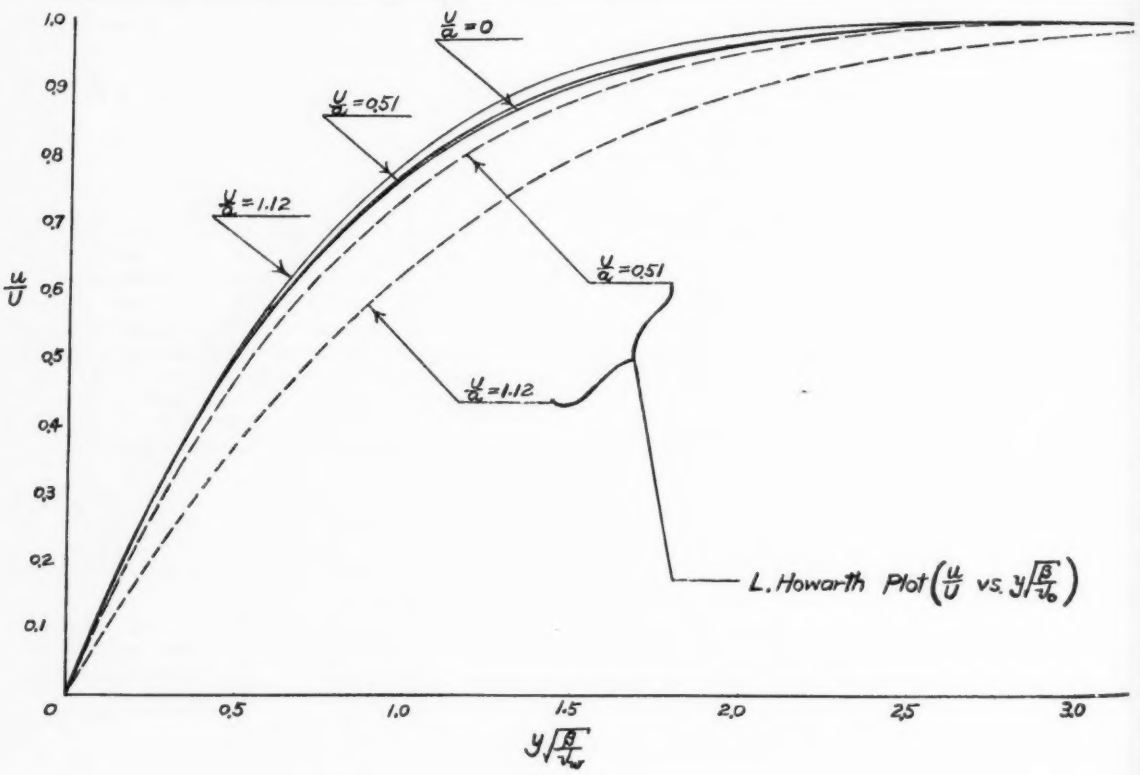

FIG. A.

value over the plate. For example, the local surface shearing stress has been found in reference 6 to be given by Eq. (57a).

$$\tau_w = [f''(0)/4] U_\infty C_w \sqrt{\rho_\infty U_\infty \mu_\infty / Cx} \qquad (57a)$$

At low free-stream temperatures, C_w and C are identical. Eq. (57a) thus reduces to the solution obtained on the basis of the fluid properties being constant at the local wall value.

$$\tau_w = [f''(0)/4] \sqrt{\rho_w U_\infty \mu_w / x}$$

At high free-stream temperatures, however, the definitions of C_w and C allow them to be different in general, the former being appropriate to the local surface fluid physical properties; the latter, to the average surface fluid physical properties. Consider, though, the strong asymptotic nature of the boundary layer upon which essentially all boundary-layer analysis leans. Increasingly crude assumptions may be made at points lying successively further ahead of the point at which the boundary-layer characteristics are sought—e.g., the conditions at the leading edge of a flat plate are completely ignored. Conversely, increasingly precise assumptions must be made at points lying successively closer to the point of interest. It is to be expected therefore that the best value for C is essentially the local C_w, rather than an average C_w. On this basis the results of the two analyses become identical "under all conditions."

It is not the intent of this note to de-emphasize the importance of compressible laminar boundary-layer analyses in which fluid properties are allowed to vary. They are needed for a fuller understanding of the details of the flow, for the evaluation of surface phenomena at very high Mach Numbers and at certain combinations of high local Mach Numbers and surface pressure gradient, etc. It is rather the intent to emphasize that, in many current applications, the characteristics of the laminar boundary layer at any point on a surface may be determined within engineering precision on the basis of the simpler analyses extant in the literature, assuming fluid properties throughout the boundary layer to be the same as at that particular point.

References

[1] Tifford, A. N., *The Thermodynamics of the Laminar Boundary Layer of a Heated Body in a High-Speed Gas Flow Field*, Journal of the Aeronautical Sciences, Vol. 12, No. 2, pp. 241–251, April, 1945.

[2] Busemann, A., *Gas-stromung mit laminaren Grenzschicht entlang einer Platte, ZAMM*, Vol. 15, No. 23, pp. 22–25, 1935.

[3] Eckert, E., and Drewitz, O., *The Heat Transfer to a Plate in Flow at High Speed*, Forschung a.d. Gebiete d. Ingenieurwesens, Vol. II, No. 3, pp. 116–122, May-June, 1940; also N.A.C.A. T.M. No. 1045, May, 1943.

[4] Howarth, L., *Concerning the Effect of Compressibility on Laminar Boundary Layers and Their Separation*, Proc. of the Royal Society of London, Series A, Vol. 194, No. 1036, pp. 16–42, July, 1948.

[5] Tifford, A. N., *On the Surface Effects of a Compressible Laminar Boundary Layer*, Readers' Forum, Journal of the Aeronautical Sciences, Vol. 17, No. 3, pp. 187–188, March, 1950.

[6] Chapman, D. R., and Rubesin, M. W., *Temperature and Velocity Profiles in the Compressible Laminar Boundary Layer with Arbitrary Distribution of Surface Temperature*, Journal of the Aeronautical Sciences, Vol. 16, No. 9, pp. 547–565, September, 1949.

Changes of Address

Since the Post Office Department does not as a rule forward magazines to forwarding addresses, it is important that the Institute be notified of changes in address 30 days in advance of publishing date to ensure receipt of every issue of the JOURNAL and REVIEW.

Notices should be sent directly to:

Institute of the Aeronautical Sciences, Inc.

2 East 64th Street, New York 21, New York

INSTITUTE *of the* AERONAUTICAL SCIENCES

1932–1951

Since its incorporation in October, 1932, as a scientific membership society to advance the art and science of aeronautics, the Institute of the Aeronautical Sciences, in over eighteen years of service to aviation, has become the representative technical society for the aviation industry and profession. It is the only organization in the United States which brings together all of the sciences and branches of engineering and technology which are applied to aeronautics.

Publications

Papers presented at meetings or submitted to the Editorial Board are published in the JOURNAL OF THE AERONAUTICAL SCIENCES or the AERONAUTICAL ENGINEERING REVIEW. The JOURNAL prints in each issue several full-length scientific papers on new research and developments in various fields applied to aviation. The REVIEW keeps members and subscribers up to date on aeronautical news and literature through reviews of new books and periodical articles, government publications and trade literature and publishes papers on applied engineering and aircraft production.

The AERONAUTICAL ENGINEERING CATALOG, published yearly, is a guide to sources and specifications of materials, parts, and accessories used in the design and production of aircraft, aircraft engines, and parts.

Research Facilities

Through the Aeronautical Archives of the Institute, members have for their use the most complete aeronautical library and reference research facilities maintained by any technical society. At the New York building of the Institute, The W. A. M. Burden Library of books, reports and periodicals, the Aeronautical Index of subject files, biographic files and bibliography, and the historical and art collections in the Archives are available for study. The Pacific Aeronautical Library at 7660 Beverly Boulevard, Los Angeles, maintains a reference collection and reading room for members and loans books to company libraries in the area. Through The Paul Kollsman Lending Library, aeronautical books are lent by mail without charge to members anywhere in the continental United States. In addition to a complete collection of standard aeronautical reference works, the Kollsman Lending Library has available for loan new aviation books as they are reviewed in the AERONAUTICAL ENGINEERING REVIEW.

Membership

In addition to membership in professional societies representing their particular fields, specialists applying their knowledge and experience to aeronautics find membership in the Institute of great value in the contacts made with others engaged in aeronautical work and in the broad coverage of all aeronautical problems furnished through its meetings and publications. All applications for membership are carefully reviewed by the Membership Committee, which recommends the grade of membership for which the applicant is found eligible. There are advanced grades of membership—Fellow and Honorary Fellow—to which members may be elected as their experience warrants. Thus, a member receives due recognition—more valuable because it is given by his colleagues—for his contributions to the progress of aeronautics. New applicants may be elected by the Membership Committee to the grade of Associate Fellow if they have been engaged for not less than ten years in the practice of the aeronautical sciences and shall have been in responsible charge of important scientific or engineering work, or shall have otherwise made outstanding contributions to the aeronautical sciences; to the grade of MEMBER if they have been engaged in professional work for at least eight years and have acquired a recognized standing in engineering, design, or other special work applied to aeronautics; to the grade of Associate Member if they have acquired a recognized standing in an administrative capacity in the aviation industry; to the grade of Technical Member if they are recent engineering school graduates or are engaged in technical aeronautical work. Student Members are admitted by application through Student Branches organized at their schools. Aeronautical companies, as well as individuals, are affiliated with, and participate in, the support of the Institute through Corporate Membership.

Dues

An entrance fee of $10 is required of all new members who apply for admission to a grade of membership to be specified by the Membership Committee (Corporate Members, Foreign Members, and Student Members being excepted).

Annual membership dues include a subscription to the AERONAUTICAL ENGINEERING REVIEW. Dues for the various grades of membership are as follows: Fellows—$16.50; Associate Fellows—$16.50; MEMBERS—$13.50; Associate Members—$13.50; Technical Members—(26 years of age and over) $13.50, (under 26) $6.50.

The regular subscription price for the JOURNAL OF THE AERONAUTICAL SCIENCES and the AERONAUTICAL ENGINEERING REVIEW is $12 and $3.00 per year, respectively. Members may subscribe to the JOURNAL at $4.00 per year.

Those who are engaged in aeronautical work or who have an interest in any technical phase of aviation will find the services of the Institute to be a necessary aid in keeping abreast of developments in these times of such rapid progress. An application form and further information about membership can be obtained from an Institute member or by writing to the Secretary.

INSTITUTE OF THE AERONAUTICAL SCIENCES, INC.

2 EAST 64TH STREET

NEW YORK 21, N.Y.